Machine Learning and Data Fusion of Simulated Remote Sensing Data

Erik T. Higgins

Dissertation submitted to the Faculty of the
Virginia Polytechnic Institute and State University
in partial fulfillment of the requirements for the degree of

Doctor of Philosophy
in
Aerospace Engineering

Eric G. Paterson, Co-chair
Laura Freeman, Co-chair
Jonathan S. Pitt
Heng Xiao
Scott England

April 17, 2023
Blacksburg, Virginia

Keywords: ship wake, naval hydrodynamics, remote sensing, neural networks, data fusion

Machine Learning and Data Fusion of Simulated Remote Sensing Data

Erik T. Higgins

(ABSTRACT)

Modeling and simulation tools are described and implemented in a single workflow to develop a means of simulating a ship wake followed by simulated synthetic aperture radar (SAR) and infra-red (IR) images of these ship wakes. A parametric study across several different ocean environments and simulated remote sensing platforms is conducted to generate a preliminary data set that is used for training and testing neural network–based ship wake detection models. Several different model architectures are trained and tested, which are able to provide a high degree of accuracy in classifying whether input SAR images contain a persistent ship wake. Several data fusion models are explored to understand how fusing data from different SAR bands may improve ship wake detection, with some combinations of neural networks and data fusion models achieving perfect or near-perfect performance. Finally, an outline for a future study into multi-physics data fusion across multiple sensor modalities is created and discussed.

Machine Learning and Data Fusion of Simulated Remote Sensing Data

Erik T. Higgins

(GENERAL AUDIENCE ABSTRACT)

This dissertation focuses on using computer simulations to first simulate the wakes of ships on the ocean surface, and then simulate airborne or satellite-based synthetic aperture radar (SAR) and infra-red (IR) images of these ship wakes. These images are used to train machine learning models that can be given a SAR or IR image of the ocean and determine whether or not the image contains a ship wake. The testing shows good preliminary results and some models are able to detect ship wakes in simulated SAR images with a high degree of accuracy. Data fusion models are then created which seeks to fuse data sources together in order to improve ship wake detection. These data fusion models are tested using the simulated SAR images, and some of these data fusion models show a positive impact on ship wake detection. Next steps for future research are documented, such as data fusion of SAR and IR data in order to study how fusion of these sensors impacts ship wake detection compared to just a single SAR sensor or multiple SAR sensors fused together.

Acknowledgments

I would like to thank my family for their support in the years leading up to this dissertation and their encouragement in tough times. I would like to acknowledge my committee members and advisors Dr. Eric Paterson, Dr. Laura Freeman, Dr. Jonathan Pitt, Dr. Heng Xiao, and Dr. Scott England for their help in my graduate studies at Virginia Tech and insightful discussions regarding the work done in this dissertation. My coworkers and fellow lab members have also been a great source of help and casual conversation: Dr. John Gilbert, Dr. Justin Kauffman, Dr. Dylan Wall, Dr. Ryan Somero, Dr. Andre Basovich, Dr. John Pierce, Christian Martin, Dr. Matt Jones, and Colby Jamerson. I would also like to thank my friends whom I made at Virginia Tech for the fun times we had while we were together in Blacksburg and further beyond in spite of everyone moving across the country and world.

Contents

List of Figures

List of Tables

Chapter 1

Introduction

1.1 Motivation

Remote sensing of the ocean in order to detect ship wakes is a well-studied problem (Munk et al., 1987, 2000). Many developments in remote sensing, such as the invention of infrared imagery and the discovery of the reflective properties of radar waves, date back to the 19th century, and by the early 20th century, remote sensing could be performed from aircraft with satellite-borne remote sensing becoming feasible during the 1960s (Cohen, 2000). With advancements in unmanned platforms and more affordable accessibility to space, the number of overhead imagery platforms grows as does the potential for a growing stream of overhead imagery data. Humans may be trained to identify ship wakes from data collected by these platforms but in order to best process a high volume stream of data, automated systems may be required. These automated systems, such as neural networks which identify features in the image through combinations of pixels or data points, are able to consider far more information at a time than a human being could, particularly with comparing sets of images or data together for any correlated features or clusters of pixels. This opens the door for data or sensor fusion where combinations of sensors may be utilized to exploit the advantage of each different sensor type, whether they are the same sensor modality examining different wavelengths—e.g., multiple SAR sensors examining different SAR frequency bands—or multiple sensor modalities.

The advantages in an automated ship wake detection mechanism are the ability to scan large volumes of overhead imagery for ship wakes. This has applications to ship tracking for defense purposes, law enforcement, and tracking illegal fishing where the ship in question in any of these cases has turned off its automatic identification system. The methodology presented here can also be extended to other identification problems concerning remote sensing data, including road detection from satellite imagery, land use classification, and resource management.

Work covered in this dissertation exists at the intersection of several disciplines: computational mechanics, physical oceanography, electro-optical sensor modeling, machine learning, and data fusion, each of which are covered in detail within this dissertation. The remainder of the first chapter contains the literature review, and the second chapter covers the physical hydrodynamic and computational mechanics–based simulations of a ship wake on the ocean surface. First, the time-varying simulation of a surface ship wake is performed followed by a simulation to calculate the redistribution of surfactants on the ocean surface due to the turbulence and velocity generated by the ship's passage. The third simulation calculates the resulting surface wind wave spectrum on the simulated ocean surface. The third chapter concerns the simulation of synthetic aperture radar and infrared remote sensing images using the data generated by the hydrodynamic simulations. This includes an overview of the sensor models. The fourth chapter covers the neural network–based classification models that are used to detect ship wakes within remote sensing data, as well as the training and evaluation details. The fifth chapter discusses data fusion including multi-sensor data fusion, and the sixth covers the conclusions and future work.

1.2 Literature Review

Remote sensing applications and platforms have proliferated in recent decades, particularly with respect to global environment monitoring. Satellites such as Terra and the Sentinel series have paved the way for high-quality remote sensing for scientific data acquisition and monitoring (Campbell and Wynne, 2011; Malenovský et al., 2012). Satellite-borne infrared radiometry (IR) sensors aid in monitoring sea surface temperature around the world, which helps quantify climate change and understand global currents. These orbital platforms are often equipped with multiple scientific sensors to enable data collection across a wide range of the electromagnetic (EM) spectrum, which enables the observation of a wide range of phenomena. Infrared waves of different wavelengths, for example, are emitted and reflected by the sea surface differently which means that certain regimes of the EM spectrum may have different uses in sea surface observation (Minnett et al., 2019).

Radar and synthetic aperture radar (SAR) sensors are also commonly integrated into earth observation satellites, which can be used for recording topology and even ocean currents (Gens and Van Genderen, 1996) regardless of the time of day or cloud cover. SAR in particular has also been used for detection of vehicles such as ships, either directly through observation of the ship itself (Marino et al., 2015; Velotto et al., 2013; Zhao et al., 2014) or indirectly through observation of the ship wake (Del Prete et al., 2021; Gilman et al., 2011; Graziano et al., 2017; Griffin et al., 1992; Karakus and Achim, 2019; Reed and Milgram, 2002; Stapleton, 1997; Xu et al., 2018), however ship wake detection through infrared and other EM means is also possible (Bunkin et al., 2011; Peltzer et al., 1987; Yang et al., 2015). This raises the possibility of using multiple sensor modalities to perform ship wake detection, which could leverage the strengths of the different sensors to better detect wakes in the ocean. Several different combinations of remote sensing data have been explored, including SAR, IR, electro-optical (EO), and automatic identification system (AIS) information (Druce et al.,

2021; Giompapa et al., 2007; Kim et al., 2016, 2018; Liu et al., 2015; Lu et al., 2015; Zhao et al., 2014).

Many researchers have sought to simulate remote sensors for SAR or other types of EM radiation, and many models have achieved images qualitatively comparable to real-world SAR images. For the marine application of remote sensing, authors have developed models for simulation of EM returns from the ocean surface using SAR (Franceschetti et al., 1998; Li et al., 2022; Rizaev et al., 2022) and IR (Mermelstein et al., 1994; Schwenger and Repasi, 2003); vehicles including the ship hull itself in SAR (Ahmadibebi et al., 2022; Ahmadibeni et al., 2020; Jones et al., 2020; Zhang et al., 2011) and IR (Willers et al., 2011); and the ship wake on the ocean surface in SAR (Ahmadibebi et al., 2022; Jones et al., 2021; Rizaev and Achim, 2022; Rizaev et al., 2022; Somero, 2021) and IR (Issa and Daya, 2014; Yang et al., 2015). Simulations cannot match the level of complexity that occurs in real-world phenomena, however some authors have found advantages to incorporating synthetic data into workflows that have the end goal of being used for real-world applications, either used for transfer learning (Ahmadibeni et al., 2020; Inkawhich et al., 2021; Malmgren-Hansen et al., 2017; Zhu et al., 2021) or as an augmentation to the training data set even if the synthetic data are not photo-realistic (Lewis et al., 2019; Polvara et al., 2020; Tobin et al., 2017; Tremblay et al., 2018; Ødegaard et al., 2016).

Artificial intelligence and computer vision has seen rapid growth in the past two decades and the remote sensing community has been able to leverage this growing potential. Architectures such as YOLO (You Only Look Once) (Redmon et al., 2016) and SSD (Single Shot Detection) (Liu et al., 2016), as well as feature extraction networks such as feature pyramid networks (Lin et al., 2017), have been utilized in remote sensing applications such as object detection and classification (Ding et al., 2023; Muhammad et al., 2018). Neural networks like these and other forms of machine learning have been applied to the study of ship wakes,

some of these are strictly for ship or ship wake detection while others seek to extract data from the ship wakes related to the ships that made them Graziano et al. (2016, 2019); Kang and Kim (2019); Zilman et al. (2004, 2015).

Data fusion, particularly data observed by multiple sensors, has been well-studied in the past. There are three different levels of data fusion for remote sensing: pixel-level data fusion, feature-level data fusion, and decision-level data fusion (Chang and Bai, 2018). The first level seeks to combine separate images or data sources at the data or pixel level, which can be accomplished through different means including principal component analysis and wavelet transforms (Jin et al., 2006). Feature-level fusion extracts features from different data inputs and performs an analysis on these extracted features. The features fused in this method may be abstract unlike pixel-level fusion where the pixel-based representation of the image or data is retained, and features that are fused may be selected through hand-picked or machine-learned means (Gunatilaka and Baertlein, 2001; Khazaee et al., 2013). The third data fusion paradigm, decision-level fusion, departs from fusion during or before the analysis and instead takes on a meta-analysis approach where several different analysis results are weighed together to form a final conclusion. Li et al. (2015) reviews several multi-sensor data fusion methods, particularly those utilizing consensus techniques which may be applicable for decision-level fusion. Other decision-level data fusion models include Bayes' theorem-based models, Dempster–Shafer theory, fuzzy logic, and Kalman filters (Buede and Girardi, 1997; Lu et al., 2015; Olfati-Saber, 2009; Solaiman et al., 1999).

The goal of this dissertation is to build a simulation workflow that allows for the generation of simulated remote sensing data for the purpose of developing machine learning–based models to detect ship wakes in remote sensing images. These simulation models are developed from first principles and empirical formulations that seek to maintain a high level of fidelity in the simulations, and therefore generate data that is representative of real-world remote

sensing data. Once the data are collected and curated, the neural network–based models can be trained and developed in order to provide preliminary results pertaining to ship wake detection. These neural networks are trained and evaluated without any data fusion means, and data fusion models are implemented and tested in the hopes to understand the relative impact of data fusion in this exemplar problem. Being able to perform all these simulations and studies in one streamlined workflow may aid in the development and deployment of real-world systems, whether they seek to detect ship wakes or any other phenomena in remote sensing images.

1.3 Agenda

Building upon these past efforts, this work seeks to combine the concept of generating synthetic remote sensing data using proven physics-based modeling and simulation tools, in order to create a digital testbed for machine learning–enabled data fusion algorithms. This aspect of generating synthetic data allows researchers to focus on prototyping wake detection models without requiring real world data to be collected or furnished prior to model development. This may yield advantages particularly for cases where existing data sets are limited or not commercially available, particularly for data fusion models where spatially- and temporally-correlated data sets from several remote sensing instruments are needed. Ultimately, it is the author's goal to develop an autonomous detection system that ingests multiple remote sensing data streams in real-time, and provides information to decision makers in a human-on-the-loop manner. The following work describes incremental progress toward this goal and builds on prior modeling and simulation methodologies, and the primary novel contributions of this dissertation lie in the infrared sensor simulation model and the machine learning and data fusion aspects of the paper.

Chapter 2

Surface Ship Wake Hydrodynamics

The remote sensing data used in this project are derived from computational models that use simulated hydrodynamic data as the basis for the ocean surface. These simulated hydrodynamic data are calculated using OpenFOAM with physics-based models that allow for the complex interaction of the ship-induced velocity and turbulence wake, swell, and sub-surface stratified fluid dynamics to play out in a realistic manner.

The simulation of the wake is divided into three parts: first, a time-varying simulation where the evolution of the wake is simulated over the span of an hour; second, a steady simulation to determine the ship wake–induced redistribution of surface active substances (SAS) or surfactants on the surface of the ocean; and third, a surface roughness modification of the ocean surface wake spectrum caused by the ship including redistribution of SAS. Data from each of these simulations feeds into later simulations in a one-way coupled manner as shown in Figure 2.1 which also highlights the interconnectedness of various parameters relating to the ship, the aerial platform, and the ocean environment in the simulation workflow. The end result is a collection of data from a simulated ocean surface that can be used as a basis for the generation of simulated remote sensing data, particularly SAR and IR images.

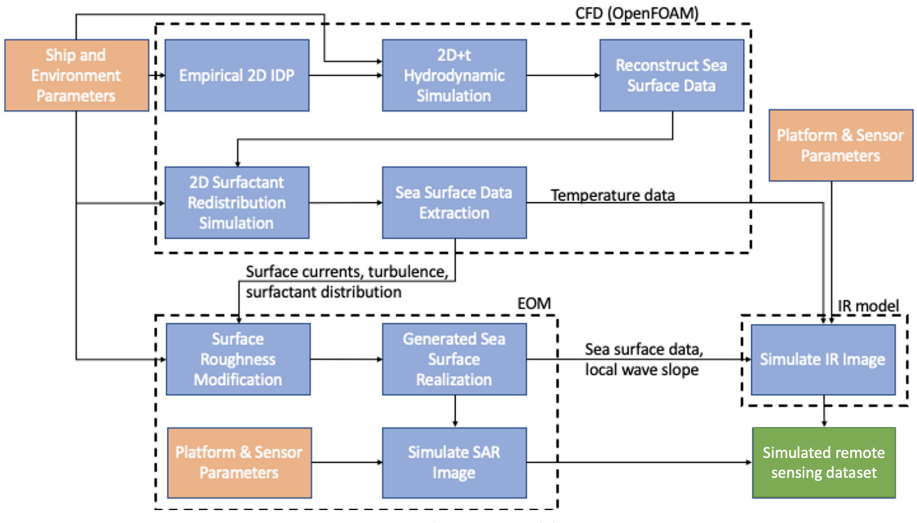

Figure 2.1: The multiple simulation components of the data generation process and the flow of data between them.

2.1 Modeling & Simulation of the 3D Flow Field

2.1.1 Governing Equations

An unsteady RANS (Reynolds averaged Navier–Stokes) approach is used in the first hydrodynamic simulation. All variable fields are decomposed into a time-averaged component and a fluctuating component then this decomposition is substituted into the Navier–Stokes equations for an incompressible fluid to yield the unsteady RANS equations in Equations (2.2) and (2.3). The Boussinesq approximation for buoyancy force is used in the latter equation, allowing for density differences within the domain to result in buoyant forcing.

The TEOS-10 equation of state is used in this simulation in order to calculate the density of the fluid (IOC et al., 2010). Equation (2.4) gives a representative form of this equation of state as a function of temperature T, salinity S, depth z, latitude ϕ_l, and longitude θ_l. Reference density ρ_{ref} in Equation (2.3) is equivalent to the background density ρ_b which itself is a function of background temperature T_b and salinity S_b.

The effects of swell are incorporated into the domain without explicitly resolution of the ocean surface through the Craik–Leibovich vortex force (Craik and Leibovich, 1976). This model is given in Equation (2.6) and is a function of the Stokes drift velocity $u_{S,i}$ and the vorticity of the fluid ω which is the curl of the velocity field. Stokes drift velocity is given by Equation (2.1) as a function of swell amplitude a_s, swell wavelength λ, the magnitude of gravity, and the z spatial coordinate. This forcing term is responsible for much of the velocity wake–ocean swell interaction that produces persistent ship wakes (Somero et al., 2018).

$$u_{S,i} = \left(2\pi\frac{a_s}{\lambda}\right)^2 \sqrt{\frac{g\lambda}{2\pi}} \exp\left(4\pi\frac{z}{\lambda}\right) \tag{2.1}$$

$$\frac{\partial U_i}{\partial x_i} = 0 \tag{2.2}$$

$$\frac{\partial U_i}{\partial t} + U_j\frac{\partial U_i}{\partial x_j} - \frac{\partial}{\partial x_j}\left[(\nu+\nu_t)\left(\frac{\partial U_i}{\partial x_j} + \frac{\partial U_j}{\partial x_i}\right)\right] = -\frac{\partial p}{\partial x_i} + f_{i,buoy} + f_{i,vortex} \tag{2.3}$$

$$\rho(\vec{x},t) = f(T(\vec{x},t), S(\vec{x,t}), z, \phi_l, \theta_l) \tag{2.4}$$

$$f_{i,buoy} = g_i\frac{\rho-\rho_{ref}}{\rho_{ref}} \tag{2.5}$$

$$f_{i,vortex} = \epsilon_{ijk}u_{S,i}\omega_j \tag{2.6}$$

Additionally, the multi-scale localized perturbation method is used to decompose several simulation fields into a background quantity, denoted with a subscript b, and a perturbation quantity, denoted with a prefix δ, as shown with a demonstrative variable $f(\vec{x},t)$ that varies with location $\vec{x}$ and time t in Equation (2.7) (Higgins et al., 2020; Higgins, 2020).

$$f(\vec{x},t) = f_b(\vec{x},t) + \delta f(\vec{x},t) \tag{2.7}$$

Let $PDE(f) = 0$ be an arbitrary partial differential equation that takes $f(\vec{x},t)$ as a variable. If we substitute $f_b(\vec{x},t) + \delta f(\vec{x},t)$ in for $f(\vec{x},t)$, the differential equation can be denoted in two equivalent ways as shown in Equation (2.8) where the term $NL(f_b, \delta f)$ notes any additional terms that arise from non-linearity in $PDE(f)$; if the partial differential equation is linear, as is the case with the partial differential equation $\frac{\partial U_i}{\partial x_i} = 0$, then $NL(f_b, \delta f)$ will be identically zero.

$$PDE(f_b + \delta f) = PDE(f_b) + PDE(\delta f) + NL(f_b, \delta f) = 0 \tag{2.8}$$

The purpose of this decomposition is to allow for a known background value of a variable to be defined within the domain, for example, an ambient temperature stratification that is largely influenced by large-scale oceanic currents and diurnal forcing that a small-scale, short-duration simulation would not be able to resolve. In the case of these simulations, the background variables are assumed to be constant in time and varying only in the vertical direction.

This process is not simply offsetting the value of the variable at each location in the domain, but rather it defines the background and deviation from the background as separate variables with the assumption that the background evolves far slower and over greater length scales than the perturbation does, to the degree that it is assumed that the perturbation does not have an effect on the background fluid dynamics. In other words, the background is assumed to evolve independently of the perturbation, however, the evolution of the perturbation may be influenced by the background in a way that couples the perturbation to the background

but not the other way around. This system can then be defined using the following partial differential equations

$$PDE(f_b) = 0$$
$$PDE(f_b) + PDE(\delta f) + NL(f_b, \delta f) = 0$$

which simplify to

$$PDE(f_b) = 0$$
$$PDE(\delta f) + NL(f_b, \delta f) = 0$$

One may note that the latter equation can be understood as $PDE(f_b + \delta f) - PDE(f_b) = 0$, which quantifies the dynamics of the perturbation variable separately from the dynamics of the background while still retaining the non-linear interaction between the background and perturbation. Since the background field in this case is known *a priori*, only the latter equation needs to be solved. This results in a modified set of governing equations with additional terms representing the influence of non-linear interaction between the background and perturbation fields upon the perturbation fields. Variables in this section that are not decomposed in this manner can be understood as being the perturbation from an identically-zero background with the δ prefix omitted for brevity.

Turbulence modeling in stratified fluids, particularly in ship wakes, is a complex matter as Wall (2021) examines. The simulations here are performed with a RANS turbulence model which sacrifices a degree of realism for a reduced computational load. A buoyant

k–ϵ turbulence model developed by Rodi (1987) is used to model the Reynolds stress in the RANS formulation. This model extends the original k–ϵ turbulence model from Launder and Spalding (1974) by allowing density stratification to generate or attenuate turbulence kinetic energy and its dissipation rate in unstable or stable stratification, respectively. Turbulent kinetic energy (TKE) k, dissipation rate of TKE ϵ, and eddy viscosity ν_t are defined in Equations (2.9)–(2.11). Expressions for shear production of TKE P and buoyancy production of TKE G are given in Equations (2.12) and (2.13). Here, β_T is the coefficient of thermal expansion of seawater and g_i is the gravity vector. Constants $C_{1\epsilon} = 1.44$, $C_{2\epsilon} = 1.92$, and $\sigma_\epsilon = 1.3$ in accordance with Rodi (1987); Rodi offers a range of possible values for $C_{3\epsilon}$ but this constant is arbitrarily taken as 0.144 here. The remaining coefficients have values of $\sigma_t = 1$, $\sigma_k = 1$, and $C_\mu = 0.09$, the latter two being adapted from Launder and Spalding (1974).

$$\frac{\partial k}{\partial t} + U_i \frac{\partial k}{\partial x_i} - \frac{\partial}{\partial x_i}\left[\frac{\nu_t}{\sigma_k}\frac{\partial k}{\partial x_i}\right] = P + G - \epsilon \tag{2.9}$$

$$\frac{\partial \epsilon}{\partial t} + U_i \frac{\partial \epsilon}{\partial x_i} - \frac{\partial}{\partial x_i}\left[\frac{\nu_t}{\sigma_\epsilon}\frac{\partial \epsilon}{\partial x_i}\right] = c_{1\epsilon}\frac{\epsilon}{k}\left(P + C_{3\epsilon}G\right) - C_{2\epsilon}\frac{\epsilon^2}{k} \tag{2.10}$$

$$\nu_t = C_\mu \frac{k^2}{\epsilon} \tag{2.11}$$

$$P = \nu_t \left(\frac{\partial U_i}{\partial x_j} + \frac{\partial U_j}{\partial x_i}\right)\frac{\partial U_i}{\partial x_j} \tag{2.12}$$

$$G = \beta_T g_i \frac{\partial T}{\partial x_i}\frac{\nu_t}{\sigma_t} \tag{2.13}$$

The buoyancy TKE source G may be defined in terms of a stratifying variable such as temperature T or salinity S for seawater, however this may equivalently be written in terms of density using the coefficient of thermal expansion definition of $\beta_T \equiv (1/\rho_{ref})\partial\rho/\partial T$. Using this knowledge, G may also be defined in terms of Brunt–Väisälä frequency N as shown in

Equation (2.14) which illustrates influence of stratification on G.

$$G = \beta_T g_i \frac{\partial T}{\partial x_i} \frac{\nu_t}{\sigma_t} = \frac{g_i}{\rho_{ref}} \frac{\partial \rho}{\partial x_i} \frac{\nu_t}{\sigma_t} = N^2 \frac{\nu_t}{\sigma_t} \tag{2.14}$$

The sea surface introduces turbulent anisotropy through suppression of turbulent motions in the vertical direction, and this change in turbulence may have an effect on wake development, especially on the ship wake at the very surface of the ocean. While this turbulence suppression was not modeled in these simulations, Somero (2021) proposes a modified k–ϵ turbulence model that models this effect. This model redistributes the vertical turbulent stresses into horizontal ones as a function of distance from the ocean surface z and is derived from experimental data collected from turbulent axisymmetric jets near a free surface that may approximate turbulent jets emitted from ship propulsors. The revised model produces a modified Reynolds stress tensor that consists of a Reynolds stress tensor calculated by a nominal k–ϵ to which the values calculated in Equations (2.15)–(2.20) are added to the respective tensor components:

$$\overline{u'^2}_{correction} = \frac{2}{3 + 1/f(z)} \overline{w'^2}_{k-\epsilon} \tag{2.15}$$

$$\overline{v'^2}_{correction} = \frac{1}{3 + 1/f(z)} \overline{w'^2}_{k-\epsilon} \tag{2.16}$$

$$\overline{w'^2}_{correction} = -\frac{1}{1 + \frac{1}{2f(z)}} \overline{w'^2}_{k-\epsilon} \tag{2.17}$$

$$\overline{u'w'}_{correction} = -\frac{1}{1 + \frac{2}{3f(z)}} \overline{u'w'}_{k-\epsilon} \tag{2.18}$$

$$\overline{v'w'}_{correction} = -\frac{1}{1 + \frac{2}{3f(z)}} \overline{v'w'}_{k-\epsilon} \tag{2.19}$$

$$\overline{u'v'}_{correction} = 0 \tag{2.20}$$

$$f(z) = \left(\frac{Ck^{3/2}}{\epsilon z} \right)^a \tag{2.21}$$

Equation (2.21) represents a wall factor based on the local turbulence length scale and is derived from Launder (1989), and Somero (2021) gives the constant C as 0.07 and the constant a as 2.

These equations show that as distance from the surface z decreases to zero, $1/f(z)$ correspondingly decreases to zero which results in up to two-thirds of the vertical turbulent normal stress being redistributed to the streamwise turbulent fluctuations $\overline{u'^2}$ and the remaining one-third being redistributed to the transverse turbulent normal stress $\overline{v'^2}$. The turbulent shear stresses $\overline{u'w'}$ and $\overline{v'w'}$ also decrease to zero in the limit that the distance from the wall approaches zero while the $\overline{u'v'}$ turbulent shear stress component is unaffected by the presence of the free surface. Conversely, as distance from the free surface increases, all of these correction factors decrease to zero which returns the Reynolds stress tensor to its original k–ϵ value. While this model is not used in these simulations, simulations with this model and potentially the combination of this model with the one utilized in this work,

which accounts for buoyant suppression of turbulence, may be of interest for the case of a ship traveling through a portion of ocean with strong near-surface stratification.

Temperature and salinity are important quantities that may be transported throughout the domain due to the interaction of the ship wake with its environment. Basing this approach off of the one developed in Higgins (2020) and described earlier in this section, temperature T and salinity S are composed into a constant yet vertically-varying background field, respectively T_b and S_b, as well as a time- and space-varying perturbation from this background field denoted by δT and δS such that $T(\vec{x},t) = T_b(z) + \delta T(\vec{x},t)$ and $S(\vec{x},t) = S_b(z) + \delta S(\vec{x},t)$. As the background components of these fields are constant in time, only the perturbation quantities need to be solved for each time step. Transport of δT and δS are modeled using partial differential equations derived from conservation laws. The left-hand side of these equations represent the familiar time rate of change, convection, and diffusion terms of the conservation of a scalar quantity in a flow, however the right-hand side quantities arise from the interaction of the time-constant background field with the flow including turbulence.

$$\frac{\partial \delta T}{\partial t} + U_i \frac{\partial \delta T}{\partial x_i} - \frac{\partial}{\partial x_i}\left[\left(\frac{\nu}{\sigma_T} + \frac{\nu_t}{\sigma_{t,T}}\right)\frac{\partial \delta T}{\partial x_i}\right] = -U_i \frac{\partial T_b}{\partial x_i} + \frac{\partial}{\partial x_i}\left(\frac{\nu_t}{\sigma_{t,T}}\frac{\partial T_b}{\partial x_i}\right) \tag{2.22}$$

$$\frac{\partial \delta S}{\partial t} + U_i \frac{\partial \delta S}{\partial x_i} - \frac{\partial}{\partial x_i}\left[\left(\frac{\nu}{\sigma_S} + \frac{\nu_t}{\sigma_{t,S}}\right)\frac{\partial \delta S}{\partial x_i}\right] = -U_i \frac{\partial S_b}{\partial x_i} + \frac{\partial}{\partial x_i}\left(\frac{\nu_t}{\sigma_{t,S}}\frac{\partial S_b}{\partial x_i}\right) \tag{2.23}$$

2.1.2 Simulation Details

Computational Domain

This simulation takes place over an hour time late after the ship has passed a specific point in the ocean which simulates a wake that can stretch for tens of kilometers downstream of

the ship with a cross-wake domain size on the order of kilometers and a depth of hundreds of meters. Even under a RANS formulation, this domain is very large, and the computational cost required to simulate this domain on a fine enough resolution to resolve the wake would be extreme, especially if a model of a ship hull were to be placed in the domain and moved in order to generate a wake, as in this case the area around the ship would need to be sufficiently resolved. Several assumptions are made which results in an approach called "2D+t" within this dissertation which has a far simpler domain that is only one cell thick in the direction of the ship's travel that is still results in a representative ship wake simulation.

The full-sized domain is shown in Figure 2.2 and for these simulations is 25 km long, 2 km wide, and 300 m deep. The first assumption is that the domain is fixed relative to the ship which is located just outside of the domain, and that the ship is traveling on a constant trajectory at a constant speed. With the ship outside of the domain, the wake can be introduced into the domain through the use of a boundary condition on the $-x$ face of the domain and the simulation can be performed in a steady manner. This removes the need to march through time as well as the need to refine the computational mesh around the ship hull but the simulation domain remains quite large, and even a 1 m resolution in all three directions would result in a domain with 1.5 billion cells which would make repeated simulations prohibitively costly to run.

The next assumption is that the wake evolves very slowly in the streamwise direction relative to the evolution in the y and z axes in such a way that the derivative in the x direction is nearly zero. In this case, the wake is nearly 2D however a fully 2D, steady simulation would not yield a realistic ship wake, so instead, the domain is changed into an Earth-fixed, time-resolved, 2D domain which the ship has pass through moments before time $t = 0$ of the simulation. Due to the ship's steady speed and course, time is used as a surrogate for distance downstream of the stern and the wake is locally 2D. Equation 2.24 shows how this

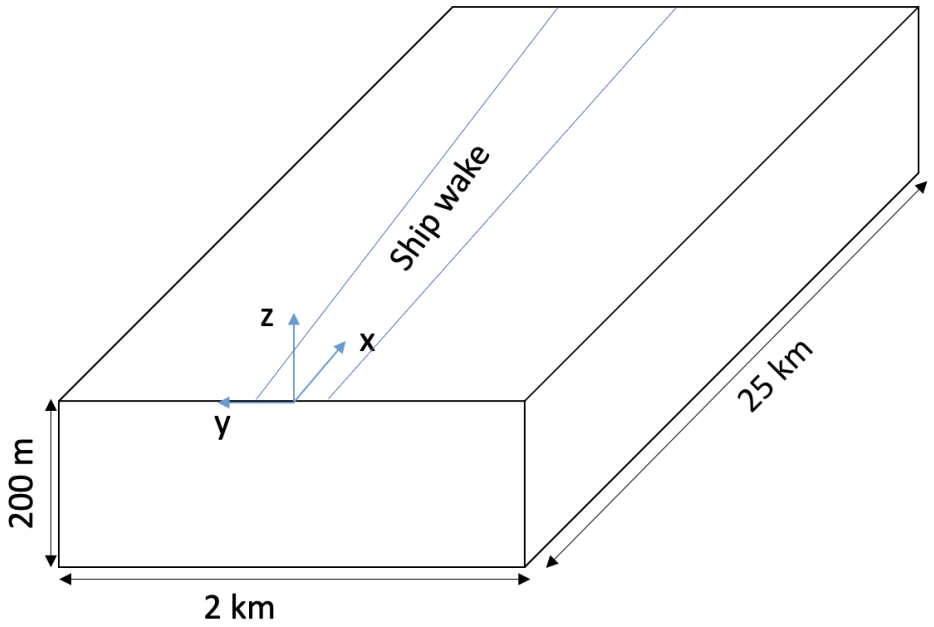

Figure 2.2: Full 3D computational domain with a representative area denoting the ship wake after the ship has traversed the domain along the $-x$ axis. At the end of the simulation, the ship is just outside of the domain near the origin.

is achieved, where Δx_{2D+t} represents the wake length simulated over a $\Delta t_{simulation}$ timespan assuming the ship is maintaining a constant course at speed U_{ship}.

$$\Delta x_{2D+t} = U_{ship} \Delta t_{simulation} \tag{2.24}$$

This results in a 2 km wide, 300 m deep 2D domain that is only one computational cell thick in the direction aligned with the ship's trajectory as Figure 2.3 shows, which is far less computationally expensive to simulate than a 3D domain. This method does have several trade offs in terms of accuracy. While the assumption was that the ship wake evolves slowly in the x direction, the 2D nature of the computational domain forces the x derivatives to be identically zero everywhere. These derivatives can be approximated either during the simulation or in post-processing through a time derivative as shown in Equation (2.25) for

an arbitrary scalar variable ϕ.

$$\frac{\partial \phi}{\partial x} \approx \frac{1}{U_{ship}} \frac{\partial \phi}{\partial t} \tag{2.25}$$

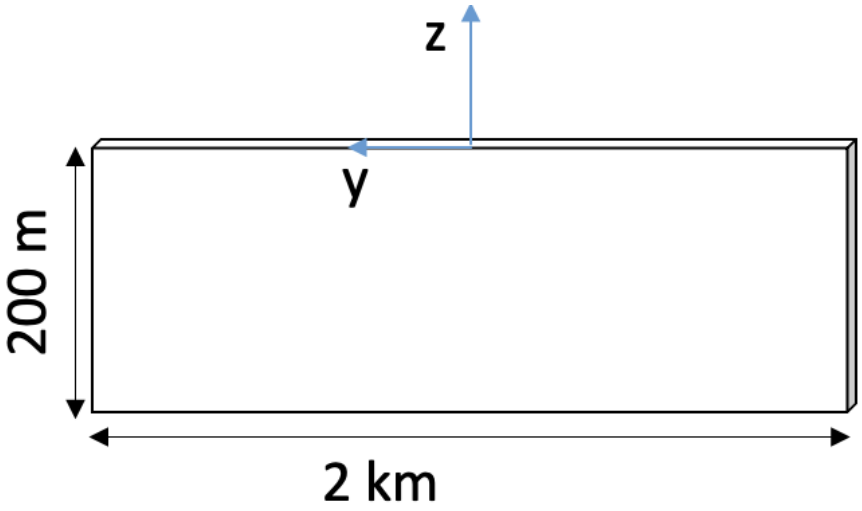

Figure 2.3: The 2D+t domain used in these simulations.

Timestep data are saved over the course of the simulation which can then be offset in the x direction according to the time they were saved at. This creates a collection of 2D slices as shown in Figure 2.4 where the missing data between saved slices being approximated by means of linear interpolation.

The domain is divided into a series of rectangular volumes. The 2000 m-wide domain is divided into 4001 elements horizontally and 201 elements vertically. An additional 500 m region is added on each side of this domain that consists of 101 elements horizontally and 201 elements vertically in each. These regions are used as numerical beaches with damping applied to them that progressively becomes stronger as distance from the origin increases. Additionally, the cells in these beach regions are not uniformly sized with cells progressively becoming longer in the y dimension as they get further from the origin. The purpose of these

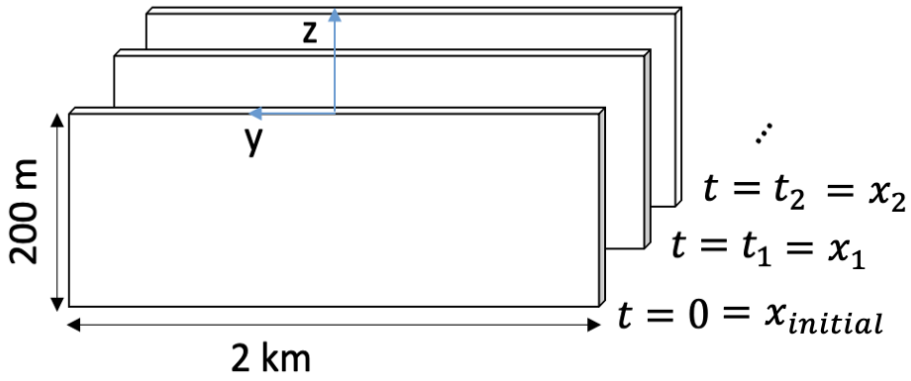

Figure 2.4: Timestep data from the 2D+t domain are transformed using a Galilean transform to convert time after the ship transit into distance downstream of the ship.

beaches is to prevent internal gravity waves or other elements of the flow from reflecting off of the computational boundary and returning to the center of the domain where they may interfere with the wake.

Initial and Boundary Conditions

Initial conditions related to the surface ship wake are initialized from empirical models in lieu of running a CFD simulation of the surface ship. The calculated initial data plane (IDP) is situated half a boat length downstream, and the models described by Miner et al. (1988) are used along with ship-specific dimensions chosen by Somero et al. (2018). The latter authors select the DDG-5415 as a ship from which the prototypical wake originates, and these equations and values are summarized in this section. Constants are listed in Tables 2.1 and 2.2.

The velocity wake of a ship is produced by thrust from the propellers (subscript p), drag from the body (subscript f) and rudders (subscript r), and a contribution from wave-breaking caused by the ship (subscript w). The initial axial (streamwise) velocity field $U_0(y, z) = U(y, z, t = 0)$ is composed of these separate contributions written as

Table 2.1: Ship and environment dimensions as well as empirical coefficients used for the IDP model.

Variable name	Symbol	Value
Length	L	142 m
Beam	B	18.9 m
Draft	D	6.16 m
Wetted surface area	S	2949.5 m^2
Propeller diameter	D_p	5.29 m
Propeller horizontal offset	y_p	4.2 m
Propeller axle depth	z_p	5.11 m
Rudder horizontal offset	y_r	3.16 m
Rudder mid-span depth	z_r	1.76 m
Rudder thickness	t_r	0.95 m
Rudder chord	c_r	6.33 m
Rudder planform area	S_r	12.1 m^2
Ship velocity	U_{ship}	7 m/s
Seawater kinematic viscosity	ν	10^{-6} m^2/s
Seawater reference density	ρ_0	1025 kg/m^3
Reynolds number	Re	9.94×10^8
Froude number	Fr	0.188
Propeller diameter	D_p	5.29 m
Swirl number	$\tilde{S}$	0.3
Rudder drag coefficient	C_{dr}	0.0093
Hull wave-making drag coefficient	C_R	0.002

$$U_0(y,z) = U_p(y,z) - (U_f(y,z) + U_r(y,z) + U_w(y,z)) \tag{2.26}$$

and the initial TKE field $k_0(y,z) = k(y,z,t=0)$ and TKE dissipation rate field $\epsilon_0(y,z) = \epsilon(y,z,t=0)$ follow a similar parameterization

$$k_0(y,z) = k_p(y,z) + k_f(y,z) + k_r(y,z).$$

Table 2.2: Ship and environment dimensions as well as empirical coefficients used for the IDP model.

Symbol	Value
$\tilde{a}_1$	1.35
$\tilde{a}_2$	1.0
$\tilde{a}_3$	0.45
$\tilde{a}_4$	8.22
$\tilde{a}$	2.6
$\tilde{a}_p$	2.45
$\tilde{a}_{s1}$	4.34
$\tilde{a}_{s2}$	3.56
α_θ	0.5
c_δ	1.14

$$\epsilon_0(y,z) = \epsilon_p(y,z) + \epsilon_f(y,z) + \epsilon_r(y,z).$$

Swirl from the propellers also introduces a spiral velocity perturbation that is included in the IDP.

The drag profile of the hull is approximated using a Gaussian profile given in Equation (2.27) with a drag-induced turbulence kinetic energy profile given by Equation (2.28). Somero et al. (2018) uses a relationship from Hassid (1980) to relate TKE dissipation rate to the TKE generated by the hull drag and this relationship is given in Equation (2.29)

$$U_f(y,z) = U_{f,max} \exp\left\{-3.5\tilde{a}\left[\left(\frac{y \pm 0.3B}{y_h}\right)^2 + \left(\frac{z}{z_h}\right)^2\right]\right\} \tag{2.27}$$

$$k_f(y,z) = k_{f,max}\tilde{a_1}\exp\left\{-\tilde{a_2}\left[\left(\frac{y}{y_h}\right)^2+\left(\frac{z}{z_h}\right)^2\right]\right\} - k_{f,max}\tilde{a_3}\exp\left\{-\tilde{a_4}\left[\left(\frac{y}{y_h}\right)^2+\left(\frac{z}{z_h}\right)^2\right]\right\} \tag{2.28}$$

$$\epsilon_f(y,z) = \sqrt{\frac{24U_{f,max}}{C_D B^2 U_{ship}}}k_f^{3/2} \tag{2.29}$$

where the hull wake half-width y_h and half-depth z_h are derived from the expected wake size at the IDP downstream location $x_{IDP} = 0.5L$ downstream of the ship and assume that the ship hull can be modeled as a flat plate for the purposes of drag, and these variables are calculated using Equations (2.30) and (2.31), respectively. Momentum thickness θ is given by Equation (2.32), virtual origin x_0 by Equation (2.33), hull drag coefficient C_D by Equation (2.34) which is derived from the hull friction coefficient C_f calculated using Equation (2.35). The maximum friction wake velocity $U_{f,max}$ is calculated using Equation (2.37) which is also used to calculate the maximum hull friction wake TKE $k_{f,max}$ using Equation (2.38).

$$y_h = \theta c_\delta \left(\frac{x_{IDP} - x_0}{\theta} \right)^{1/3} \tag{2.30}$$

$$z_h = 0.5 y_h \left(\frac{B}{2D} \right)^{-2/3} \tag{2.31}$$

$$\theta = \sqrt{\frac{C_D B^2}{8}} \tag{2.32}$$

$$x_0 = \theta \left(\frac{-\sqrt{8}\alpha_\theta}{c_\delta \sqrt{C_D}} \right)^3 \tag{2.33}$$

$$C_D = C_f \frac{S}{B^2} \tag{2.34}$$

$$C_f = \frac{0.075}{\left(\log_{10}(Re) - 2\right)^2} \tag{2.35}$$

$$x_{IDP} = 0.5L \tag{2.36}$$

$$U_{f,max} = \frac{\tilde{a} U_{ship} S C_f}{\pi y_h z_h} \tag{2.37}$$

$$k_{f,max} = (0.3 U_{f,max})^2 \tag{2.38}$$

The ship loses energy to its surroundings through the formation of waves as it drives through the ocean. This loss contributes a velocity field to the IDP which is again modeled assuming a Gaussian distribution. The axial velocity component is given by Equation (2.39) where its maximum value $U_{w,max}$ is given by Equation (2.40) and is related to the total wave-making drag R_{max} modeled using Equation (2.41). The distribution is shaped using a wave wake half-width y_{hw} and half-height z_{hw} which are calculated using Equations (2.42) and (2.43).

$$U_w(y,z) = U_{w,max} \exp\left\{-6\tilde{a}\left[\left(\frac{y \pm 0.6B}{y_{hw}}\right)^2 + \left(\frac{z}{z_{hw}}\right)^2\right]\right\} \tag{2.39}$$

$$U_{w,max} = \frac{\tilde{a} R_{wave}}{\pi \rho_0 U_0 y_{hw} z_{hw}} \tag{2.40}$$

$$R_{wave} = 0.5 \rho_0 U_0^2 S C_R \tag{2.41}$$

$$y_{hw} = L/20 \tag{2.42}$$

$$z_{hw} = D \tag{2.43}$$

The velocity and TKE contribution of the propeller is derived by modeling the propeller wake as an axisymmetric, self-similar jet and are given by Equations (2.44) and (2.45), respectively. These are Gaussian in form and are centered on each of the propeller axes. Additionally, Hassid (1980) shows that the TKE dissipation rate is proportional to $k^{3/2}$ and this relationship is adapted from Somero et al. (2018) as shown in Equation (2.46). The ship is assumed to be in steady forward motion, giving each propeller a thrust T equal to half of the drag due to the hull friction and wave drag; drag due to the rudder is neglected. The axial velocity profile due to thrust $U_p(y,z)$ is given using Equation (2.44) with a maximum axial velocity due to thrust $U_{p,max}$ given by Equation (2.47). Thrust and propeller radius r_h are calculated using Equations (2.48) and (2.49), respectively.

$$U_p(y,z) = U_{p,max} \exp\left[-2\tilde{a}_p\left(\frac{\sqrt{(y \pm y_p)^2 + (z - z_p)^2}}{r_h}\right)^2\right] \tag{2.44}$$

$$k_p(y,z) = k_{p,max} \exp\left[-\tilde{a}\left(\frac{\sqrt{(y \pm y_p)^2 + (z - z_p)^2}}{r_h}\right)^2\right] \tag{2.45}$$

$$\epsilon_p(y,z) = \frac{\sqrt{12}}{B} k_p^{3/2} \tag{2.46}$$

$$U_{p,max} = \frac{\tilde{a}T}{\pi\rho_0 U_{ship} r_h^2} \tag{2.47}$$

$$T = 0.5(0.5\rho_0 U_0^2 B^2 C_D + R_{wave}) \tag{2.48}$$

$$r_h = 0.086 x_{IDP} \tag{2.49}$$

$$k_{p,max} = (0.59 u_{p,max})^2 \tag{2.50}$$

Propeller-induced swirl is modeled by adding a tangentially-aligned velocity component to the IDP. The magnitude of this velocity as a function of y and z is given by Equation (2.51) with a maximum magnitude of $V_{s,max}$ in Equation (2.52) which are both dependent on propeller torque Q and an empirical swirl half-radius r_{sh}. These latter quantities are given by Equations (2.53) and (2.54), respectively.

$$V_s(y,z) = V_{s,max}\tilde{a}_{s1}\frac{\sqrt{(y \pm y_p)^2 + (z - z_p)^2}}{r_{sh}} \exp\left[-\tilde{a}_{s2}\left(\frac{\sqrt{(y \pm y_p)^2 + (z - z_p)^2}}{r_{sh}}\right)^2\right] \tag{2.51}$$

$$V_{s,max} = \frac{\tilde{a}_{s2} Q}{\pi\rho_0 U_0 \tilde{a}_{s1} r_{sh}^3} \tag{2.52}$$

$$Q = 0.5\tilde{S}TD_p \tag{2.53}$$

$$r_{sh} = 0.095\sqrt{x_{IDP} B} \tag{2.54}$$

The rudders contribute a velocity and turbulent wake to the IDP. The rudders are modeled as NACA 0015 airfoils, giving them a thickness of 15% relative to their chord. The velocity

wake is given by Equation (2.55), the TKE contribution by Equation (2.56), and the TKE dissipation contribution to the IDP by Equation (2.57). Additional quantities including the maximum velocity deficit $u_{r,max}$ which is given by Equation (2.58), maximum TKE contribution $k_{r,max}$ defined using Equation (2.59), rudder wake half-width y_{rh} and half-height z_{rh} by Equations (2.60) and (2.61), empirical constant $\tilde{a}_r$ by Equation (2.62).

$$U_r(y,z) = U_{r,max} \exp\left[-\tilde{a}\left(\frac{y \pm y_r}{y_{rh}}\right)^2 + \left(\frac{z - z_r}{z_{rh}}\right)^2\right] \tag{2.55}$$

$$\begin{aligned} k_r(y,z) =& k_{r,max}\tilde{a}_1 \exp\left\{-\tilde{a}_2\left[\left(\frac{y}{y_{rh}}\right)^2 + \left(\frac{z}{z_{rh}}\right)^2\right]\right\} \\ &- k_{r,max}\tilde{a}_3 \exp\left\{-\tilde{a}_4\left[\left(\frac{y \pm 0.3B}{y_{rh}}\right)^2 + \left(\frac{z}{z_{rh}}\right)^2\right]\right\} \end{aligned} \tag{2.56}$$

$$\epsilon_r(y,z) = \sqrt{\frac{24U_{r,max}}{C_d B^2 U_{ship}}} k_r^{3/2} \tag{2.57}$$

$$U_{r,max} = \frac{\tilde{a}_r U_{ship} S_r C_{dr}}{2\pi y_{rh} z_{rh}} \tag{2.58}$$

$$k_{r,max} = u_{r,max}^2 \tag{2.59}$$

$$y_{rh} = \tilde{a}_r \sqrt{x_{IDP} t_r} + 0.5 t_r \tag{2.60}$$

$$z_{rh} = \frac{S_r}{2c_r} \tag{2.61}$$

$$\tilde{a}_r = 0.23\sqrt{C_{dr}} \tag{2.62}$$

Boundary Conditions

In this simulation, the sea surface is modeled as a rigid lid with a free-slip boundary condition applied, meaning that the height of the ocean surface does not fluctuate according to perturbations caused by the ship wake nor is there a turbulent boundary layer caused by the ocean surface. Waves on the surface and their resulting deformation to the free surface are not calculated in this portion of the simulation with wind waves being simulated at a later step. This results in a reduced computational cost in the simulation at the cost of the loss of physics related to the deformation of the surface. Note that the effects of swell on and near the surface are modeled in the simulation through a vortex forcing term, meaning that swell can still influence the domain even though the free surface is assumed to be rigid. The bottom boundary is similarly treated as a free slip surface.

The lateral boundaries are modeled as outlets but as mentioned before, the region of space closest to the lateral boundaries have a damping beach applied to them with the aim of preventing any internal gravity waves from reaching the lateral boundaries. The streamwise boundaries are periodic which in combination with the one cell thick domain enforces the 2D+t natural.

Numerical Methods

These simulations use the PISO (pressure-implicit with splitting of operators to solve for the velocity and pressure fields of the flow Issa (1986). This step splits the differential equation solution into two steps: a velocity estimation followed by a pressure correction loop.

The first step discretizes the conservation of momentum equation in Equation (2.3) into the following matrix equation form in Equation (2.63), where A and H are matrices, U_i^* is a vector of uncorrected cell-center velocities, p_i^* is the cell-center pressure calculated in the

previous timestep, and $f_{body,i}$ are the cell-center body forces applied to the fluid for each cell. Other than p_i^*, all other values are calculated for the current timestep; the elements of A and H are calculated using the discretization schemes selected for the given cases and U_i^* is calculated through standard solvers that are provided within OpenFOAM.

$$AU_i^* = H - \nabla p_i^* + f_{body,i} \tag{2.63}$$

Next, the pressure field is calculated for the current solver timestep and this information is used to correct the momentum of the fluid for the current timestep. Two variables are recast: U_i^* is substituted with U_i^{**}, which refers to the corrected velocity for the current timestep, and p_i^* is recast as p_i^{**} which represents the updated pressure field. Left-multiplying both sides of Equation (2.63) by the inverse of A and taking the divergence of both sides yields Equation (2.64).

$$\nabla \cdot U_i^{**} = \nabla \cdot \left(A^{-1}H - A^{-1}\nabla p_i^{**} + A^{-1} f_{body,i}\right) \tag{2.64}$$

Here, we are modeling the seawater as an incompressible fluid which means that the corrected velocity field will be divergence free and thus the left side of the above equation is identically zero. Further rearrangement and simplification results in a Poisson-type equation for the current timestep pressure field shown in Equation (2.65).

$$\nabla \cdot \left(A^{-1}\nabla p_i^{**}\right) = \nabla \cdot \left(A^{-1}H + A^{-1} f_{body,i}\right) \tag{2.65}$$

Once again, this equation is solved using standard numerical methods provided by OpenFOAM. Further technical details on this method are summarized in Higgins (2020) for a

similar application.

2.2 Modeling & Simulation of Surfactant Redistribution

The next step of the wake simulation is the simulation of the redistribution of surface active substances (SAS), also called surfactants, on the ocean surface. Velocity and turbulence induced by the passage of the ship, particularly the interaction of surface currents and ocean swell, create regions of converging and diverging flow which will alter the ambient distribution of biological film and debris. The surface tension of the ocean water may therefore be affected by the passage of the ship which in turn may affect SAR returns for that region of ocean.

2.2.1 Governing Equations

The surfactant simulation takes place on a 2D domain which is fixed relative to the ship as opposed to the earth-fixed 2D+t simulation in the previous step. SAS is modeled as a passive scalar concentration Γ that is measured relative to a reference concentration that is convected with surface currents U_i and diffused by molecular and turbulent diffusion as shown by the governing equation given by Equation (2.66). In this case, molecular and turbulent diffusivity of the SAS concentration is equivalent to the molecular viscosity and eddy viscosity of the fluid, the latter being dependent on the ship wake and therefore spatially varying. This is approach is adapted from work outlined by Somero (2021).

$$\frac{\partial \Gamma}{\partial t} + U_i \frac{\partial \Gamma}{\partial x_i} - \frac{\partial}{\partial x_i}\left[(\nu + \nu_t)\frac{\partial \Gamma}{\partial x_i}\right] = 0 \tag{2.66}$$

2.3 Modeling & Simulation of the Surface Wave Spectrum

2.3.1 Governing Equations

The aforementioned 2D+t hydrodynamic simulation and 2D unsteady SAS redistribution simulation represent the direct impact of the ship on the environment, and the next step of understanding the impact of the ship wake on the environment lies in the simulation of the surface wave spectrum. Somero (2021) devises an approach where the surface wave spectral density N is modeled as a function of wind speed, turbulence, and local surface tension. Equation (2.67) where $C_{g,i}$ is the wind wave group velocity, k_i is the wind wave number, β is a wind wave growth factor that is a function of the friction velocity U_*, γ is a damping term that is the superposition of surface tension–based damping γ_s and turbulence-induced damping γ_t, and α is a non-linear wave decay coefficient.

$$\frac{\partial N}{\partial t} + (U_i + C_{g,i}) \frac{\partial N}{\partial x_i} - k_i \frac{\partial U_i}{\partial x_j} \frac{\partial N}{\partial x_j} = (\beta - \gamma) N - \alpha N^2 \tag{2.67}$$

The equation for β in Equation (2.68) is adapted from Plant (1982) where Somero (2021) uses the relationship $U_* = 0.03 U_{wind}$ to link wind speed to wind-wave growth. Here, ω is the intrinsic frequency of the water waves.

$$\beta = 0.04 \frac{k^2}{\omega} U_*^2 \tag{2.68}$$

Somero (2021) presents a model for calculating the damping caused by the presence of SAS γ_s which is given in Equation (2.69). This model incorporates elements several models (Cini

et al., 1987; Milgram et al., 1993a,b; Peltzer et al., 1993) to account for the modification of the surface tension of the ocean surface due to the local concentration of SAS. Here, E is the film elasticity of the SAS film which is related to film pressure Π. γ_s is a function of the uncontaminated fluid density ρ, kinematic viscosity ν, and freshwater surface tension $\tau_w \approx 72$ mN/m. These equations are summarized below, and the reader is referred to Somero (2021) for a more comprehensive overview.

$$\gamma_s = 4\nu k^2 \frac{X + XY - 2X^2}{1 - 2X + 2X^2} \tag{2.69}$$

where

$$\begin{aligned} X &= \frac{|E|k^2}{4\rho\sqrt{\pi^3 \nu f^3}} \\ Y &= \frac{|E|k}{8\pi\rho\nu f} \\ f &= \frac{1}{2\pi}\sqrt{gk + \frac{\tau_w - \Pi}{\rho}k^3} \end{aligned}$$

N is solved as a field in five dimensions: two spatial dimensions, time, and a two-dimension wavenumber space. Limitations in OpenFOAM prevents this from being directly solvable, so ERIM Ocean Model (EOM) is used in the determination of N. This step is conceptually a part of the hydrodynamic simulation, but functionally computed at the same time that the SAR simulations are performed.

Lyzenga and Bennett (1988) The spectral density of the ocean surface elevation $S(k, \phi)$ is approximated using Equation (2.70) where B and c are constants (Lyzenga and Bennett, 1988).

$$S(k, \phi) = Bk^{-c} \tag{2.70}$$

The background wave spectrum in terms of angular frequency is modeled using the Pierson–Moskowitz spectrum which has the form shown in Equation (2.71) where α is 8.1×10^{-3}, β is 0.74, U_{wind} is the wind speed, and g is the magnitude of gravity (Pierson and Moskowitz, 1964).

$$S(\omega) = \left(\alpha g^2/\omega^5\right) \exp\left(-\beta \left[g/U_{wind}\omega\right]^4\right) \tag{2.71}$$

Following the approach of Lyzenga (1986), the computational domain for the ocean surface is discretized into rectangular elements. A sampling window passes over the domain to calculate the surface height field as a function of the surface wave spectral density and wavenumber. The wavenumber space for this sampling window in the x and y directions is discretized into M and N elements, respectively, where the mth k value in the x direction and nth k value in the y direction can be given by Equations (2.72) and (2.73), respectively. Here, L_x and L_y refer to the length of the sampling window in the x and y directions.

$$k_m = \frac{2\pi}{L_x}\left(m - \frac{M}{2}\right) \forall m \in [1, M-1] \tag{2.72}$$

$$k_n = \frac{2\pi}{L_y}\left(n - \frac{N}{2}\right) \forall n \in [1, N-1] \tag{2.73}$$

This process uses a Hanning window which is given for either coordinate direction in Equations (2.74) and (2.75).

A random surface elevation realization within a given sampling window can be calculated through Equation (2.76) where r and ψ are randomly sampled from the intervals $[-1, 1]$ and $[0, 2\pi)$, respectively. This procedure is repeated for every sampling window across the domain with the sampling window translated half a length in each direction with every sample being

added together to calculate the final surface elevation field.

$$w_m = \sqrt{\frac{1}{2} - \frac{1}{2}\cos\left(\frac{2\pi m}{M}\right)} \tag{2.74}$$

$$w_n = \sqrt{\frac{1}{2} - \frac{1}{2}\cos\left(\frac{2\pi n}{N}\right)} \tag{2.75}$$

$$z(m,n) = 2\pi\sqrt{\frac{S(m,n)}{L_x L_y}} w_m w_n r e^{i\psi} \tag{2.76}$$

After this point in the simulation workflow, the ship wake is simulated as well as the redistribution of SAS due to the passage of the ship and its wake. These data are then used to calculate the surface roughness modification which in turn affects the surface wind wave spectrum and the resulting ocean surface elevation. Various data from these simulations are compiled and used in the next step which is the simulation of SAR and IR imagery for the sections of ocean that contain these ship wakes.

Chapter 3

Physics of Electromagnetic Remote Sensors

The remaining computational physics simulations concern simulation of remote sensing equipment in order to produce simulate synthetic aperture radar (SAR) and infra-red (IR) imagery. These models build off of the simulated hydrodynamic outputs calculated in the preceding chapter and are intended to produce synthetic remote sensing data that can be used to train and test machine learning–based wake detection methods or supplement real-world remote sensing data sets.

3.1 Synthetic Aperture Radar (SAR)

3.1.1 Model Overview

The SAR model is adapted from Lyzenga (1986) and Lyzenga and Bennett (1988) as well as Somero (2021). The goal is to be able to simulate a SAR antenna on a moving aerial platform that is observing the ocean surface within the simulated hydrodynamic environment. Several factors such as Doppler shift are accounted for in the SAR return model in order to provide noise that is rooted in physics-based phenomena. This work focuses on three different SAR bands—C, S, and X—whose frequencies are given in Table 3.1.

Table 3.1: List of SAR bands used in this study and the electromagnetic frequencies used for each in the SAR image simulations.

SAR Band	Frequency (GHz)
S	3.1
C	5.3
X	9.6

3.1.2 Model Equations

The radar cross section of the ocean surface is divided into two distinct components which are combined to create the approximate radar cross section in the approach given by Lyzenga and Bennett (1988). One component is radar cross section due to tilted Bragg scattering σ_B which is a function of the surface wave spectral density given in Equation (2.70), and this model is shown in Equation (3.1). The second component is due to specular Bragg scattering σ_S which is given in Equation (2.70).

$$\sigma_B(\theta,\phi) = 8\pi k_0^4 \iint |G(\theta,\xi_x,\xi_y)|^2 S(2k_0\sin\theta',\phi)\, p(\xi_x,\xi_y)\, d\xi_x d\xi_y \tag{3.1}$$

$$\sigma_S(\theta,\phi) = \frac{\pi}{\cos^4\theta}\left|\frac{1-\epsilon}{1+\epsilon}\right| p(\tan\theta,0) \tag{3.2}$$

The perfect SAR (pSAR) return can be calculated through the superposition of the above radar cross section components and the random sea surface elevation realization associated with the simulation using Equation (3.3) where P_x is the size of the pixel in the x direction. pSAR returns differ from regular SAR returns as they do not include the impact of different phenomena that would impact real-world SAR antenna, such as Doppler shift due to the moving SAR platform. It is assumed in these simulations that the entire domain is imaged very quickly so that there is no significant variation in the ocean surface including the wake

region from the beginning of data measurement to the end of data measurement. The reader is referred to Somero (2021) for more details on these phenomena as well as the associated models.

$$\sigma_{pSAR} = \sigma_B + \sigma_S + \frac{z(x + P_x, y) - z(x, y)}{P_x} \frac{\partial(\sigma_B + \sigma_S)}{\partial \theta} \tag{3.3}$$

3.1.3 Example Simulation Results

SAR images can be generated for nearly arbitrary combinations of sensor and platform parameters, such as look angle, incidence angle, polarization, and SAR frequency band used. Figure 3.1 shows how the SAR frequency band used affects the generated SAR image, showing the differences between C-band, S-band, and X-band SAR images. The C-band and X-band images on the left and right, respectively, show a bright streak in that indicates regions of high radar cross section that is indicative of a ship wake. The equivalent S-band image in the middle is similar although one may notice a dark outline surrounding the ship wake that is absent in the other two SAR bands. The difference in wavelengths between the SAR bands may cause different features to become highlighted in the resulting SAR images as different sized waves on the ocean surface reflect the incident SAR waves differently. This may prove beneficial for analyses which look at combinations of SAR images of the same ocean environment.

The ocean environment itself can have a great impact on the generated SAR images. Figure 3.2 shows the effect of swell presence and direction. The left image shows an ocean environment without swell which does not create a noticeable persistent ship wake that are visible in the other two images. The direction of swell also has an impact on the appearance of the ship wake in the middle and right SAR images. The variation in these three images

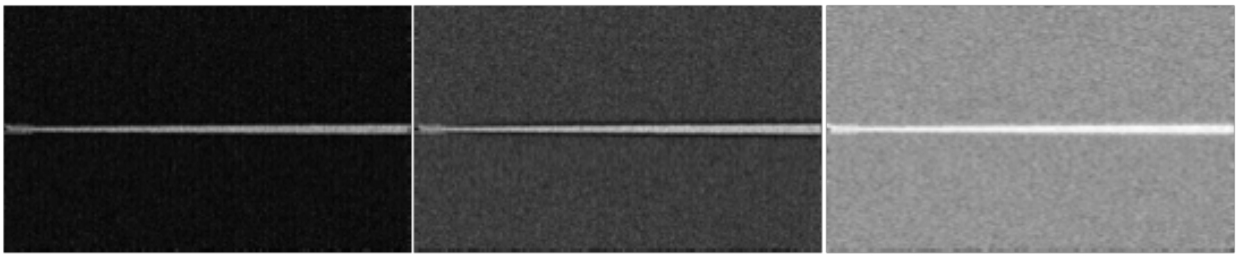

Figure 3.1: Comparison of SAR images across SAR bands. (left) C-band, (middle) S-band, (right) X-band.

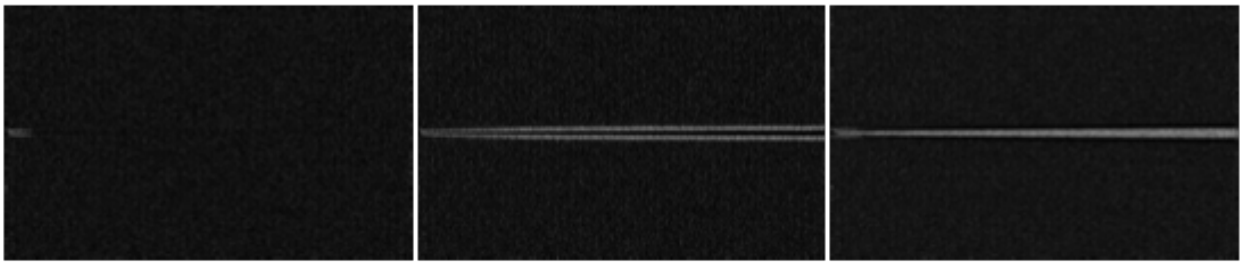

Figure 3.2: Comparison of C-band SAR images for ship wakes in (left) calm seas, (middle) head seas, (right) following seas.

arises from the vortex force term in Equation (2.6).

The next images show the impact of a near-surface temperature gradient on a simulated SAR return. Two cases are set up where all parameters are the same except one case has a linear stratification all the way to the surface while the other has a 20 m deep isothermal layer at the surface and a linear stratification below as shown in Figure 3.3. Figure 3.4 shows the resulting S-band SAR images for these cases where the case with an isothermal layer is on the top and the case with linear stratification everywhere including up to the surface is on the bottom. The passage of the ship mixes the fluid at the surface, drawing colder subsurface water upwards towards the surface. This mixing creates a net buoyancy force near the surface which creates internal gravity waves near the surface that interact with the persistent ship wake further downstream of the boat. These images show how differences in environments can have a major impact on ship wake formation and persistence as observed by simulated SAR sensors.

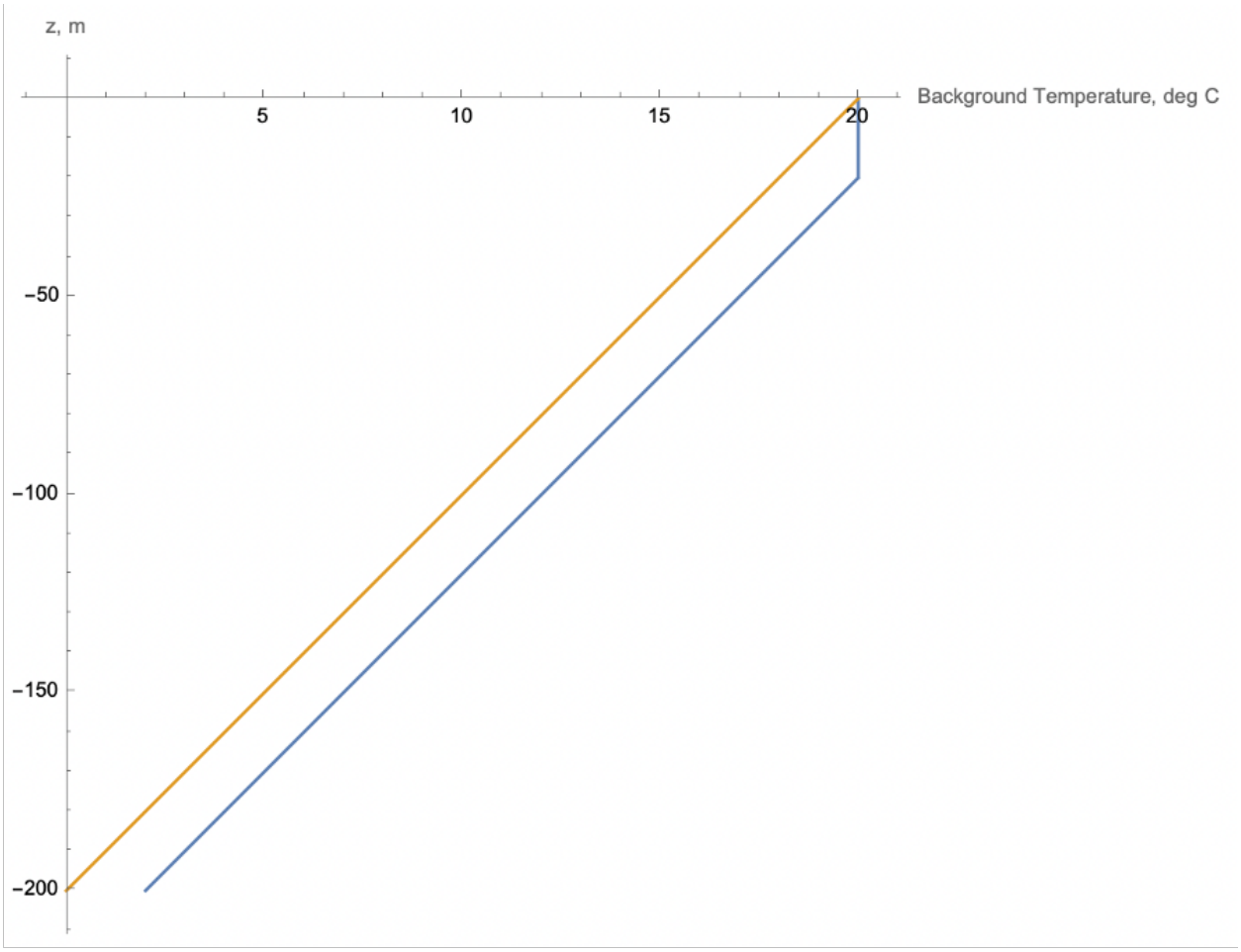

Figure 3.3: Temperature stratification for the images shown in Figure 3.4. One case has an isothermal layer at the surface while the second has a linear stratification throughout.

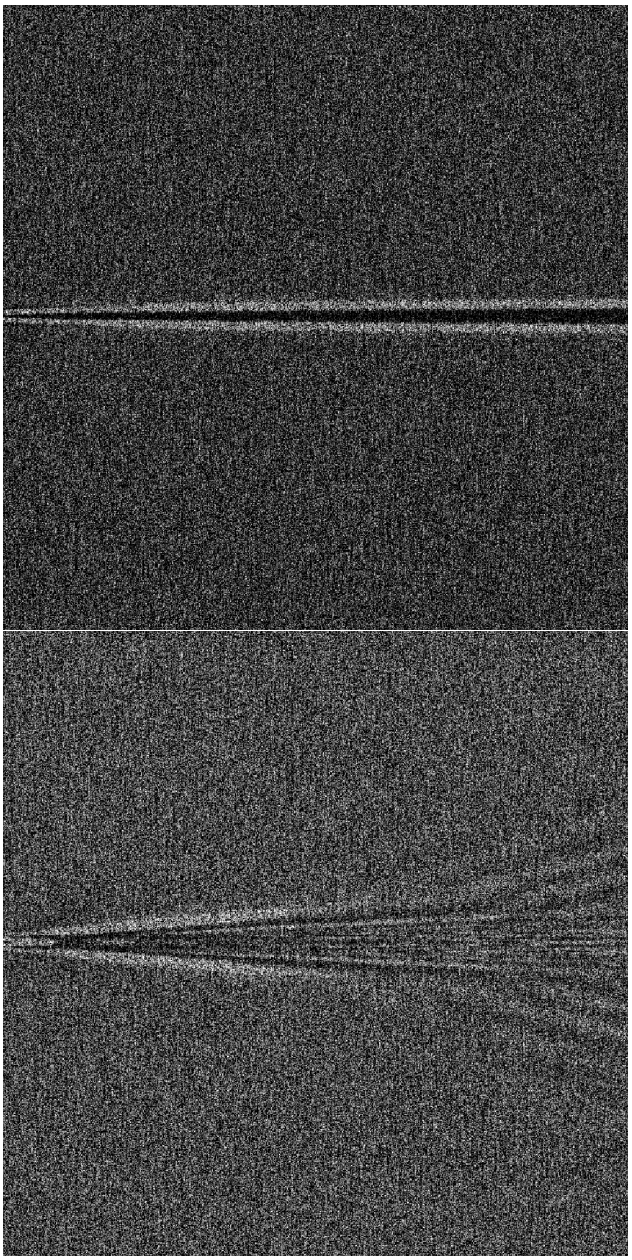

Figure 3.4: S-band SAR images (top) without and (bottom) with a near-surface temperature gradient that causes the formation of internal gravity waves on the surface.

3.2 Infra-red (IR)

3.2.1 Model Overview

Computational models for an IR sensor must account for numerous factors affecting the transmission, reflection, and emission of IR radiation from various sources. These sources include direct solar radiation, scattering and emission of IR radiation by the atmosphere and atmospheric phenomena such as clouds, and surface reflection and emission. These sources can be broken down into two distinct sets of physics, reflected radiation $R_{reflected}$ and emitted radiation that originates on the earth or within its atmosphere $R_{emitted}$. Reflection includes both diffuse reflection, or scattering, and specular reflection, where the former may occur on the earth's surface as well as within the atmosphere whereas the latter only occurs on the earth's surface.

These two sources of radiation that arrive at a simulated sensor may be broken down by origin or source as well as direction relative to the earth's surface. The sun is one of the largest sources of IR radiation which travels through the atmosphere towards the planet's surface. The planetary surface may also emit IR radiation towards an atmospheric sensor. The atmosphere is a source of both downwelling radiation towards the earth's surface as well as upwelling radiation that originates between the earth's surface and the sensor. This atmospheric radiation which radiates in either direction may be emitted by or scattered by the gas molecules. These sources may be represented by the following variables, all of which require a model to quantify: downwelling direct solar IR radiation that reaches the surface R_{sun}, upwelling black-body radiation emitted by the ocean surface R_{sea}, downwelling atmospheric emitted IR radiation or scattered IR radiation from non-solar sources that reaches the surface $R_{atmo,down}$, downwelling in-scattered solar IR radiation $R_{ss,down}$, upwelling atmospheric emitted IR or scattered radiation from non-solar sources that reaches the sensor

$R_{atmo,up}$, and upwelling in-scattering of solar radiation $R_{ss,up}$. These sources are illustrated in Figure 3.5. The downwelling sources and the upwelling surface emission can be combined into a single term R_{surf} for the sake of conciseness. Parameters such as transmissivity τ, emissivity ϵ, and reflectivity ρ require empirical or physical models to fully quantify the IR radiation sources. Here, the emissivity and reflectivity of the planetary surface are related and depend on the local surface slope relative to the incident IR wave.

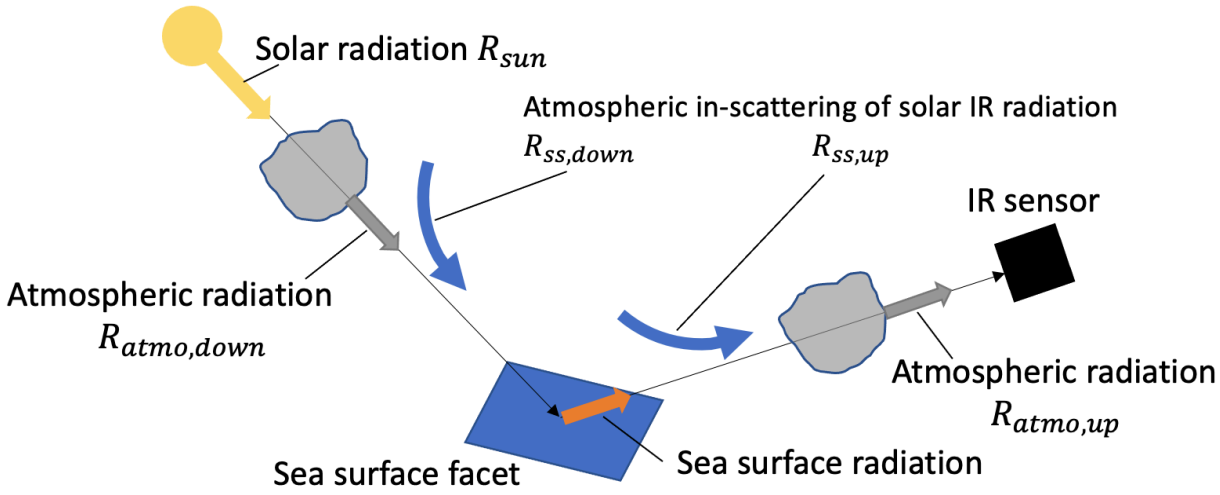

Figure 3.5: Sources of IR radiation that may reach an airborne IR sensor.

IR radiation is polarized, meaning that the aforementioned quantities may differ between the two components of the radiation. Horizontal polarization, or s-polarization, is the component of EM radiation that oscillates out of the plane of reflection and vertical, or p-polarization, is the component of EM radiation that oscillates within the plane of reflection.

A comprehensive model for an IR sensor may have a governing equation such as the one in Equation (3.4). The functional dependence of these variables is not written in this equation but are shown in later sections when specific models are discussed, but the following variables are important for numerous models: receiver elevation θ_r and azimuth ϕ_r angles, receiver

altitude h, solar elevation θ_s and azimuth ϕ_s, IR wavelength λ, sea surface temperature T_{surf}, sea surface elevation z, and sea surface slopes $\xi_x = \partial z/\partial x$ and $\xi_y = \partial z/\partial y$ in the x and y directions, respectively. It is assumed that the models selected for the sources $R_{atmo,down}$, $R_{atmo,up}$, $R_{ss,down}$, and $R_{ss,up}$ model the effects of imperfect transmission. Two separate transmission values are yet required, τ_{sun} models the transmission loses that affects solar irradiance as it propagates from the top of the atmosphere to the surface and τ_{surf} which models transmission losses of IR radiation that propagates from the surface to the sensor.

$$R = \tau_{surf} R_{surf} + R_{atmo,up} + R_{ss,up} \tag{3.4}$$

where

$$R_{surf} = \epsilon R_{sea} + \rho \left(\tau_{sun} R_{sun} + R_{atmo,down} + R_{ss,down} \right)$$

The above equation is solved for every grid cell within the domain to generate a simulated IR image. Data output from OpenFOAM and EOM are already discretized, and these data retain the same coordinate system where $+x$ is defined in the direction opposite to the ship direction, $+z$ pointing straight up, and $+y$ completing the right-handed system. The sea surface elevation realization generated by EOM is used to generate a series of facets with varying orientation. These facets function as discrete surfaces which are used in the calculation of reflection and emissivity, and the atmosphere-pointing surface normal for each facet can be derived from the sea surface elevation data.

The model described by Equation (3.4) is comprehensive and consequently requires models for all of the parameters and IR sources listed. An assumption is now taken to reduce this equation to a simpler form, the assumption being that all atmospheric effects are negligible,

including loss due to imperfect transmissivity and atmospheric-originating IR radiation. Additionally, it is assumed that the amount of solar IR that is scattered directly towards the sensor, i.e. $R_{ss,up}$, is negligible. Numerically, this means that all τ values are equal to unity and that $R_{atmo,down}$, $R_{atmo,up}$, and $R_{ss,up}$ are equal to zero. This simplifies Equation (3.4) down to a form that only contains sea surface–emitted IR radiation and reflected solar radiation shown in Equation (3.5), which requires models for emissivity, reflectivity, ocean surface black-body radiation, direct solar radiation, and in-scattered solar radiation that reaches the ocean at the specular angle. A high-level summary for the IR sensor model is given in algorithm 1.

$$R = \epsilon R_{sea} + \rho \left(R_{sun} + R_{ss,down} \right) \tag{3.5}$$

Algorithm 1 IR sensor model algorithm.

Input: sea surface elevation z; sea surface temperature T_{surf}; sensor location and orientation θ_r, ϕ_r, and h; sun location θ_s and ϕ_s; IR wavelength λ

Discretize sea surface into facets; calculate ξ_x, ξ_y, and atmosphere-pointing surface normals.

for all sea surface facets **do**

Calculate reflectivity ρ and emissivity ϵ.

Calculate emitted black-body IR radiation from sea surface R_{sea}.

Calculate solar IR radiance R_{sun} and scattered solar IR radiance $R_{ss,down}$ and the quantity of IR radiation that is reflected by facet towards sensor.

Calculate total IR radiance R detected at sensor for the given facet.

end for

Generate image from R and save to disk.

3.2.2 Model Equations

Surface Facet Geometry

The ocean surface may be discretized into a series of flat plates or facets with different orientations depending on the local sea surface slope. This allows one to apply known analytic methods for calculating the reflection of IR waves off of this surface, and an approach based on the one derived by Wu and Smith (1997) is used here. The simulated sensor assumes that any given facet on the sea surface will reflect IR waves towards the sensor such that they may be detected. These reflected IR waves are assumed to originate from the sun, neglecting secondary reflection from neighboring facets, and so the angle of incidence required to attain this reflection is calculated using equations that will be described in this section. Similarly, the reflection computations for each facet assume that it exists alone and is not subject to interference in the form of wave shadowing from other waves on the ocean surface.

Figure 3.6 shows an example sea surface facet defined using Cartesian coordinates, where the surface has an atmosphere-pointing unit normal vector $\hat{n}$. The unit vector $\hat{r}$ points from the center of the facet towards the IR sensor and the unit vector $\hat{i}$ is the direction in which an incident EM wave would need to travel in order to reflect off of the facet along $\hat{r}$; $\hat{r}$, $\hat{i}$, and $\hat{n}$ are all co-planar and the plane that they span may not be coincide with the vector z.

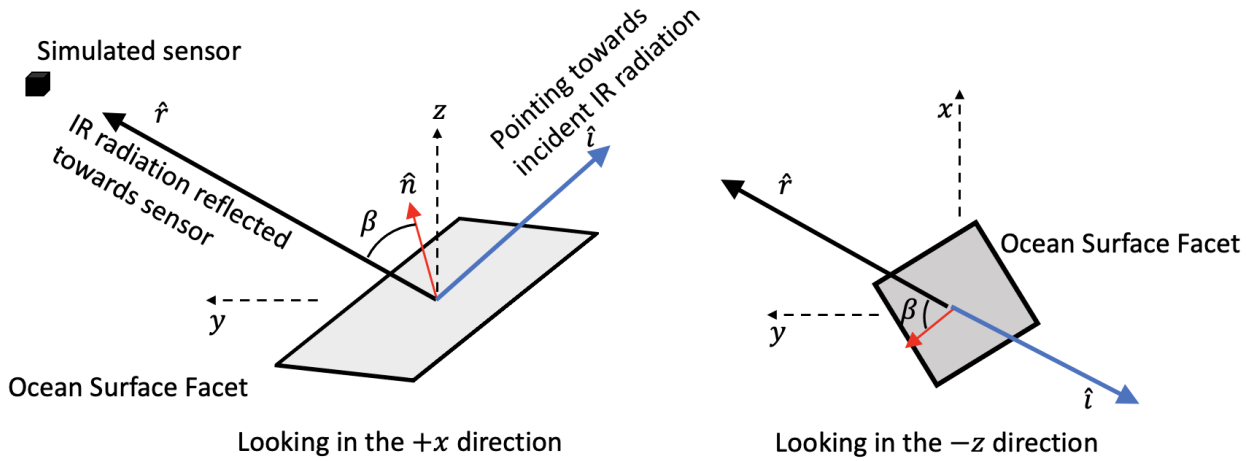

Figure 3.6: A model sea surface facet showing the important angles and vectors used in this IR sensor model as seen from two different views. Note that this facet is inclined and its normal does not align with any coordinate axis.

The following polar angles are then defined between z and the subscript vector: θ_r, θ_i, θ_n. Angle β represents the angle between $\hat{r}$ and $\hat{n}$ such that $\cos\beta = \hat{r} \cdot \hat{n}$ if $\hat{r}$ and $\hat{n}$ are defined in Cartesian coordinates. Geometric relations may be used to relate $\hat{r}$, $\hat{i}$, and $\hat{n}$ together, and since $\hat{r}$ and $\hat{n}$ are known *a priori*, $\hat{i}$ may be calculated for each sea surface facet using knowledge that the incident ray is reflected about the surface normal as recorded in Equation (3.6).

$$\hat{i} = 2\hat{n}\cos\beta - \hat{r} \tag{3.6}$$

Refractive Index of Seawater

The complex refractive index $\bar{n}$ of both air and seawater is required to calculate the value of ρ and therefore ϵ using the model discussed in the above section. This number is generally complex in value and governs how an electromagnetic wave is affected by the medium it travels in. Equation (3.7) shows how $\bar{n}$ is constructed from its components, each of which

having a physical interpretation: n is called the index of refraction and $\kappa \geq 0$ is extinction coefficient. The former is related to the phase velocity of an EM wave in a medium and the latter represents the lossiness of an EM wave as it travels through a medium.

$$\bar{n} = n - i\kappa \tag{3.7}$$

$\bar{n}$ in a vacuum for all electromagnetic waves is real and equal to unity, but this value can vary greatly by both medium and the EM wavelength or frequency. In air at 0 °C, the refractive index is negligibly different from $\bar{n}$ in a vacuum with a real value of nearly 1.0003 which is used for this work (Hecht, 2017). $\bar{n}$ for water and seawater has a complicated relationship that has been studied by many researchers. Several authors (Bertie and Lan, 1996; Downing and Williams, 1975; Hale and Querry, 1973; Pinkley et al., 1977; Rusk et al., 1971; Segelstein, 1981) present empirical estimates of $n_{pure} = n_{pure}(\lambda)$ and $\kappa_{pure} = \kappa_{pure}(\lambda)$ for pure water across a wide range of the EM spectrum including the IR spectrum, however the composition of seawater including salinity and chlorinity as well as temperature may change the values of n and κ compared to pure water. The following subsections seek to understand the impact of salinity and temperature on the refractive index of water and if possible derive correction factors $\Delta n_{S,T}$ and $\Delta\kappa_{S,T}$ for these variables in a way that a corrected refractive index can be computed as shown in Equation (3.8). For further accuracy, the combined dependence of temperature and salinity on refractive index can be incorporated into this equation but this is not pursued in this work.

$$\bar{n}_{sea}(\lambda, S, T) = (n_{pure}(\lambda) + \Delta n_S(\lambda, S) + \Delta n_T(\lambda, T)) - i\,(\kappa_{pure}(\lambda) + \Delta\kappa_S(\lambda, S) + \Delta\kappa_T(\lambda, T)) \tag{3.8}$$

Impact of Salinity

Friedman (1969) studied the complex refractive index of seawater across the 1.5–15 µm portion of the IR spectrum and compared it to documented values for pure water for the same range and found there were significant differences between the refractive indices of seawater and pure water. He tabulated these differences as functions of wavelength such that these differences are—after being modified for the salinity of the ocean—added to the refractive index for pure water $\bar{n}_{pure}$ as correction factors as shown in Equation (3.8). Friedman also studied the impact of relative salinity on refractive index and found that there was an approximately linear relationship between salinity and refractive index. Therefore, he provided a recommendation for scaling the wavelength-dependent additive corrections to n and κ by the salinity relative to a reference chlorinity of 19 ppt. Chlorinity may be directly used in this calculation if available, however chlorinity is proportional to salinity measured in practical salinity units (PSU) by a factor of 1.80655 PSU to 1 ppt chlorinity (Millero, 2016), giving a reference salinity S_{ref} of approximately 34.3 PSU.

Below are the Friedman's recommendations for correction factors Δn_S and $\Delta \kappa_S$ as a function of wavelength λ and practical salinity S which are used for the determination of $\bar{n}$ of sea water in this work:

1. $1.5 \leq \lambda < 9$ µm: $\Delta n_S(\lambda, S) = 6 \times 10^{-3} \frac{S}{S_{ref}}$, $\Delta \kappa_S(\lambda, S) = 0$;
2. $9 \leq \lambda \leq 15$ µm: $\Delta n_S(\lambda, S)$ and $\Delta \kappa_S(\lambda, S)$ are linearly interpolated from wavelength-dependent values given in a table by Friedman (1969) then multiplied by a factor $\frac{S}{S_{ref}}$.

The difference in the index of refraction and extinction coefficient across the 1.5–15 µm range is shown in Figure 3.7. Pinkley and Williams (1976) performed a similar study of the

complex refractive index of seawater and provides an estimation of $\bar{n}$ is in good agreement with Friedman's results. Root-mean-square (RMS) error of $\bar{n}$ with and without Friedman's salinity correction is calculated for both n and κ relative to Pinkley and Williams' data. RMS error of n decreases across the IR spectrum when the salinity correction is used but RMS error increases for κ with the salinity correction. Newman et al. (2005) compared the correction factors of both Friedman and Pinkley and Williams to observed data collected over the ocean and found both correction schemes were in accordance with the observations.

Impact of Temperature

While Friedman did not examine the effects of temperature, Pinkley et al. (1977) examined refractive index across a range of temperatures from 1 °C to 50 °C, and these authors show that n and κ do not exhibit radical differences in behavior across the IR spectrum between the tested temperatures although the quantitative values of n and κ vary with temperature, especially around a wavelength of 3 µm. Newman et al. (2005) also examines the effects of temperature on refractive index and found that both index of refraction and extinction coefficient tend to increase with decreasing temperature and provided a tabulated curve fit for n and κ as a linear function of temperature and non-linear function of wavelength. In equation form, the curve fits have the form

$$n(\lambda, T) = n_0(\lambda) + c_n(\lambda)(T - T_{ref})$$
$$\kappa(\lambda, T) = \kappa_0(\lambda) + c_\kappa(\lambda)(T - T_{ref})$$

where T_{ref} is zero degrees Celsius and the fluid is assumed to be ocean water. $c_n(\lambda)$ and $c_\kappa(\lambda)$ act as partial derivatives of the respective refractive index component with respect to

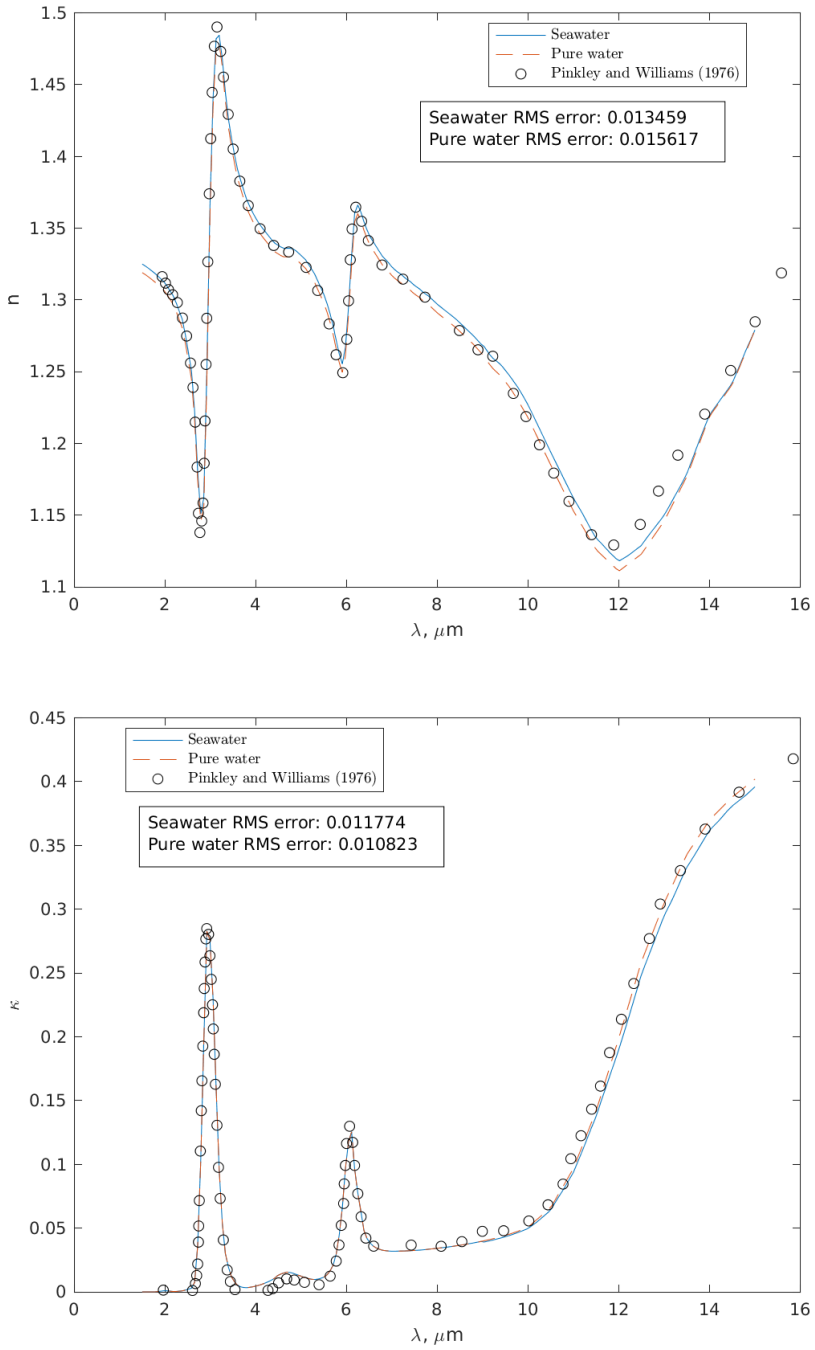

Figure 3.7: Index of refraction n (top) and extinction coefficient κ (bottom) for seawater with a salinity of 34.3 PSU (solid blue line) and pure water (dashed orange line) using Hale and Querry (1973) for pure water and the procedure of Friedman (1969) for seawater corrections. The open dots represent experimental data from Pinkley and Williams (1976).

temperature at zero degrees Celsius and $n_0 = n(\lambda, 0°)$ and $\kappa_0 = \kappa(\lambda, 0°)$. Hale and Querry's tabulated $\bar{n}$ data as well as Friedman's salinity corrections are calculated with a reference temperature of 27 °C, and since these data form the basis for the refractive index used in this work, some assumptions are needed to derive a temperature correction from the data of Newman et al. (2005).

Firstly, one may assume that any non-linear interaction between salinity and temperature on refractive index are small and may be neglected. One concrete outcome of this assumption is that we can take c_n, c_κ as constant with salinity and therefore these coefficients as provided by Newman et al. (2005) may be applied to seawater or fresh water. Secondly, it is assumed that $c_n(\lambda), c_\kappa(\lambda)$ are approximately constant across the range of temperatures seen in a typical open ocean environment such as in the Atlantic ocean far from the poles. In this case, we may adjust the reference temperature from 0 °C to 27 °C, which is the reference temperature for the Hale and Querry refractive index data, while using the same c_n and c_κ values provided by Newman et al. This means that $n_0(\lambda)$ and $\kappa_0(\lambda)$ are equal to those provided by Hale and Querry for freshwater so $\Delta n_T(\lambda, T)$ and $\Delta \kappa_T(\lambda, T)$ from Equation (3.8) become equal to

$$\Delta n_T(\lambda, T) = c_n(\lambda)(T - 27\ °C)$$
$$\Delta \kappa_T(\lambda, T) = c_\kappa(\lambda)(T - 27\ °C).$$

The above temperature correction scheme is applied to the Hale and Querry estimates for refractive index alongside Friedman's salinity corrections to provide a complete model for refractive index. $c_n(\lambda)$ and $c_\kappa(\lambda)$ are provided in a table for wavenumbers between 770 and 1230 cm^{-1} which are interpolated for any wavelength that yields a wavenumber within this

range. This range roughly corresponds to the 8–12 µm range, and outside of this range, the temperature correction terms are set to 0.

Newman et al. (2005) provides curves for n, κ as functions of wavelength and data from these curves are digitized and used to evaluate the refractive index model given by Equation (3.8). Figure 3.8 plots observed refractive index against the calculated refractive index at two different temperatures—6 °C and 27 °C—and two different salinities—0 PSU and 34.3 PSU. Root-mean-square error for these four calculated curves are displayed on the plot as well. Applying the derived temperature corrections leads to a better match with Newman et al.'s data as shown by the RMS error, which is expected as the temperature corrections originate from Newman et al. This is particularly visible in the plot for n for wavelengths between 11 and 13 microns. The extinction coefficient κ shows a lower RMS error when the salinity correction is omitted, which is also observed in Figure 3.7.

Surface Reflectivity

Reflectance ρ represents the fraction of energy that reflects off of a surface and is a function of the Fresnel power reflectivity coefficient. Reflectivity coefficients and therefore reflectance are dependent on polarization as shown in Equation (3.9), but an unpolarized reflectance may be quantified using Equation (3.10).

$$\rho_p = |r_p|^2 \tag{3.9a}$$

$$\rho_s = |r_s|^2 \tag{3.9b}$$

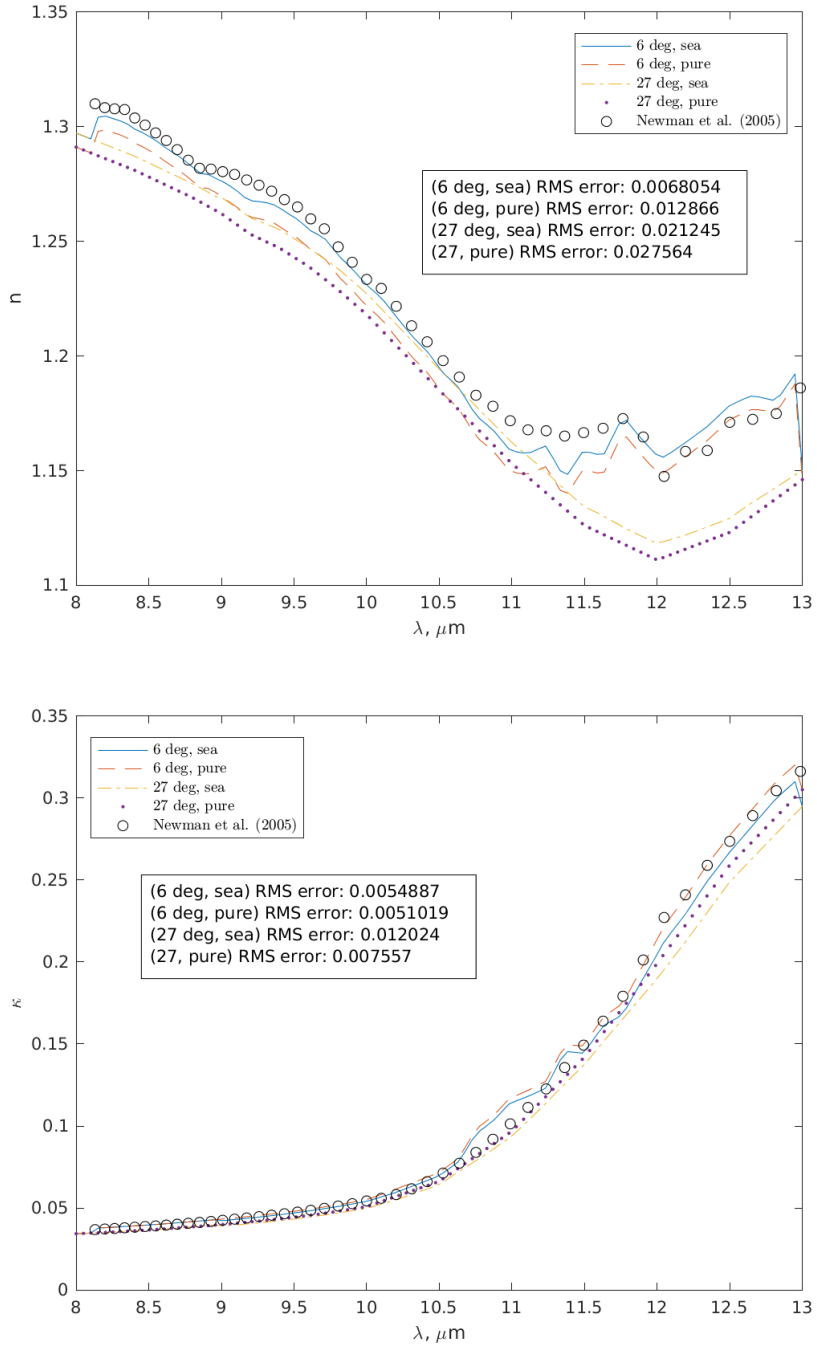

Figure 3.8: Index of refraction n (top) and extinction coefficient κ (bottom) for freshwater and seawater with a salinity of 34.3 PSU at a warm (27 °C) or cold (6 °C) temperature. These data are compared to the data from Newman et al. (2005).

$$\rho = \frac{\rho_p + \rho_s}{2} \tag{3.10}$$

The Fresnel power reflectivity coefficients r_p and r_s are related to incidence angle θ_i and the angle that the transmitted rays take within the ocean θ_t using Equations (3.11a) and (3.11b) for the p-polarized and s-polarized waves, respectively. These equations are functions of the complex indices of reflection of air n_{air} and the ocean water n_{sea}.

$$r_p = \frac{-n_{sea}\cos\theta_i + n_{air}\cos\theta_t}{n_{sea}\cos\theta_i + n_{air}\cos\theta_t} \tag{3.11a}$$

$$r_s = \frac{n_{air}\cos\theta_i - n_{sea}\cos\theta_t}{n_{air}\cos\theta_i + n_{sea}\cos\theta_t} \tag{3.11b}$$

The angles θ_i and θ_t can be related using Snell's law, given in Equation (3.12).

$$\sin\theta_t = \frac{n_{air}}{n_{sea}}\sin\theta_i \tag{3.12}$$

Combining Equation (3.12) and the identity $\cos\theta = \sqrt{1-\sin^2\theta}$ allows Equations (3.11a) and (3.11b) to be rewritten, after some manipulation, as Equations (3.13a) and (3.13b) respectively. These equations may be solved to determine reflectance, and Figure 3.9 shows how these reflectance varies for p-polarized, s-polarized, and unpolarized EM waves as incidence angle changes. The reflectance of each polarization exhibits a notable difference in their relationship, with p-polarized EM waves having a decrease in reflectance as incidence angle increases from 0° before increasing to 1 as incidence angle approaches 90°. S-polarized EM waves have a monotonic increase in reflectance as incidence angle increases and at all incidence angles plotted in Figure 3.9, ρ_s has a higher magnitude than ρ_p, meaning that

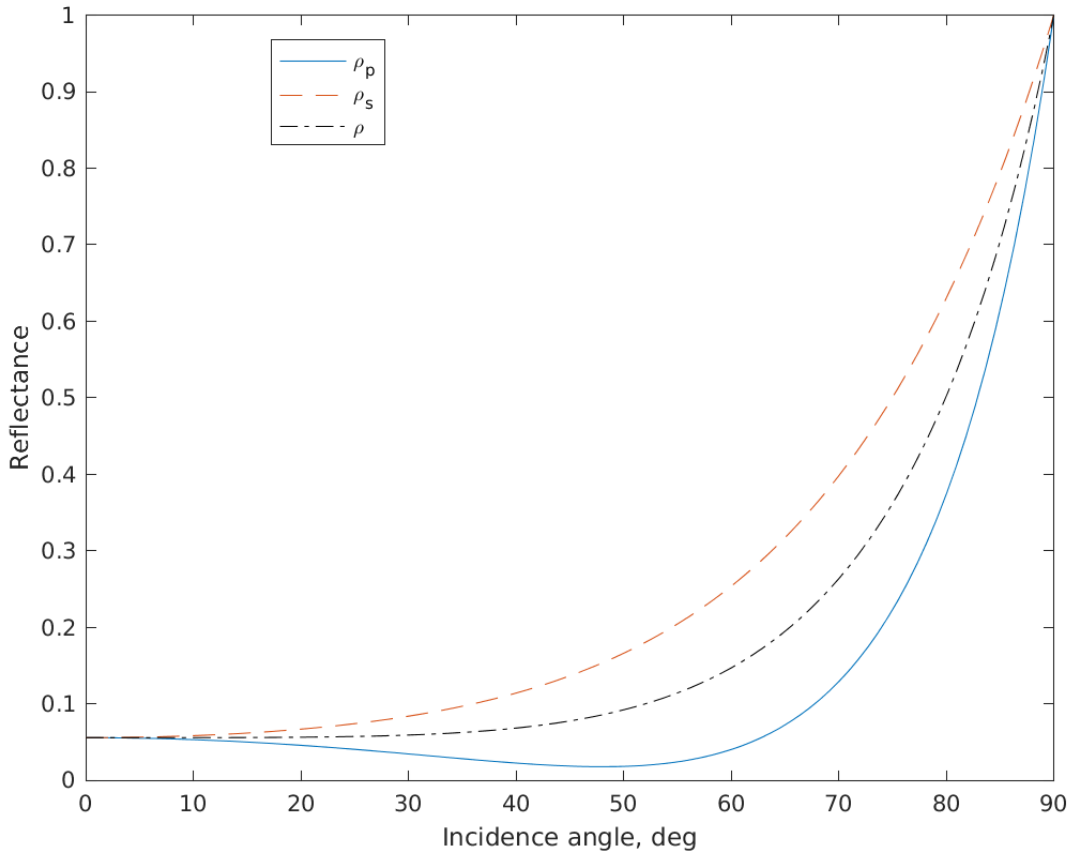

Figure 3.9: Reflectance for both polarizations and unpolarized EM waves as a function of incidence angle. Here, $\bar{n}_{sea} = 1.1 - 0.5i$ and $\bar{n}_{air} = 1 - 0i$ for demonstration purposes.

the majority of energy in EM waves reflecting off of the ocean surface will be carried in the out-of-plane polarized waves.

$$r_p = \frac{-n_{sea}^2 \cos\theta_i + n_{air}\sqrt{n_{sea}^2 - n_{air}^2 \sin^2\theta_i}}{n_{sea}^2 \cos\theta_i + n_{air}\sqrt{n_{sea}^2 - n_{air}^2 \sin^2\theta_i}} \tag{3.13a}$$

$$r_s = \frac{n_{air}\cos\theta_i - \sqrt{n_{sea}^2 - n_{air}^2 \sin^2\theta_i}}{n_{air}\cos\theta_i + \sqrt{n_{sea}^2 - n_{air}^2 \sin^2\theta_i}} \tag{3.13b}$$

Friedman (1969) performed an experimental study of reflectance of sea water across the IR

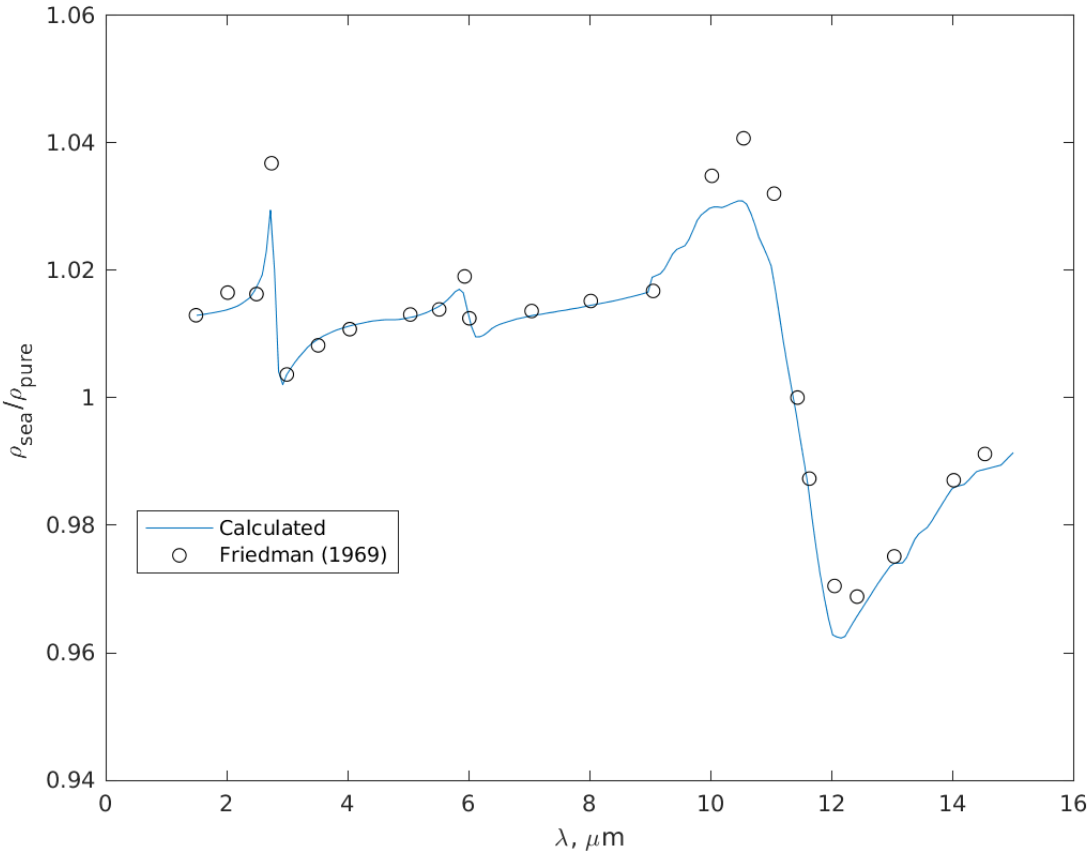

Figure 3.10: The ratio of reflectance for seawater and pure water across the IR spectrum for an incidence angle of 70° and a chlorinity of 19 ppt.

spectrum. These data are plotted in Figure 3.10 alongside values calculated from Equation (3.10) above for a reflection with an incidence angle of 70 ° and a seawater chlorinity of 19 ppt, roughly corresponding to a salinity of 34.3 PSU. The calculated values on this plot use refractive index values for pure water with seawater corrections applied as described in the above subsection. The calculated and experimental data compare well except at a few points where the reflectivity ratio changes rapidly, however this may partially be explained by the fact that Friedman derived the seawater refractive index corrections for a different set of pure water refractive index values than the ones utilized in this work.

The effects of salinity are also examined by Friedman (1969) where, as above, the ratio of seawater reflectance and pure water reflectivity are examined for a 70° incidence angle as shown in Figure 3.11. Here, this reflectance ratio of two IR wavelength—10.5 and 12.4 µm—is examined as salinity of the water is varied with a reference value of 19 ppt chlorinity is used such that a relative salinity of two refers to seawater with a chlorinity of 38 ppt. The Fresnel reflectivity equations are used with the seawater-corrected refractive index including the salinity correction described in section 3.2.2. The computed values lay near the experimental data with a maximum of approximately 2% difference relative to the experimental values. The 10.5 µm experiences a noticeable divergence from the experimental value but the calculated reflectance values for wavelengths around 10.5 µm fit the experimental data relatively poorly as shown in Figure 3.10. Given that the calculated values use a linear salinity correction, any deviation from the observed values at a relative salinity of 1 would be exacerbated by an environment with doubled salinity, although nearly the entirety of the world's oceans have a salinity of 30–40 PSU (Droghei et al., 2018) so this level of salinity would only be experienced in artificial settings. Nonetheless, the linear salinity correction that Friedman describes fares well here.

While Friedman examined reflections at high incidence angles, Pinkley and Williams (1976) examined IR reflections off of seawater at near-normal incidence angles. Figure 3.12 plots the reflectance ratio of seawater to pure water across the IR spectrum in a similar manner to the procedure shown in Figure 3.10. An incidence angle of 5° is used in the calculation, and seawater with chlorinity of 19 ppt and 38 ppt are used for the calculation. Reflectance ratio curves for these two chlorinities are compared with the corresponding curves from Pinkley and Williams. Again, the reflectance ratios calculated using the seawater correction procedure recommended by Friedman fares well compared to experimental data at small incidence angles.

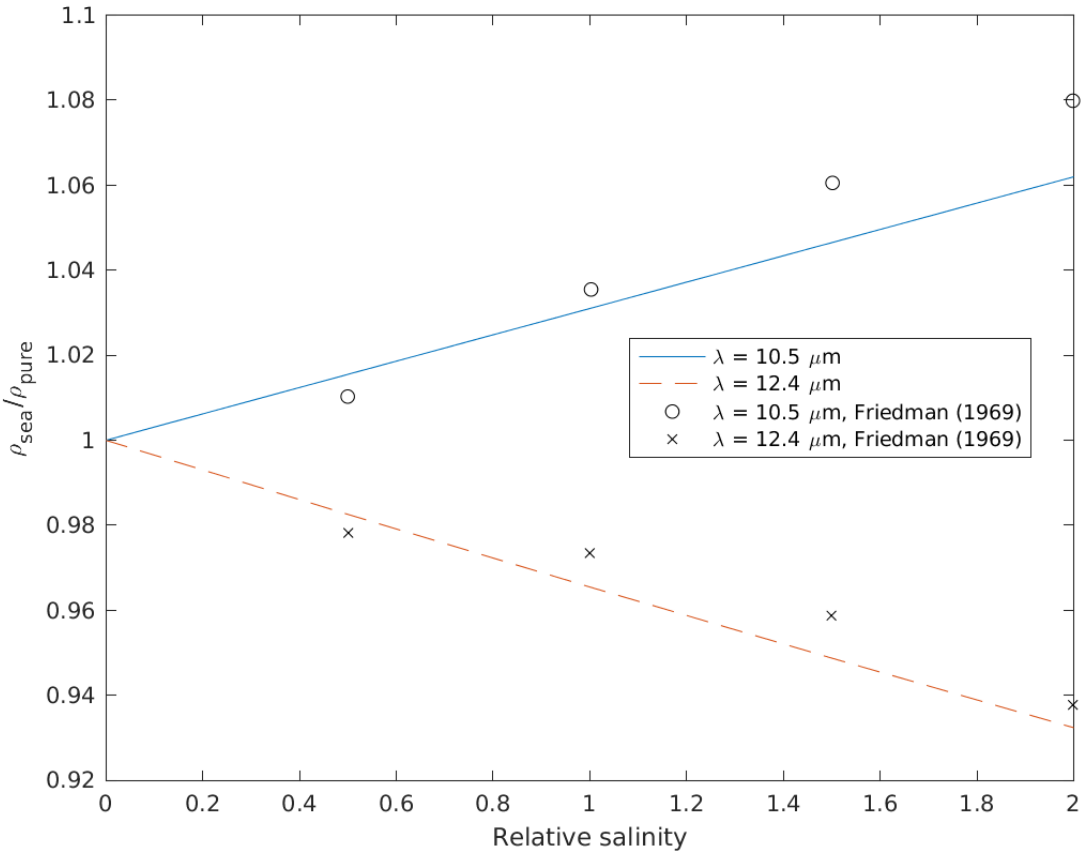

Figure 3.11: The ratio of reflectance for seawater and pure water across the IR spectrum for an incidence angle of 70° and a chlorinity of 19 ppt.

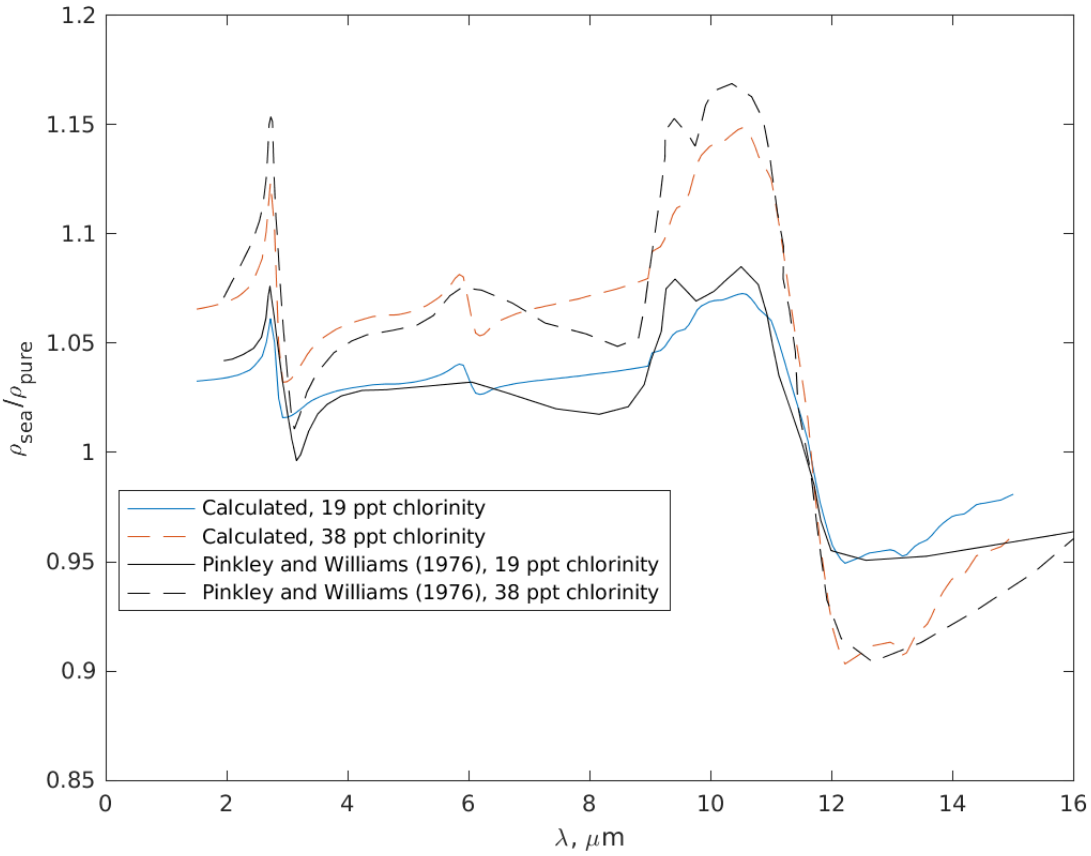

Figure 3.12: The ratio of reflectance for seawater and pure water across the IR spectrum for an incidence angle of 5° (calculated) and "near-normal incidence" (data from Pinkley and Williams (1976)) for two different seawater chlorinities.

Surface Emissivity

The problem of determining emissivity of the ocean surface facets remains. Energy carried in an electromagnetic wave of a given polarization must be conserved, so if one knows the fraction of energy transmitted into the water, this same fraction must be ultimately absorbed. Absorptivity, or the fraction of incident energy that is absorbed, for a body in thermal equilibrium is related to emissivity using Kirchhoff's law of thermal radiation, as shown in Equation (3.14) for either both polarized components of EM waves and consequently their unpolarized equivalent. As reflectance is a function of the media and incidence angle of the incoming EM waves, these values are also functions of the media and incidence angle, and Figure 3.13 shows how these values may vary with incidence angle on an air–sea interface. Emissivity is high for low incidence angles and negligible for near-grazing incidence angles which may have a significant impact on the detectability of a hot or cold patch of water on the ocean surface.

$$\epsilon_p = 1 - \rho_p \tag{3.14a}$$

$$\epsilon_s = 1 - \rho_s \tag{3.14b}$$

$$\epsilon = 1 - \rho = \frac{\epsilon_p + \epsilon_s}{2} \tag{3.14c}$$

The experiments conducted by Friedman (1969) and Pinkley and Williams (1976) help understand the performance of the refractive index and reflectance model used in this work in a controlled environment but real-world data are still needed to compare the performance of the reflectance and equivalently emissivity model to a real ocean environment. Saunders (1968) examined sky and ocean surface radiance and as part of the study also

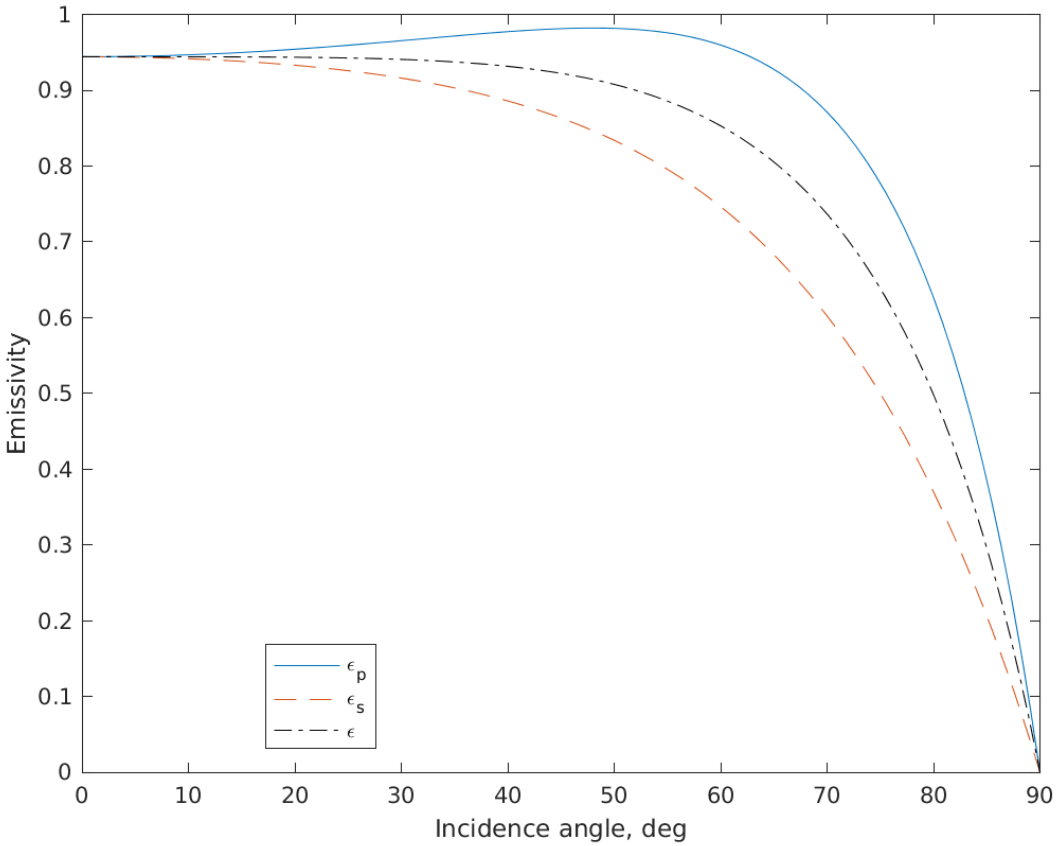

Figure 3.13: Emissivity for both polarizations and unpolarized EM waves as a function of incidence angle. $\bar{n}_{sea}$ and $\bar{n}_{air}$ are the same as in Figure 3.9

.

recorded reflectance values for the 8.35–12.2 µm range. These values were averaged across the wavelength range and weighted by sensor sensitivity, and here these measurements are compared against several other estimations in Figure 3.14. Equation (3.10) is evaluated for IR wavelengths—8.4 µm, 10 µm, and 12 µm—using complex index of refraction values from Hale and Querry with Friedman's correction applied for the latter two wavelengths. Wilson (1979) provides an empirical model for sea surface emissivity as a function of incidence angle that is compared with the data from Saunders and the three analytic emissivity curves. Wilson's emissivity model is given in Equation (3.15).

$$\epsilon_{Wilson} = 0.98\left(1 - [1 - \cos\theta_i]^5\right) \tag{3.15}$$

The reflectance curves calculated from the Fresnel equations match Saunders' data closer than Wilson's model particularly at large incidence angles. Saunders' data is the result of weighted averaging across the 8.35–12.2 µm range with the weightings provided by the sensor system and not included in the report, however the three analytic reflectance curves nearly cover the wavelength range examined by Saunders and bracket the experimental data well. This shows that Equations (3.13a), (3.13b), and (3.14) provide a good model for emissivity of long-wave IR.

3.2.3 Modeling IR Sources

All infrared radiation in this model originally radiates from a body, whether that body is the sun, the atmosphere, the sea surface, or any object within the sky. The atmosphere and sea surface will also interact with any radiation that propagates within in or otherwise interacts with it. Solar radiation travels through space and reaches the earth's atmosphere where it is refracted and transmitted through the atmosphere until it reaches the planetary

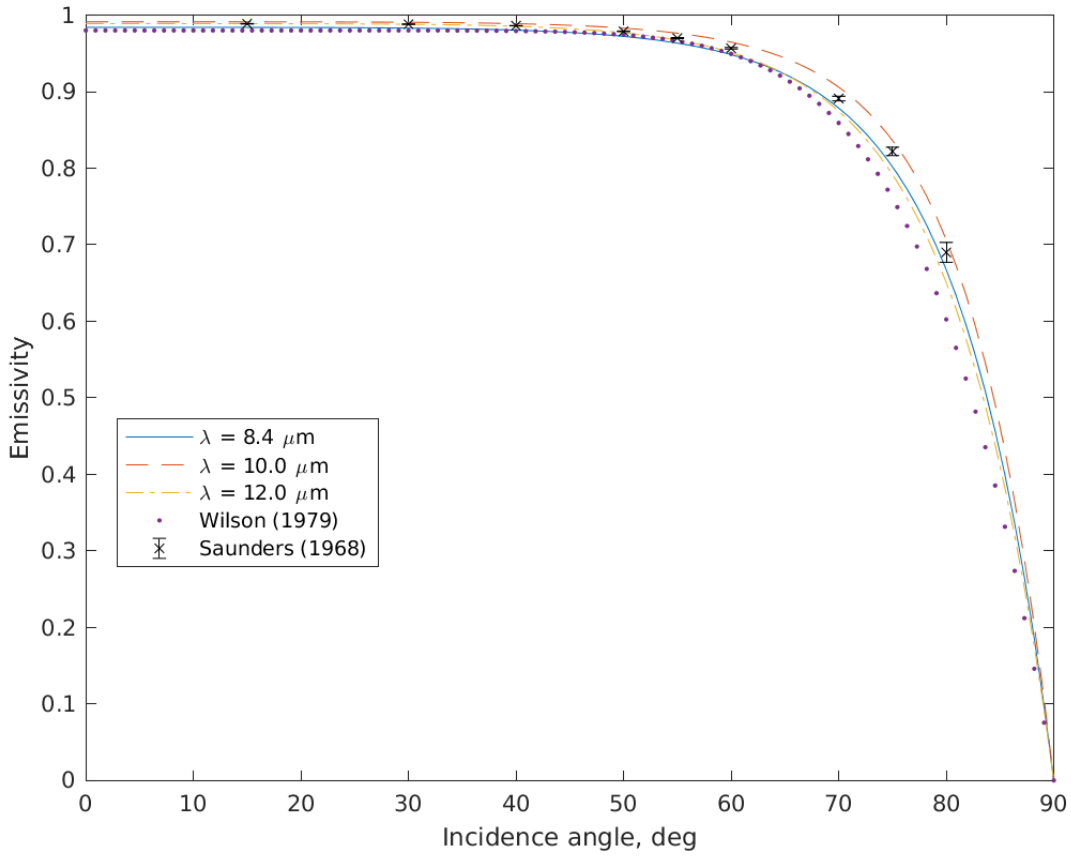

Figure 3.14: Comparison of emissivity calculated from Fresnel equations and Wilson's emissivity curve fit in Equation (3.15) with experimental data from Saunders (1968).

surface. These waves are scattered and attenuated by the atmosphere, with some wavelengths being affected more than others—cf. UV waves and visible light—but otherwise these waves may reach the earth's surface where they are reflected at the specular angle of the local surface directly towards a simulated IR sensor. These effects must be modeled using governing equations or otherwise accounted for a realistic IR sensor model. Several authors have provided comprehensive IR models which account for various IR sources and phenomenologies (Levesque and St-Germain, 1990; Mermelstein et al., 1994), and the section that follows describes the models used for IR image generation in this work.

Wein's displacement law states that the wavelength that corresponds to the peak emission of a black body is inversely proportional to its temperature in Kelvin with the constant of proportionality being around 2898 $\mu m \cdot K$ (Hecht, 2017). For temperatures near 300 K, this wavelength is around 10 µm which is well within the IR regime in the electromagnetic spectrum, however a surface with a temperature of 5800 K, which is comparable to the surface temperature of the sun, has peak EM emissions at a wavelength of 500 nm which is classified as visible light. The spectral radiance L_λ of a body with an emission ϵ may be quantified as a function of wavelength λ and temperature T using Planck's radiation law, shown in Equation (3.16) in units of $W/(sr \cdot m^3)$ where c is the speed of light in air, h is the Planck constant, and k_B is Boltzmann's constant (Hecht, 2017). Spectral radiance can be interpreted as as power per unit area, per unit length, per unit solid angle. Integrating spectral radiance over a wavelength window $\Delta\lambda$ as shown in Equation (3.17) converts this quantity to radiance L which have units of power per unit area, per unit solid angle. Figure 3.15 shows how radiance modeled by Equation (3.17) varies between a black-body at 293 K and a black-body at 5800 K where the wavelength window is $\Delta\lambda = 1$ µm wide.

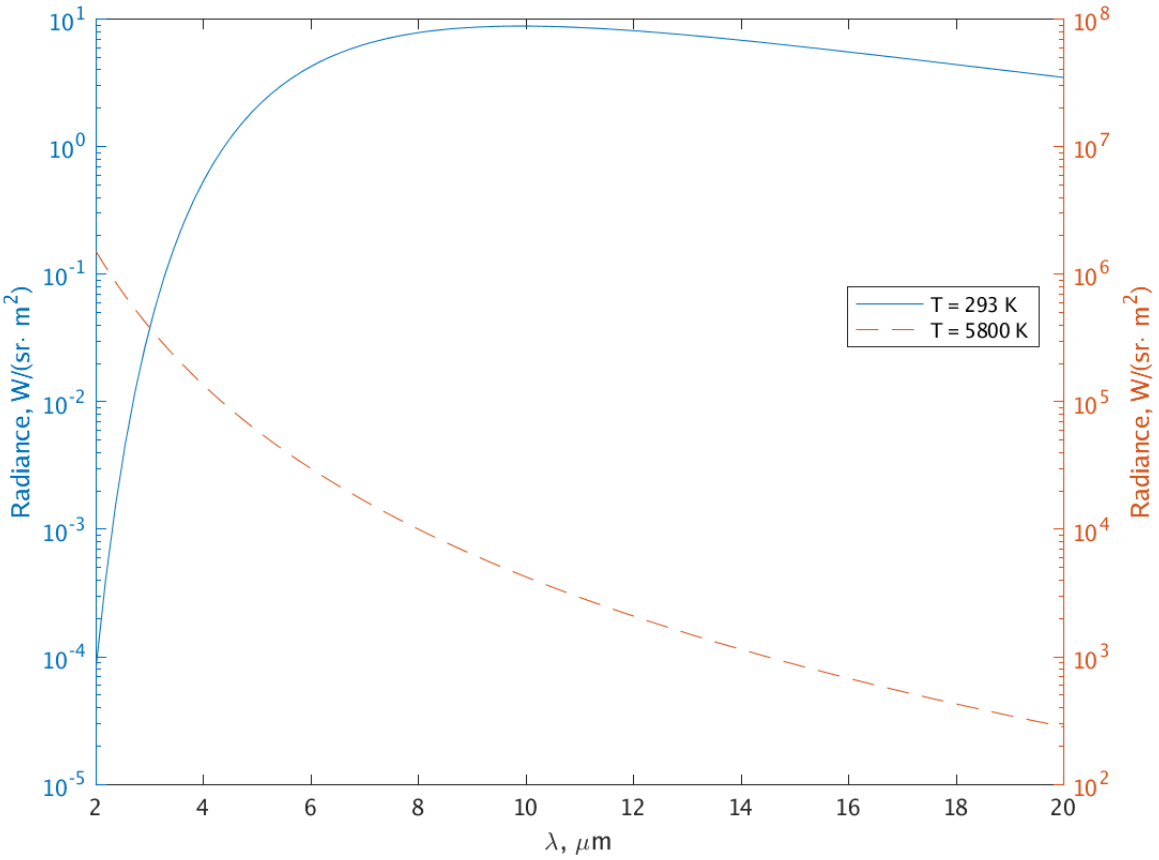

Figure 3.15: Emitted radiance by a black-body across part of the IR spectrum. The left axis represents the radiance of the $T = 293$ K case (blue solid line) and the right axis represents the radiance of the $T = 5800$ K case (orange dashed line). Note that the vertical axes are not equal in magnitude.

$$L_\lambda(\lambda, T) = \frac{2\epsilon hc^2}{\lambda^5} \frac{1}{\exp\left(\frac{hc}{k_B \lambda T}\right) - 1} \tag{3.16}$$

$$L(\lambda, \Delta\lambda, T) = \int_{\lambda - 0.5\Delta\lambda}^{\lambda + 0.5\Delta\lambda} L_\lambda d\lambda \approx L_\lambda \Delta\lambda \tag{3.17}$$

In most cases, T is the physical temperature of the body which may be measured in-situ

by a thermometer, but T may also represent a brightness temperature. Given an observed radiance L or spectral radiance L_λ, Equation (3.16) or Equation (3.17), respectively, may be used to solve for the brightness temperature emitted by a real body. This represents an effective temperature which may not be equal to the in-situ temperature of the body. For example, an IR sensor positioned on the ground and aimed at the sky will detect a quantity of radiation. This radiation is not only emitted by the atmosphere in the sensor's field of view but also radiation that is scattered towards the sensor. A parcel of air 10 m in front of the camera will emit radiation towards the sensor as will a parcel of air 100 m away from the sensor that is co-linear with the sensor and the first parcel of air. These two parcels of air may be at different temperatures, but both contribute to the radiation arriving at the sensor along the same ray, and therefore if the brightness temperature of the sky in the direction of these two parcels is calculated, the brightness temperature may not equal either of the temperature of these two parcels of air.

Scattering is the result of the interaction of EM waves with particles. It may be divided into different phenomena including Rayleigh and Mie scattering. The former occurs when EM waves are scattered by particles much smaller than the waves' wavelength, such as oxygen and nitrogen molecules, and is proportional to λ^{-4} while the latter form of scattering occurs when EM waves pass through a medium with particles much larger than the wavelength such as dust or water droplets in clouds. Unlike Rayleigh scattering, Mie scattering is roughly independent of wavelength (Hecht, 2017). An example of each of these two forms of scattering is blue-colored sky caused by Rayleigh scattering during the day and white clouds whose color is caused by the uniform scattering of light caused by Mie scattering.

Surface IR Radiation

All objects with temperature above absolute zero will radiate thermal energy and as such the sea is a source of radiation that must be quantified for the IR sensor model. This is particularly of interest in the case where a ship introduces a temperature wake, such as by mixing or entraining cold sub-surface water or expelling wastewater that has a different temperature from the surrounding fluid. The surface is modeled as a black body which uses Equation (3.17) and surface emissivity is calculated using Equation (3.14c).

Solar IR Radiation

Solar IR radiation is quantified using a model adapted from Levesque and St-Germain (1990) which assumes that the sun has an emission profile equivalent to a black body at a given temperature T_{sun}. These solar rays are emitted by the sun in all directions and some arrive at the earth traveling roughly parallel to each other. These rays encounter the atmosphere through which they are transmitted and scattered. The atmosphere is assumed to be perfectly transmissive, and the solar IR radiation model is given by

$$L_{sun}(\lambda, \Delta\lambda, T_{sun}, \Delta\theta_s) = \left(\frac{r_{sun}}{D_{sun}}\right)^2 L(\lambda, \Delta\lambda, T_{sun})\phi(\Delta\theta_s) \tag{3.18}$$

where $\Delta\theta_s$ is the angle between the ray incident upon the ocean surface and the ray directed from the facet to the sun. r_{sun} and D_{sun} are the radius of the sun and distance between the sun and earth, respectively, and the square of this ratio is proportional to the solid angle subtended by the sun as observed by a person on the earth's surface. $\phi(\Delta\theta_s)$ is the Henyey–Greenstein function (Henyey and Greenstein, 1941) given by Equation (3.19) which models the scattering of electromagnetic radiation using a constant G to control the shape of the

scattering—$G \to 1$ leads to a sharp peak for small angles that rapidly trends towards 0 for larger angles while $G = 0$ results in uniform scattering in all directions.

$$\phi(\Delta\theta_s) = \frac{1}{4\pi} \frac{1 - G^2}{(1 + G^2 - 2G\cos(\Delta\theta_s))^{3/2}} \tag{3.19}$$

Sky IR Radiation

As with solar IR radiation, the approach that Levesque and St-Germain (1990) used to simulate sky-generated IR radiation is used here: the atmosphere is represented as a blackbody with a prescribed brightness temperature that takes the form given in Equation (3.20). This profile is an interpolation between the brightness temperature at zenith and the brightness temperature measured from the horizon. Levesque and St-Germain (1990) chose this profile in a way that half the difference between the zenith and horizon brightness temperature occurs at around 15° above the horizon.

$$T_{sky}(\gamma) = T_{zenith} + (T_{horizon} - T_{zenith}) \left(\frac{2\gamma}{\pi}\right)^{5/2} \tag{3.20}$$

Levesque and St-Germain (1990) state that they use a zenith brightness temperature that is 50–60 K lower than the horizon brightness temperature, and this is within the vicinity of brightness temperatures experimentally observed or derived from standard atmosphere models per Grimming et al. (2021). A more fine-tuned brightness temperature profile may be prescribed based on the time of year, time of day, and location of the simulated domain.

This approach is compared to observed IR radiation data from Saunders (1968) who created a curve fitting for radiation according to the following form

$$N = A - B \exp -C(z-1) \tag{3.21}$$

where

$$z = (4.9 \times 10^5 \cos^2 \theta_i + 1401)^{0.5} - 700 \cos \theta_i$$

and A, B, and C are values that Saunders gives for different days throughout the year. For this comparison, the following values of A, B, and C were selected: 3540 µWcm^{-2}sr^{-1}, 2570 µWcm^{-2}sr^{-1}, and 0.285, respectively. Saunders' curve fit and the Planck radiation approach are compared over a 90° zenith angle range in Figure 3.16 where the horizon has a brightness temperature of 20 °C and the zenith has a brightness temperature of -40 °C and radiance is integrated over the 8.5–12.5 µm range. The Planck radiation model aligns with the observed data well for much of the angle range except for angles near the horizon which corresponds to data near 90°. The data presented by Saunders has much day-to-day variation so this model serves as an adequate starting point for future development.

3.2.4 Model Limitation

The following points summarize the limitations of the derived IR model which may be addressed in future work.

1. Neglects atmospheric transmissivity and upwelling atmospheric emission
2. Neglects upwelling in-scattered solar radiation
3. Neglects the effects of small waves, i.e. those lost by the discretization of the surface into facets
4. Neglects diffuse reflection (scattering) on the ocean surface

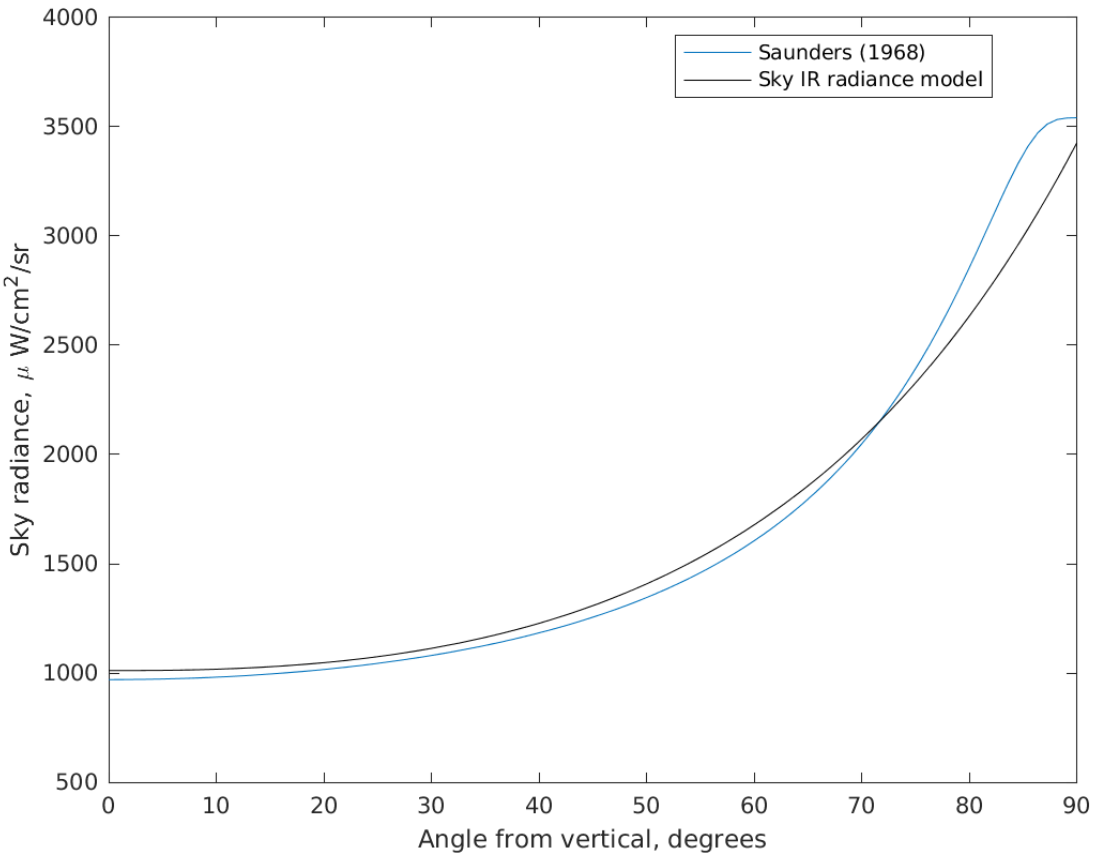

Figure 3.16: IR radiance as calculated by Equation (3.17) compared to data from Saunders (1968).

5. Neglects the effects of breaking surface waves, seafoam, and any other surfactant (Branch et al., 2016; Cheng et al., 2017)

6. Refractive index does not take into account ocean composition apart from linear temperature and chlorinity (salinity) corrections

7. Neglects secondary reflections from sea surface facet to sea surface facet

8. Neglects sea surface absorption and transmission

9. Assumes clear sky

10. Assumes polarized components of the incoming solar radiation are equal in magnitude for all wavelengths

11. Solar model assumes solar radiation is equally distributed across wavelengths

3.2.5 Example Simulation Results

Figure 3.17 shows an example of a simulated IR image of a ship wake upon the ocean surface. In this case, the ship's propellers mix water at the surface causing cool water to be introduced into the surface of the ocean. This cold water creates a dark patch on the surface which may be observed compared to the background which remains at a constant temperature. The random nature of the sea surface reflects different amounts of IR radiation towards the simulated sensor, created a noise background in spite of a nearly-isothermal surface temperature outside of the ship wake.

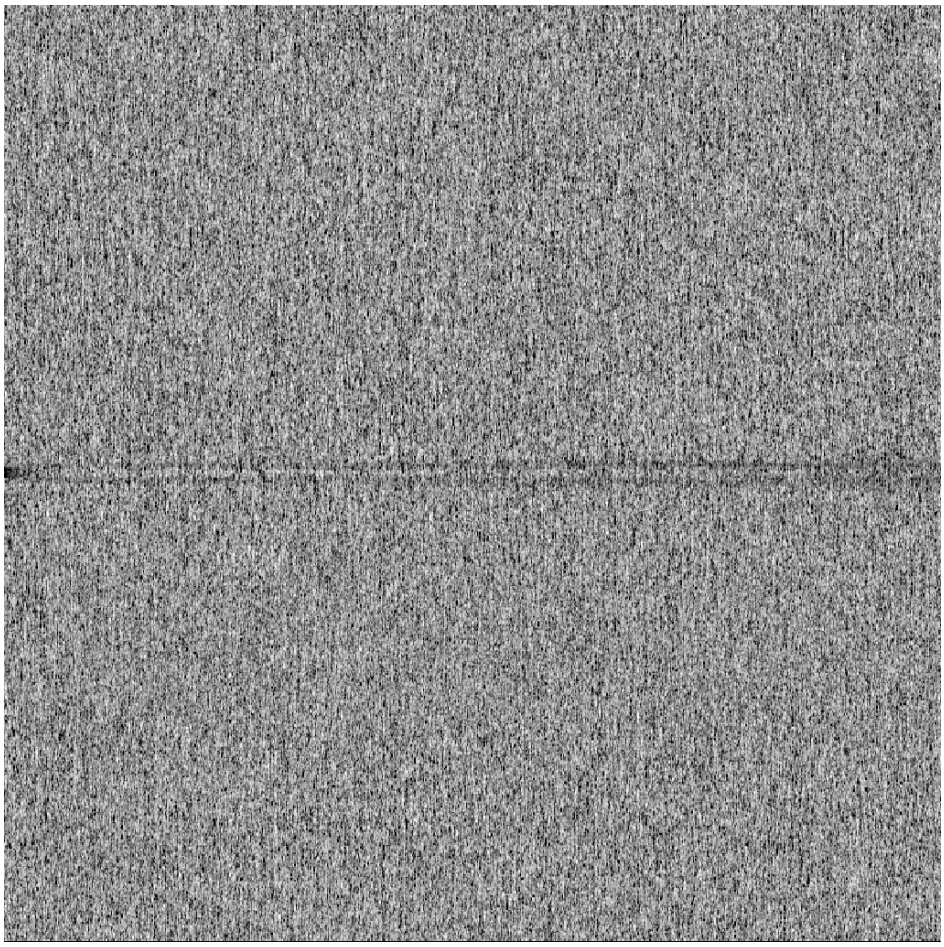

Figure 3.17: An example of a simulated 11 micron IR image of a ship wake generated using this model.

Chapter 4

Machine Learning of Remote Sensing Data

The ultimate goal of this dissertation is to develop, train, and test machine learning–based models whose goal is to detect the presence of a ship wake in remote sensing data. Studies such as this may play a role in an automated ship detection network which may aid other forms of ship detection besides, for example, detection of the ship body itself through direct observation. The use of machine learning also has the advantage of being able to consider very large sets of data beyond what humans would be able to analyze as well as be able to identify complex patterns that can be used to identify the presence of ship wakes as well as discern any additional information from the ship wake. This includes potential uses in the estimation of ship size, trajectory, and speed. While the development and testing of these more advanced analysis tools are beyond the scope of this work, this simple goal of detection a ship wake in the context of a binary classification problem is the first step in a longer series of automated classification work.

Deployment of an automated ship wake detection system requires that the detection models be trained on high quality real-world data, or data that otherwise have enough verisimilitude that the model will be able to perform adequately when real-world data is given as an input. Models that utilize machine learning learn from their training data and so these models need to be exposed to a large quantity of data covering a broad range of scenarios in order

to provide a useful and robust model, so obtaining a data set large enough and diverse enough for a given application of a wake detection system may be challenging. The data must be curated such that they are in a standardized format, and the data must also have a corresponding set of ground truth labels that serve as the known status of the presence of a wake in an input. There are also considerations for the quality of the training data with respect to expected data collected during deployment, particularly for the peculiarities of the sensor system. Any flaws in collected that may be observed during run time, such as noise in the collected data or lost data due to sensor failure, may also need to be considered as such instances may be observed during real-world operation of a wake detection system. For example, in the event that segments of a SAR image are lost due to communication failure or some other incident, knowledge of the robustness of the detection model may allow the operator to make a decision whether the collected data can be used as an input or if replacement data must be collected.

Finding data sets which fit these criteria while still being relevant to the intended deployment use case may be difficult. Different sensor systems may have difference performance characteristics and different output data formats that make trying to create a universal model useless. The question then becomes a matter of which data should the models pursued in this thesis be trained on. Rather than collecting real-world data for training and evaluation, this work leverages the physics-based modeling and simulation means described in preceding chapters to generate a set of simulated remote sensing data of ship wakes. This has several advantages since the data can be generated in a uniform format and in as large of a quantity as desired. All of the details of the simulations are known *a priori* so ground truth labels can be provided during the data generation stage, and parameters can be controlled for unlike in real-world data. This provides a means of parameter studies for determining model robustness or uncertainty quantification that may be difficult or impossible using real-world

data.

Simulated training and testing data do have drawbacks. Any phenomena not modeled or resolved during the physics simulations will not be included in the training and testing data which may hamper the performance of the trained models if they are deployed onto real-world systems. This may be a significant barrier to the use of simulated data as training data for wake detection models, and good performance when trained and tested on simulated data may provide a false sense of confidence regarding the expected performance of a model when deployed into a real-world environment. This may require that simulation models be tuned to provide data that better reflect a particular use case, and many large-scale simulations may incur a large computational resource cost. It may be possible that in spite of perfectly realistic data, simulated data may be useful in the augmentation of a training data set comprised of real-world data.

Real-world data must also be collected to cover all expected use cases and environments that the system may be deployed to which may be a costly venture. The inclusion of simulated data as a means to cover missing scenarios or use cases is something that may also be considered by users. As an illustration, take a case where real-world remote sensing data of a ship wake for a ship traveling in a straight line in head seas is collected as well as for the ship wake of a ship making a turn in calm seas. In order to develop a model that may have to identify the wakes of ships that have made a turn in head seas, model developers may not have access to such real-world training data. If the model is able to learn the patterns and features of head seas and a turn separately from the real-world data, then simulated data may be able to provide a case where some features of head seas travel and a maneuver are present and help the model understand what it might see in these cases.

The simulated remote sensing image data provide a structured form of data where the data exist in the form of a 2D or 3D matrix where each layer is a channel. The SAR and IR

sensors both have only a single channel but if a camera were to be added, this may require the use of data with multiple layers to represent each color channel. Given the structured nature of the data, it was decided that the wake detection models be based on convolutional neural networks (CNNs). CNNs have been well-studied for their ability to process images and form the basis for many object detection models including YOLO (You Only Look Once) (Redmon et al., 2016) and SSD (Single Shot Detection) (Liu et al., 2016), as well as feature extraction networks such as feature pyramid networks (Lin et al., 2017). Networks like these have been utilized in remote sensing applications such as object detection and classification (Ding et al., 2023; Muhammad et al., 2018).

Convolutional neural networks operate by convolving a filter across a matrix of input data. This filter is an $H_{filter} \times W_{filter} \times N_{features}$ matrix of weights that maps the input data to a new matrix called a feature map. This layer has depth of $N_{features}$, each layer of which is attributed to an abstract feature and its spatial occurrence. These features represent combinations of pixels or data that are learned as a result of the training process, and therefore these features or shapes may not have a physical interpretation. Convolutional layers may be placed sequentially one after the other, and one may interpret this as detecting combinations of features. This has the effect of looking at data on multiple scales, first on the pixel-level then at higher and higher abstractions of the input data.

4.1 Classifier Model Architecture

The convolutional neural networks in this study are created in Python using PyTorch (Paszke et al., 2019) which is shown schematically in Figure 4.1 with its layers described using Pytorch syntax in Table 4.1. A grayscale, 1024 pixel by 1024 pixel SAR image is used as the input, and pixels in the input are normalized so that their values throughout the image follow a normal

distribution. Three sequential convolutional layers are used to first extract features from the input image or image set. Batch normalization is performed following each convolution, as well as a rectified linear unit (ReLU) activation function, followed by a max pool operation. A reshaping operation flattens the final convolutional feature map into a 1D vector. This vector of features is then used as an input to a series of two fully connected neural network layers. A final fully connected layer reduces the output to a single real number which is bounded between 0 and 1 using a sigmoid activation function. This numerical output o_i is then mapped to a classification c_i through the use of a simple threshold: if o_i is greater than the threshold, then the classification $c_i = 1$, otherwise $c_i = 0$. A threshold value of 0.6 is used for the work in this paper. In this model, $c_i = 0$ corresponds to a "wake is not present in input" classification while $c_i = 1$ corresponds to a "wake is present in input" classification.

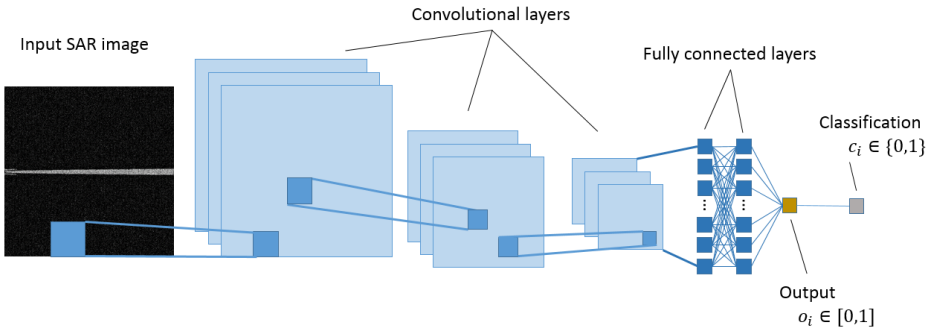

Figure 4.1: Schematic of the neural network classifier used in this study.

Table 4.1: Description of the layers in the CNN-based classifier used in this study using Pytorch syntax. The inputs are listed in order where the raw SAR data is input into the layer described in the first row and the output of the layer described by the last row is the output. All parameters not listed use the default values. The variable `inChannels` refers to the number of input channels which is equal to 1 for a single-band classifier.

Layer
`Conv2d(in_channels=inChannels, out_channels=10, kernel_size=3)`
`BatchNorm2d(num_features=10)`
`ReLU(inplace=True)`
`nn.MaxPool2d(kernel_size=2)`
`Conv2d(in_channels=10, out_channels=20, kernel_size=3)`
`BatchNorm2d(num_features=20)`
`ReLU(inplace=True)`
`nn.MaxPool2d(kernel_size=2)`
`Conv2d(in_channels=20, out_channels=30, kernel_size=3)`
`BatchNorm2d(num_features=30)`
`ReLU(inplace=True)`
`nn.MaxPool2d(kernel_size=2)`
Reshape feature maps into a 1D data vector
`Linear(in_features=47628, out_features=70)`
`Linear(in_features=70, out_features=30)`
`Linear(in_features=30, out_features=1)`

The aforementioned neural network, termed the "base" network architecture contains only 1 input channel and serves as a basis for comparison for two more architectures. The second one, called "clss," is extremely similar to "base" except that it has 2 input channels both of which being set to the input SAR image. The third is called "unet" and like "clss" has two

input channels but this time the second input channel is the output from a trained U-net which is given the input SAR data as its own input. The purpose of "clss" is to provide a control against merely changing the size of the input and this is done by providing the network redundant data so the size of the input is the same as that of the "unet" model but the model as a whole is provided the same amount of unique data as the "base" model would be receiving.

4.1.1 U-Net

U-nets are a form of CNN developed first by Ronneberger et al. (2015) for use in segmentation of medical imagery, but remote sensing applications are demonstrated by Xia et al. (2021). The U-net used in this study is adapted from Usuyama (2020) and is is shown schematically in Figure 4.2 and in Pytorch syntax in Table 4.2. For conciseness, the description of the custom `DoubleConv2d` objects are described in Table 4.3. Concatenation is performed by appending the feature maps at one point with the feature maps of a previous point in the network, effectively doubling the size of the feature map tensor. Note that the U-net does not have a sigmoid layer built into it so the output is not necessarily bound between 0 and 1 upon its calculation.

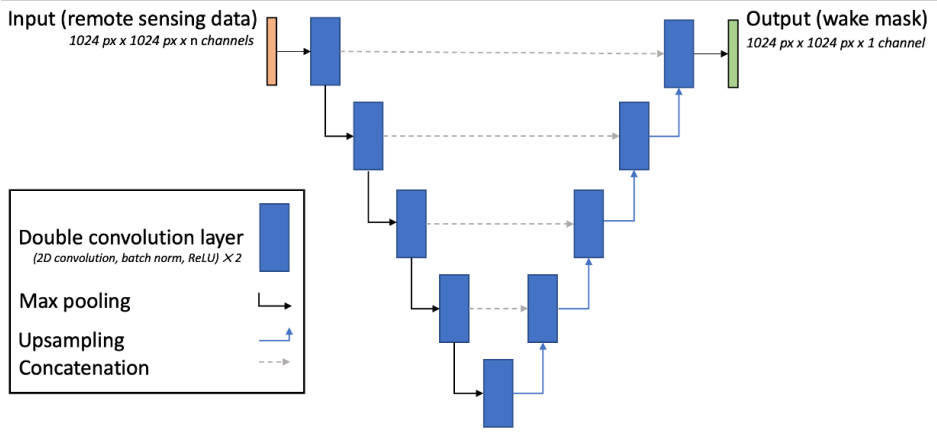

Figure 4.2: Schematic of the U-net neural network used in this study.

Table 4.2: Description of the layers in the U-net used in this study using Pytorch syntax. The inputs are listed in order where the raw SAR data is input into the layer described in the first row and the output of the layer described by the last row is the network output. All parameters not listed use the default values. `DoubleConv2d` objects are described in Table 4.3.

Layer
`DoubleConv2d(in_channels=inChannels, out_channels=64)` (Layer 0)
`nn.MaxPool2d(kernel_size=2)`
`DoubleConv2d(in_channels=64, out_channels=128)` (Layer 1)
`nn.MaxPool2d(kernel_size=2)`
`DoubleConv2d(in_channels=128, out_channels=256)` (Layer 2)
`nn.MaxPool2d(kernel_size=2)`
`DoubleConv2d(in_channels=256, out_channels=512)`
`nn.Upsample(scale_factor=2, mode='bilinear', align_corners=True)`
Concatenate feature maps with output of Layer 2
`DoubleConv2d(in_channels=768, out_channels=256)`
`nn.Upsample(scale_factor=2, mode='bilinear', align_corners=True)`
Concatenate feature maps with output of Layer 1
`DoubleConv2d(in_channels=384, out_channels=128)`
`nn.Upsample(scale_factor=2, mode='bilinear', align_corners=True)`
Concatenate feature maps with output of Layer 0
`DoubleConv2d(in_channels=192, out_channels=64)`
`Conv2d(in_channels=64, out_channels=1, kernel_size=1)`

Table 4.3: Double convolutional layer for the U-net that takes integer inputs `inChannels` and `outChannels`.

Layer
`Conv2d(in_channels=inChannels, out_channels=outChannels,`
`    kernel_size=3, padding=1)`
`ReLU(inplace=True)`
`Conv2d(in_channels=outChannels, out_channels=outChannels,`
`    kernel_size=3, padding=1)`
`ReLU(inplace=True)`

Training and Experiment

Classifier training is conducted once the SAR data set has been constructed as outlined by Figure 4.3. The data set is broken into a split of training and testing data. Data across these two subsets are distributed so that each subset has a nearly 50/50 split of wake-present and wake-not-present data which are randomly sampled from the full data set. The networks are trained for 60 epochs using stochastic gradient descent for backpropagating loss, which is calculated using binary cross entropy. The classifiers are trained with a learn rate of 10^{-3} is used with an L_2 weight penalty of 0.1. Input images are randomly rotated in 90° increments to improve robustness and prevent overfitting.

The U-net is trained using a linear combination of binary cross entropy and Sorensen–Dice loss for its training. The U-net outputs a tensor of values between 0 and 1 with values close to 1 being interpreted as being pixels that likely contain a ship wake and values close to 0 indicate that the corresponding pixel likely does not contain a ship wake. The ground truth wake masks used in training and evaluation are created by human curators who look at the

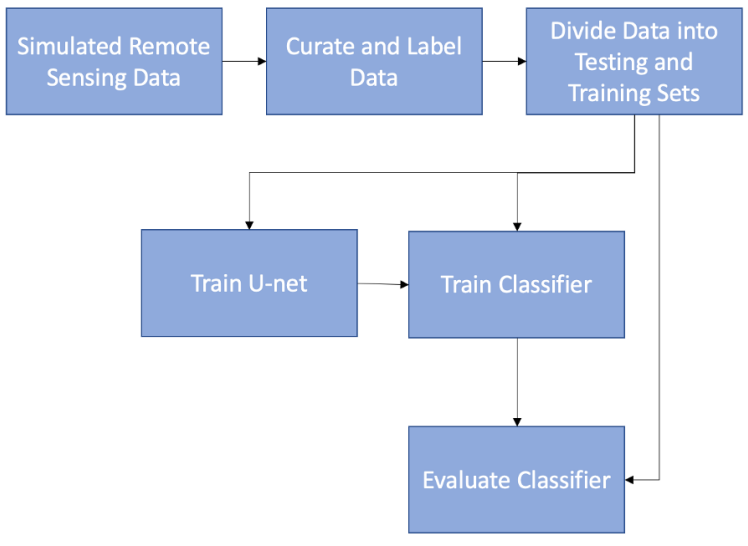

Figure 4.3: The curation, training, and evaluation process for this work.

wake images for a simulation case and attempt to determine the spatial extent of the wake for that simulation case, coloring the areas that contain the ship wake with white (a value of 1) and the areas without a wake as black (values of 0). Both the U-net output and the ground truth wake mask are used for the calculation of both loss functions. The Pytorch function `BCEWithLogitsLoss` is used to calculate the binary cross entropy loss which for a single pixel is calculated as in Equation (4.1), where y is the ground truth value (either 0 or 1), x is the output of the U-net, and σ is the sigmoid function, then averaged across the entire output. The U-net network is trained using the Adam algorithm in Pytorch with a learn rate of 10^{-4} and an L2 weight decay penalty of 10^{-4}. As with the classifier, the U-net is trained over 60 epochs and its input is likewise rotated at random 90° increments to prevent overfitting.

$$BCE = y \log\left(\sigma(x)\right) + (1 - y) \log\left(1 - \sigma(x)\right) \tag{4.1}$$

Sorensen–Dice loss is related to the intersection-over-union of the ground truth and U-net

outputs and is calculated by Equation (4.2) for each pixel. The logarithm of this loss value and the binary cross entropy loss are multiplied by complementary weights between 0 and 1 which sum to 1, then these are added together to get the final loss value for a U-net output. In this study, the binary cross entropy loss represents 70% of the total loss for the U-net while the remaining 30% is composed of Sorensen–Dice loss; these fractions were selected arbitrarily.

$$SDL = left\frac{2xy}{x+y} \tag{4.2}$$

4.2 Experiment

A classifier for each SAR band and each of the three model architectures is trained separately and saved to file. The "unet" architectures require a previously-trained U-net network which is likewise trained only on a single SAR band. Each network is trained on a fixed set of 135 images then tested on a fixed set of 14 SAR images from the data set associated with each network's specific SAR band. This process is repeated five times for each combination of SAR band and network architecture to reduce the impact of any randomness which may be introduced into the process. The evaluation produces a set of outputs between 0 and 1 which are saved to file. This process is illustrated in Algorithm 2.

After the networks have been trained and evaluated five times, the evaluation data are loaded from disk for post-processing. The classifier outputs are bound between 0 and 1 and these are then converted to binary values 0 and 1 through the use of a simple threshold of 0.5 which converts the classifier outputs into binary values. This binary classification problem allows performance to be quantified through true positives (TP), true negatives (TN), false positives (FP), and false negatives (FN) which allows for various metrics to be calculated,

Algorithm 2 Overall training and evaluation algorithm.

```
generate SAR image data set
generate ground truth classifications for each image
for each evaluation iteration do
    sample data from image data set using Monte Carlo sampling
    divide sampled data into training and testing data sets
    training neural network(s) using training data
    evaluate trained neural network(s) using testing data
    save evaluations to file
end for
```

such as accuracy, F-scores, and Matthews correlation coefficient (MCC). For the purposes of this paper, accuracy and MCC are used for comparing the different forms of data fusion and for comparing the results of the individual bands. This latter metric has been shown to be a better metric compared to F-scores, especially for unbalanced data sets Chicco and Jurman (2020). MCC is calculated using Equation 4.3, and accuracy is calculated by dividing the sum of true positives and true negatives by the total number of SAR images tested.

$$MCC = \frac{TP \times TN - FP \times FN}{\sqrt{(TP + FP)(TP + FN)(TN + FP)(TN + FN)}} \tag{4.3}$$

4.3 Results

Tables 4.4, 4.5, and 4.6 contain the results of the classifier training and evaluation. The C-band performs well across the board, even when the simple "base" classifier model is used, but performance in the other two SAR bands is lower in most cases. The X-band outperforms the S-band in all classifier models tested and is able to achieve perfect performance when the U-net is used to generate a wake mask from the X-band SAR input which is then used as an additional input to the classifier. When the U-net is used in tandem with the classifier, performance is improved across all three bands including perfect performance within the C-

Table 4.4: Single-band classification results using the "base" classifier model. A threshold value of 0.5 was used to convert the continuous classifier output into a binary classification outcome.

SAR Band	MCC	Accuracy
C	0.81	91%
S	0.29	61%
X	0.48	73%

Table 4.5: Single-band classification results using the "clss" classifier model. A threshold value of 0.5 is used to convert the continuous classifier output into a binary outcome.

SAR Band	MCC	Accuracy
C	0.89	94%
S	0.17	54%
X	0.25	56%

band. While this perfect accuracy is likely due to the small data set with a limited amount of sea states, it demonstrates promising results for using neural networks to identify whether remote sensing data contains ship wakes or not.

The results show that classifiers trained and evaluated on a single SAR frequency band could consistently classify the input images as containing or not containing a persistent ship wake. The implemented feature-level data fusion was not as successful as decision-level fusion for increasing the efficacy of the ship wake detection algorithm, with the latter being able to bring performance improvements to initially-poorly performing neural network-based classifiers.

Table 4.6: Single-band classification results using the "unet" classifier model. A threshold value of 0.5 is used to convert the continuous classifier output into a binary outcome.

SAR Band	MCC	Accuracy
C	1.00	100%
S	0.83	91%
X	0.89	94%

Chapter 5

Data Fusion for Machine Learning of Remote Sensing Data

5.1 Data Fusion Models

The goal of data fusion in the context of this wake detection problem is to fuse multiple streams of sensor data and improve ship wake detection when posed as a binary classification problem. These sensors may differ from each other through the observation of different regimes of the electro-magnetic spectrum. Different sensor modalities, such as the fusion of imagery of a single point in time and time-series data, may also provide content which may be able to improve wake detection. Combinations of phenomena or patterns observed across combinations of sensors may allow for an automated system to identify ship wakes with higher certainty, as the whole of a set of heterogeneous data may be more than the sum of its individual components.

Data fusion may occur on three separate levels: the pixel or data level, the feature level, and the decision level. The first method fuses input data at the lowest level and can be thought of as combining each separate sensor into a single, fused sensor. While this method has been used in remote sensing applications, this method is not pursued in this dissertation. The other two levels of data fusion are introduced and their implementation in the current paper are given below. Different forms of data fusion can also be used within the same general

classifier framework. For instance, a classifier may be trained to classify C-band SAR data, another to classify S-band SAR data, and a third to classify X-band SAR data. A fourth classifier utilizing feature-level fusion could then be trained using an image set comprised of a C-band image, an S-band image, and an X-band image. Decision-level fusion could use any combination of these four classifiers to perform classification using data fusion, as others have shown Golrizkhatami and Acan (2018). Further classifiers could be added as well, potentially including classifiers trained on data fused on the pixel level.

Feature-Level Fusion

In feature-level data fusion, features are extracted from multiple inputs and analyzed together by the same system. The aim of this method is to use information from separate data to better understand and give context to extracted features. The modified form of the classifier architecture shown in Figure 4.1 is used for feature-level fusion. Feature-level fusion takes place within the convolutional layers, the first of which extracts features across all input images simultaneously. The input differs in that it is now a set of several SAR images. All of the images in this set are looking at the same sea surface, and all SAR parameters used to generate the image set are identical except that the radar band used to generate each image differs. Any combination of SAR bands may be used in this input, but for this study C-band, S-band, and X-band images formed the input image set for feature-level fusion. A schematic of the classifier used for the 3 band feature-level fusion is shown in Figure 5.1.

Decision-Level Fusion

At the decision-level, fusion occurs by analyzing the input data separate from one another, then using the resulting single-source conclusions to come to a final, fused conclusion. In

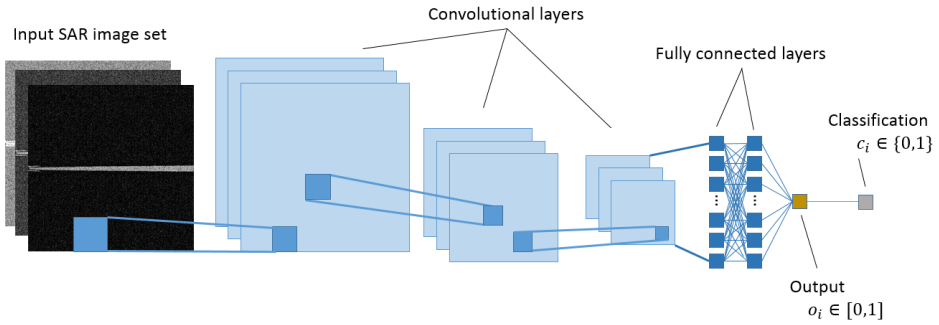

Figure 5.1: Schematic of the neural network classifier using feature-level fusion.

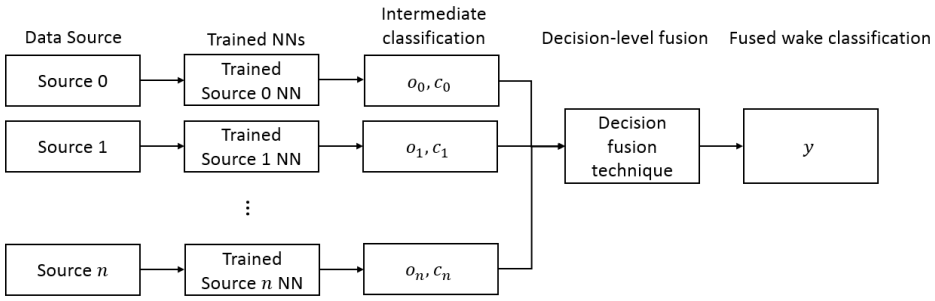

Figure 5.2: Decision-level data fusion flowchart.

this way, analysis is performed as it would be without data fusion, rendering decision-level fusion agnostic to the classification algorithm used. Decision-level fusion is incorporated into the classification procedure as shown in Figure 5.2. Here, the source may refer to a single sensor (e.g., C-band), data fused at the pixel level, or a set of SAR images for feature-level fusion.

Two different decision-level fusion approaches are examined: a Bayes classifier and Dempster–Shafer theory.

Bayes' Classifier

The first approach, the Bayes classifier, is performed by evaluating Equation (5.1)

$$y_{class}(x) = \arg\max_{y \in Y} \sum_{i=0}^{n} P[y \mid c_i] P[c_i \mid x] \tag{5.1}$$

where y_{class} is the Bayes classifier classification, x is the input SAR data, Y is the set of all possible classifications, n is the number of separate neural network classifiers in the data fusion analysis, o_i is the classification made by the ith neural network classifier. The probability of a y classification given an intermediate classification c_i, symbolically $P[y \mid o_i]$, can be derived from data using Bayes' theorem. These probabilities may be empirically estimated from model evaluation results and, in the present binary classification problem, related to the number of true positives (TP), true negatives (TN), false positives (FP), and false negatives (FN) of a given classifier. The derivation of the above equation is as follows.

Given an intermediate classification $c_i \in \{0, 1\}$ which is derived from a value $o_i \in [0, 1]$ given by a classifier model i analyzing input data x, one can determine the probability of a final classification $y \in \{0, 1\}$ given c_i using Bayes' theorem given in Equation (5.2).

$$P[y \mid c_i] = \frac{P[c_i \mid y] P[y]}{P[c_i]} \tag{5.2}$$

Here, $P[c_i \mid y]$ represents the likelihood of a given intermediate classification given a final classification, $P[c_i]$ is the marginal likelihood of a particular intermediate classification, and $P[y]$ represents the prior probability of a given final classification.

For the models tested in this paper, the possible intermediate classifications are a "wake is present" classification and a "wake is not present" classification, and the possible values of the final classification y are the same as those for c_i. Taking a "wake is present" classification to be 1 numerically, and a "wake is not present" classification to be 0, we may view the aforementioned probabilities in terms of true positives, false positives, true negatives, and

false negatives. For example, $P[c_i = 1 \mid y = 1]$ can be viewed as the probability of the ith classifier model giving a "wake is present" classification given that the final classification is also a "wake is present" classification, and therefore a true positive result on the part of the ith classifier. Symbolically, the probability of a true positive in cases where the final classification is "wake is present" is written as

$$P[c_i = 1 \mid y = 1] = \frac{TP}{TP + FN}$$

Similarly, for the other possible combinations of c_i and y

$$P[c_i = 0 \mid y = 1] = \frac{FN}{TP + FN}$$
$$P[c_i = 1 \mid y = 0] = \frac{FP}{TN + FP}$$
$$P[c_i = 0 \mid y = 0] = \frac{TN}{TN + FP}$$

The prior $P[y]$ can be estimated in a similar manner, with the results shown below.

$$P[y = 0] = \frac{TN + FP}{TP + FP + TN + FN}$$
$$P[y = 1] = \frac{TP + FN}{TP + FP + TN + FN}$$

Marginal likelihood is similarly evaluated.

$$P[c_i = 0] = \frac{TN + FN}{TP + FP + TN + FN}$$
$$P[c_i = 1] = \frac{TP + FP}{TP + FP + TN + FN}$$

The resulting possibilities for $P[y \mid c_i]$ are then obtained, and shown below.

$$P[y = 0 \mid c_i = 0] = \frac{TN}{TN + FN} = \left(1 - \frac{FN}{TN + FN}\right)$$
$$P[y = 1 \mid c_i = 0] = \frac{FN}{TN + FN}$$
$$P[y = 0 \mid c_i = 1] = \frac{FP}{TP + FP} = \left(1 - \frac{TP}{TP + FP}\right)$$
$$P[y = 1 \mid c_i = 1] = \frac{TP}{TP + FP}$$

These resulting values are then substituted into Equation (5.1) to yield Equations (5.4) and (5.5).

The probability of a classification c_i given the input x can be determined by the ith classifier. Here, the neural network classifiers output a real number o_i between 0 and 1, where values close to 1 indicate the input SAR image contains a persistent wake and values close to 0 indicate the input SAR images do not contain a persistent wake. If this number is above a certain threshold, c_i is said to be 1 (wake is present), while values of o_i below this threshold result in a c_i of 0 (wake is not present). One may treat o_i as a probability that the ith

classifier predicts a wake is present, and therefore $P[c_i \mid x] = o_i$ is the probability a wake is present in an input and $P[c_i \mid x] = 1 - o_i$ is the probability that a wake is not present in an input. With these two sets of simplifications, Equation (5.1) can thus be rewritten as Equation (5.3), with the definitions of P_{wake} and $P_{no\ wake}$ are given in Equations (5.4) and (5.5), respectively.

$$y_{class}(x) = \begin{cases} 1, & P_{wake} > P_{no\ wake} \\ 0, & \text{otherwise} \end{cases} \tag{5.3}$$

$$P_{wake} = \sum_{i=0}^{n} \frac{TP_i}{TP_i + FP_i} o_i + \frac{FN_i}{TN_i + FN_i} (1 - o_i) \tag{5.4}$$

$$P_{no\ wake} = \sum_{i=0}^{n} \left(1 - \frac{TP_i}{TP_i + FP_i}\right) o_i + \left(1 - \frac{FN_i}{TN_i + FN_i}\right) (1 - o_i) \tag{5.5}$$

One may interpret these equations as using the results of model evaluation to weight the model responses. If a particular model is prone to giving false positives, a high value of o_i, normally an indication of a high probability of a persistent wake within the input, may be a false positive. This results in the classifier placing a higher probability on a "no wake present" classification than o_i alone would suggest. Similarly, a high rate of false negatives and a low o_i may lead to the Bayes classifier giving a higher probability of a "wake is present" classification than one would expect just looking at o_i alone. This approach is in-line with Bayesian inference, which uses past data to update current hypotheses.

Dempster–Shafer Theory

Dempster–Shafer theory attributes degrees of belief to different hypotheses or sets of hypotheses that belong to a universe X based on evidence and through a process of combination allows for different sets of evidence to be fused together such that refined degrees of belief accounting for all the fused evidence are ascertained Shafer (1976). In the approach taken here, each classifier is treated as a sensor which quantifies the degree of belief that a wake is either present or not present in the input. The numerical output of the ith classifier o_i is bounded between 0 and 1 where a value of 0 represents absolute certainty that there is no wake present in the input and a value of 1 represents absolute certainty that a wake is present in the input. Here, $m_i(y = 1) = o_i$ is taken as the degree of belief that hypothesis $y = 1$ according to classifier i, meaning a wake is present, is true and correspondingly $m_i(y = 0) = 1 - o_i$ is the degree of belief that a wake is not present ($y = 0$). Here, the mass functions m_i of each hypothesis or set of hypotheses must sum to 1 and the mass function of the null hypothesis must equal 0. With m_i quantified for all classifiers, Equation 5.6 is used to produce m_{fused} for a hypothesis or set of hypotheses A given two sets of beliefs m_1 and m_2.

$$m_{fused}(A) = \frac{\sum_{B \cap C = A; A \neq \varnothing} m_1(B) m_2(C)}{1 - k} \tag{5.6}$$

where conflict k is defined as

$$k = \sum_{B \cap C = \varnothing} m_1(B) m_2(C)$$

Dempster–Shafer theory defines an upper and lower bound of degree of belief for each hypothesis or set of hypotheses, named plausibility Pl and belief Bel, respectively, which are

defined below. Unlike a confidence interval where one might assume a particular distribution of probabilities within these bounds, e.g. Gaussian, no such assumption may be made about the distribution of probabilities within these bounds.

$$Pl(A) = \sum_{A \cap B \neq \varnothing} m(B)$$

$$Bel(A) = \sum_{B \subseteq A} m(A)$$

This form is useful for quantifying the degree of uncertainty in each hypothesis. However, it may be simpler to make decisions such as one for classification using a probability value for each singular hypothesis. Smets and Kennes (1994) define a pignistic probability P_{bet} for each hypothesis singleton y using the following formula, where the vertical bar operator represents the cardinality of argument set. The resulting value is then converted to a binary classification outcome using a threshold to determine the final, fused classification outcome.

$$P_{bet}(y) = \sum_{y \in A \subseteq X} \frac{m_{fused}(A)}{|A|}$$

5.2 Training and Experiment

The training process for the inclusion of data fusion follows nearly the same process as that for the single SAR band models. The models are trained for 60 epochs using 135 training images and evaluated using 14 testing images, both of which are split 50/50 between the "wake is present" and "wake is not present" ground truth labels. As this process involves data from more than one SAR frequency band, the input data for feature-level fusion is composed

of several SAR images of different bands, each of which occupies a separate channel in the input data tensor. Similarly, the U-net networks using feature-level fusion also receive data from multiple SAR bands in the same format as the classifier where each channel in the input data corresponds to a different SAR band. Metadata identifiers are assigned to each SAR image so that all of the input SAR data are viewing the same wake and sea surface and have all of the same platform parameters except the SAR frequency band used to simulate the image. As in the single band study, the "clss" model has an extra input channel used to control for the increase in input data size that the "unet" model sees compared to the "base" model. In this case, the "clss" model is given a duplicate of the first channel's data. This train-and-evaluate process is also repeated for a total of five iterations to reduce the impact of any randomness in the training process. The same training hyperparameters are used for training the networks used for feature-level fusion as well as a threshold value of 0.5 for converting the continuous outputs of the classifier to binary classification outcomes.

The data of S-band and X-band SAR images are used in this experiment while the C-band images are omitted due to the near-perfect performance of all classifier models trained on the C-band images. This is to model a case where two classifiers or sensors with mediocre performance are fused in order to bring better results. The feature-level fusion of these two SAR bands, referred to in text as "SX", requires further train-and-evaluate cycles while decision-level data fusion conducted using Bayes classifier and Dempster–Shafer theory reuses the single-band classifier evaluation results from the previous chapter, thus no further simulations are required to evaluate decision-level fusion.

Table 5.1: Feature-level and decision-level fusion performed using the "base" classifier model.

SAR Band	MCC	Accuracy
SX	0.26	63%
Bayes classifier (S, X)	0.57	74%
Dempster–Shafer (S, X)	0.43	66%

5.3 Results

Tables 5.1, 5.2, and 5.3 give the results of the incorporation of data fusion within the classification problem. In all cases, at least one decision-level fusion yielded an improvement to the classifier performance when measured by both MCC and accuracy while the feature-level fusion method implemented here did not provide the same level of performance improvement and in some cases led to a performance drop compared to the best-performing single-band classifier. Dempster–Shafer theory and the Bayes classifier both perform generally well. These methods are applied to a binary classification problem here but may also be extended for interval-based analysis performed on the wake, such as estimating a range of speeds that the vessel that produced the wake may have been travelling at.

The use of three different classifier models yields differing classifier performance, allowing one to examine how data fusion aids different classifiers. The "base" classifier model has poorer S-band and X-band classification performance compared to those of the "unet" classifier model, but through data fusion these poorly-performing classifiers are able to achieve higher MCC and accuracy without any additional training or data. This improvement in performance is not as significant as the performance increase due to using a more complex model like the "unet" one, however. On the opposite side, the use of decision-level fusion on the "unet" model which has near-perfect classification performance does not degrade performance. This shows that data fusion may be a viable approach to improving classification or other analysis even if the fused sensor outputs or analysis results do not perform well individually.

Table 5.2: Feature-level and decision-level fusion performed using the "clss" classifier model.

SAR Band	MCC	Accuracy
SX	0.20	59%
Bayes classifier (S, X)	0.27	60%
Dempster–Shafer (S, X)	0.21	54%

Table 5.3: Feature-level and decision-level fusion performed using the "unet" classifier model.

SAR Band	MCC	Accuracy
SX	0.97	99%
Bayes classifier (S, X)	1.00	100%
Dempster–Shafer (S, X)	0.89	94%

5.4 Multi-Physics Data Fusion

Data fusion for multiple SAR bands shows promise for improving probability of detection for ship wakes and is the first step in a more-comprehensive plan for data fusion across sensor modalities and across data types. This approach aims to utilize the strengths of different sensor modalities in order to improve classification accuracy, for example, in cases where a single-source SAR and a single-source IR detection system both show a small probably for a wake being present, does fusion of these data sources yield a definitive "no," or does the fusion of SAR and IR data in this case reverse this preliminary result.

One potential test case to study this potential avenue for future work would be to identify environments where multiple sensor modalities yield differing observations. For example, identifying cases where a ship produces an identifiable wake in an IR image but not a visible one in a corresponding SAR image, or a case where a ship produces a faint ship wake in both IR and SAR images. Collecting combinations of outcomes like these will give a data set for testing multi-physics data fusion in various circumstances in order to determine how beneficial it is to fuse multiple sensor modalities. In particular, it will help evaluate whether neural networks and data fusion methods can utilize combinations of features across sensor

modalities to improve classification accuracy. Figure 5.3 shows a ship wake viewed by SAR and IR. This environment has a near-surface temperature gradient that results in the ship mixing warm surface water with cold sub-surface water, creating a dark stream of colder water compared to the surrounding ambient ocean. This mixing creates a net buoyancy force that generates internal gravity waves on the surface. These internal gravity waves do not advect the cold water in the wake center line, causing the IR signature of the wake to have a different character than the one in the SAR image. Identifying situations like these may provide interesting test cases for multi-physics data fusion studies.

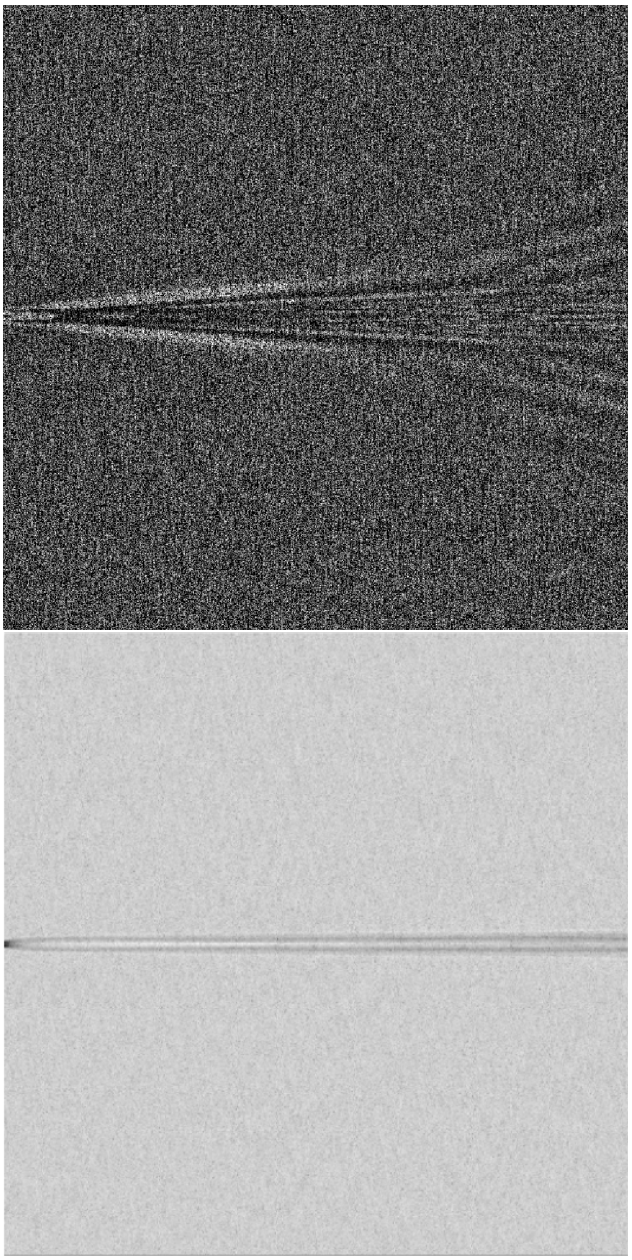

Figure 5.3: (Top) S-band SAR image and (bottom) IR image of a ship wake in an environment with a near-surface temperature gradient. Note that the wake as viewed by IR does not have the same shape as the wake when viewed by the SAR sensor due to capturing different sets of physical phenomena.

Chapter 6

Conclusions and Future Work

6.1 Conclusions

This dissertation covers the implementation of a simulation workflow that is designed to simulate the turbulent, persistent wake of a surface ship for tens of kilometers downstream of the stern along with the associated perturbations to ambient surface active substances (SAS) and the local surface wave spectrum in a computationally-tractable manner. The data from these simulations are then used to generate simulated remote sensing imagery. Synthetic aperture radar (SAR) and infra-red (IR) images of these ship wakes are created using physics-based modeling and simulation methods. Three SAR bands and two IR bands are selected for data generation and collected into data sets for training and testing.

Next, the simulated data are curated and assigned ground truth labels related to the presence or absence of a persistent wake. Any additional data used for supervised training such as wake masks for the U-net for image segmentation is generated at this point. The convolutional neural network–based classifiers are then designed and trained on the curated SAR data. Three different network architectures are examined for the purpose of determining the impact of using a U-net neural network to segment the input data into regions where a wake is likely present and regions where one is likely not present. Separate networks are trained for each combination of architecture and data source which are then evaluated by withholding part of the training data for each SAR band then testing using the withheld portion. Results

show that the network that integrates a U-net neural network have improved wake detection results over the simpler networks. The performance of the different SAR bands is also evaluated, showing that the networks trained and tested on C-band SAR imagery have the best performance.

Data fusion methods are overviewed and their implementations outlined. Two data fusion modalities are examined: feature-level fusion where fusion occurs after feature extraction, and decision-level fusion where fusion occurs after each individual data source is analyzed using its own pre-trained neural network. Two decision-level fusion methods, Bayes' classifier and Dempster–Shafer theory, are described and tested alongside feature-level fusion. These data fusion approaches are evaluated for the ship wake detection problem, and they show that decision-level fusion shows an improved wake detection performance over the tested approaches that do not utilize data fusion. In particular, the use of decision-level fusion and the classifier architecture that uses the U-net in tandem with a convolutional neural network were able to achieve perfect or nearly-perfect detection results. Plans for testing data fusion across multiple sensor modalities, such as SAR and IR, are also discussed.

6.2 Future Work

Several topics that constitute future work which extends this research have been completed and are worth mentioning. Sobien et al. (2023) examines the use of data augmentations analogous to data dropout and sensor noise, both phenomena which may be encountered during the operation of a real remote sensor, and their impact on neural network evaluation. Honea et al. (2022) looks at using mathematical filtering techniques such as Radon transforms to pre-process raw remote sensing data with the intention to better reveal patterns in the images.

The methodologies developed and explored in this work can be expanded to include data fusion of other forms of data, not just beyond SAR and IR picture data, but also data types such as time-series data and spectral data. These data may be useful for the targeted ship wake detection problem as well as a more general multi-physics, multi-sensor data fusion problem. Additionally, more simulations may be performed with an even wider range of parameters to understand how robust the models are when exposed to out-of-domain simulations. Testing out different sea surface wave spectrum models, different turbulence models, and more types of ships are examples of starting points for future work.

Uncertainty quantification for the detection methods is another avenue for future research. Being able to estimate the confidence of whether a ship wake is in an image or not can be very beneficial for real-world use as well as for model development and comparisons across data fusion methods as it can provide a different perspective of model performance compared to simpler metrics such as accuracy and F1 scores. Incorporating uncertainty quantification into the model output itself may also yield benefits for data fusion, where decision rules may be applied to determine which sensors may be most promising to fuse together. Uncertainty and error quantification of the hydrodynamic and electromagnetic models may be beneficial for similar reasons, especially since error and uncertainty can propagate between simulations. Such quantification may aid in the selection of physical models used in these simulations in order to provide more realistic simulated remote sensing images. Further neural network architectures and data fusion methodologies may also be tested to examine their performance relative to these relatively-simple networks and data fusion models.

The use of simulated remote sensing data in model development and training poses an interesting challenge as the performance of these models when trained on simulated data and tested on real-world data is unknown. Future studies may examine the transfer learning capacity of these models to determine how much performance is impacted when trained on

one source of data and evaluated on the other. Similar studies may be beneficial to determine if supplementing a real-world data set with simulated images grants performance benefits. This situation may arise when real-world data covers a limited scope and the model users seek to deploy trained networks to a new environment where there is very limited or no existing real-world training data.

Bibliography

Ali Ahmadibebi, Branndon Jones, and Amir Shirkhodaie. Physics-based wake modeling for marine vehicles activity recognition based on simulated synthetic aperture radar. In Weilin "Will" Hou and Linda J. Mullen, editors, *Ocean Sensing and Monitoring XIV*, page 25, Orlando, United States, May 2022. SPIE. ISBN 978-1-5106-5112-8 978-1-5106-5113-5. doi: 10.1117/12.2629032. URL https://www.spiedigitallibrary.org/conference-proceedings-of-spie/12118/2629032/Physics-based-wake-modeling-for-marine-vehicles-activity-recognition-based/10.1117/12.2629032.full.

Ali Ahmadibeni, Branndon Jones, and Amir Shirkhodaie. Transfer learning from simulated SAR imagery using multi-output convolutional neural networks. In Michael E. Zelinski, Tarek M. Taha, Jonathan Howe, Abdul A. Awwal, and Khan M. Iftekharuddin, editors, *Applications of Machine Learning 2020*, page 30, Online Only, United States, August 2020. SPIE. ISBN 978-1-5106-3828-0 978-1-5106-3829-7. doi: 10.1117/12.2568922. URL https://www.spiedigitallibrary.org/conference-proceedings-of-spie/11511/2568922/Transfer-learning-from-simulated-SAR-imagery-using-multi-output-convolutional/10.1117/12.2568922.full.

John E Bertie and Zhida Lan. Infrared Intensities of Liquids XX: The Intensity of the OH Stretching Band of Liquid Water Revisited, and the Best Current Values of the Optical Constants of H20(I) at 25 °C between 15,000 and 1 cm^{-1}. *Applied Spectroscopy*, 50(8): 1047–1057, 1996.

Ruth Branch, C. Chris Chickadel, and Andrew T. Jessup. Infrared emissivity of seawater and foam at large incidence angles in the 3–14 m wavelength range. *Remote Sensing of Environment*, 184:15–24, October 2016. ISSN 00344257. doi: 10.1016/j.rse.2016.06.009. URL https://linkinghub.elsevier.com/retrieve/pii/S0034425716302474.

D.M. Buede and P. Girardi. A target identification comparison of bayesian and dempster-shafer multisensor fusion. *IEEE Transactions on Systems, Man, and Cybernetics - Part A: Systems and Humans*, 27(5):569–577, 1997. doi: 10.1109/3468.618256.

Alexey F. Bunkin, Vladimir K. Klinkov, Vladislav A. Lukyanchenko, and Sergey M. Pershin. Ship wake detection by Raman lidar. *Applied Optics*, 50(4):A86, February 2011. ISSN 0003-6935, 1539-4522. doi: 10.1364/AO.50.000A86. URL https://www.osapublishing.org/abstract.cfm?URI=ao-50-4-A86.

James B. Campbell and Randolph H. Wynne. *Introduction to Remote Sensing*. Guilford Press, 5th edition, 2011. ISBN 978-1-60918-177-2.

Ni-Bin Chang and Kaixu Bai. *Multisensor Data Fusion and Machine Learning for Environmental Remote Sensing*. CRC Press, 2018.

Jie Cheng, Xiaolong Cheng, Shunlin Liang, Raquel Niclòs, Aixiu Nie, and Qiang Liu. A Lookup Table-Based Method for Estimating Sea Surface Hemispherical Broadband Emissivity Values (8–13.5 m). *Remote Sensing*, 9(3):245, March 2017. ISSN 2072-4292. doi: 10.3390/rs9030245. URL http://www.mdpi.com/2072-4292/9/3/245.

Davide Chicco and Giuseppe Jurman. The advantages of the Matthews correlation coefficient (MCC) over F1 score and accuracy in binary classification evaluation. *BMC Genomics*, 21(1):6, December 2020. ISSN 1471-2164. doi: 10.1186/s12864-019-6413-7. URL https://bmcgenomics.biomedcentral.com/articles/10.1186/s12864-019-6413-7.

Renato Cini, Pietro Paolo Lombardini, Claudia Manfredi, and Enrico Cini. Ripples damping due to monomolecular films. *Journal of Colloid and Interface Science*, 119(1):74–80, September 1987. ISSN 00219797. doi: 10.1016/0021-9797(87)90246-3. URL https://linkinghub.elsevier.com/retrieve/pii/0021979787902463.

C.J. Cohen. Early history of remote sensing. In *Proceedings 29th Applied Imagery Pattern Recognition Workshop*, pages 3–9, Washington, DC, USA, 2000. IEEE Comput. Soc. ISBN 978-0-7695-0978-5. doi: 10.1109/AIPRW.2000.953595. URL http://ieeexplore.ieee.org/document/953595/.

A. D. D. Craik and S. Leibovich. A rational model for Langmuir circulations. *Journal of Fluid Mechanics*, 73(3):401–426, February 1976. ISSN 0022-1120, 1469-7645. doi: 10.1017/S0022112076001420. URL https://www.cambridge.org/core/product/identifier/S0022112076001420/type/journal_article.

Roberto Del Prete, Maria Daniela Graziano, and Alfredo Renga. First Results on Wake Detection in SAR Images by Deep Learning. *Remote Sensing*, 13(22):4573, November 2021. ISSN 2072-4292. doi: 10.3390/rs13224573. URL https://www.mdpi.com/2072-4292/13/22/4573.

Kaiyang Ding, Junfeng Yang, Hui Lin, Zhao Wang, Deyi Wang, Xiaohao Wang, Kai Ni, and Qian Zhou. Towards real-time detection of ships and wakes with lightweight deep learning model in Gaofen-3 SAR images. *Remote Sensing of Environment*, 284: 113345, January 2023. ISSN 00344257. doi: 10.1016/j.rse.2022.113345. URL https://linkinghub.elsevier.com/retrieve/pii/S0034425722004515.

Harry D. Downing and Dudley Williams. Optical constants of water in the infrared. *Journal of Geophysical Research*, 80(12):1656–1661, April 1975. ISSN 01480227. doi: 10.1029/JC080i012p01656. URL http://doi.wiley.com/10.1029/JC080i012p01656.

Riccardo Droghei, Bruno Buongiorno Nardelli, and Rosalia Santoleri. A New Global Sea Surface Salinity and Density Dataset From Multivariate Observations (1993–2016). *Frontiers in Marine Science*, 5:84, March 2018. ISSN 2296-7745. doi: 10.3389/fmars.2018.00084. URL http://journal.frontiersin.org/article/10.3389/fmars.2018.00084/full.

Daniel Druce, Xiaoye Tong, Xia Lei, Tao Guo, Cecile M.M. Kittel, Kenneth Grogan, and Christian Tottrup. An Optical and SAR Based Fusion Approach for Mapping Surface Water Dynamics over Mainland China. *Remote Sensing*, 13(9):1663, April 2021. ISSN 2072-4292. doi: 10.3390/rs13091663. URL https://www.mdpi.com/2072-4292/13/9/1663.

G. Franceschetti, M. Migliaccio, and D. Riccio. On ocean SAR raw signal simulation. *IEEE Transactions on Geoscience and Remote Sensing*, 36(1):84–100, January 1998. ISSN 01962892. doi: 10.1109/36.655320. URL http://ieeexplore.ieee.org/document/655320/.

D Friedman. Infrared Characteristics of Ocean Water (1.5-15). *Applied Optics*, 8(10): 2073–2078, October 1969. doi: 10.1364/AO.8.002073. URL http://opg.optica.org/ao/abstract.cfm?URI=ao-8-10-2073.

R. Gens and J. L. Van Genderen. Review Article SAR interferometry—issues, techniques, applications. *International Journal of Remote Sensing*, 17(10):1803–1835, July 1996. ISSN 0143-1161, 1366-5901. doi: 10.1080/01431169608948741. URL https://www.tandfonline.com/doi/full/10.1080/01431169608948741.

M. Gilman, A. Soloviev, and H. Graber. Study of the Far Wake of a Large Ship. *Journal of Atmospheric and Oceanic Technology*, 28(5):720–733, May 2011. ISSN 0739-0572, 1520-0426. doi: 10.1175/2010JTECHO791.1. URL http://journals.ametsoc.org/doi/10.1175/2010JTECHO791.1.

S. Giompapa, R. Croci, R. Di Stefano, A. Farina, F. Gini, A. Graziano, and F. Lapierre. Naval target classification by fusion of IR and EO sensors. Florence, Italy, October 2007. doi: 10.1117/12.738072. URL http://proceedings.spiedigitallibrary.org/proceeding.aspx?doi=10.1117/12.738072.

Zahra Golrizkhatami and Adnan Acan. ECG classification using three-level fusion of different feature descriptors. *Expert Systems with Applications*, 114:54–64, December 2018. ISSN 09574174. doi: 10.1016/j.eswa.2018.07.030. URL https://linkinghub.elsevier.com/retrieve/pii/S0957417418304469.

Maria Graziano, Marco D'Errico, and Giancarlo Rufino. Wake Component Detection in X-Band SAR Images for Ship Heading and Velocity Estimation. *Remote Sensing*, 8(6): 498, June 2016. ISSN 2072-4292. doi: 10.3390/rs8060498. URL http://www.mdpi.com/2072-4292/8/6/498.

Maria Graziano, Marco Grasso, and Marco D'Errico. Performance Analysis of Ship Wake Detection on Sentinel-1 SAR Images. *Remote Sensing*, 9(11):1107, October 2017. ISSN 2072-4292. doi: 10.3390/rs9111107. URL http://www.mdpi.com/2072-4292/9/11/1107.

Maria Daniela Graziano, Alfredo Renga, and Antonio Moccia. Integration of Automatic Identification System (AIS) Data and Single-Channel Synthetic Aperture Radar (SAR) Images by SAR-Based Ship Velocity Estimation for Maritime Situational Awareness. *Remote Sensing*, 11(19):2196, September 2019. ISSN 2072-4292. doi: 10.3390/rs11192196. URL https://www.mdpi.com/2072-4292/11/19/2196.

Owen M Griffin, Rodney D Peltzer, Arthur M Reed, and Robert F Beck. Remote Sensing of Surface Ship Wakes. *Naval Engineers Journal*, 1992.

Robert Grimming, Patrick Leslie, Derek Burrell, Gerald Holst, Brian Davis, and Ronald Driggers. Refining Atmosphere Profiles for Aerial Target Detection Models. *Sensors*,

21(21):7067, October 2021. ISSN 1424-8220. doi: 10.3390/s21217067. URL https://www.mdpi.com/1424-8220/21/21/7067.

A.H. Gunatilaka and B.A. Baertlein. Feature-level and decision-level fusion of noncoincidently sampled sensors for land mine detection. *IEEE Transactions on Pattern Analysis and Machine Intelligence*, 23(6):577–589, June 2001. ISSN 01628828. doi: 10.1109/34.927459. URL http://ieeexplore.ieee.org/document/927459/.

George M. Hale and Marvin R. Querry. Optical Constants of Water in the 200-nm to 200- m Wavelength Region. *Applied Optics*, 12(3):555, March 1973. ISSN 0003-6935, 1539-4522. doi: 10.1364/AO.12.000555. URL https://opg.optica.org/abstract.cfm?URI=ao-12-3-555.

Samuel Hassid. Collapse of turbulent wakes in stably stratified media. *Journal of Hydronautics*, 14(1):25–32, January 1980. ISSN 0022-1716, 1555-5909. doi: 10.2514/3.48175. URL https://arc.aiaa.org/doi/10.2514/3.48175.

Eugene Hecht. *Optics*. Pearson Education, Inc, Boston, 5 ed edition, 2017. ISBN 978-0-13-397722-6.

L. C. Henyey and J. L. Greenstein. Diffuse radiation in the Galaxy. *The Astrophysical Journal*, 93:70, January 1941. ISSN 0004-637X, 1538-4357. doi: 10.1086/144246. URL http://adsabs.harvard.edu/doi/10.1086/144246.

Erik Higgins, Jonathan Pitt, and Eric Paterson. Multi-Scale Localized Perturbation Method in OpenFOAM. *Fluids*, 5(4):250, December 2020. ISSN 2311-5521. doi: 10.3390/fluids5040250. URL https://www.mdpi.com/2311-5521/5/4/250.

Erik T Higgins. *Multi-Scale Localized Perturbation Method for Geophysical Fluid Flows*.

Thesis, Virginia Polytechnic Institute and State University, Blacksburg, Virginia, USA, August 2020.

Cassidy Honea, Erik Higgins, Daniel Sobien, and Justin Kauffman. Synthetic Aperture Radar: Utilizing Radon Image Transformations to Enhance the Detection of Ship Wakes. *The ITEA Journal of Test and Evaluation*, 43(4):197–201, December 2022.

Nathan Inkawhich, Matthew J. Inkawhich, Eric K. Davis, Uttam K. Majumder, Erin Tripp, Chris Capraro, and Yiran Chen. Bridging a Gap in SAR-ATR: Training on Fully Synthetic and Testing on Measured Data. *IEEE Journal of Selected Topics in Applied Earth Observations and Remote Sensing*, 14:2942–2955, 2021. ISSN 1939-1404, 2151-1535. doi: 10.1109/JSTARS.2021.3059991. URL https://ieeexplore.ieee.org/document/9356129/.

IOC, SCOR, and IAPSO. The international thermodynamic equation of seawater – 2010: Calculation and use of thermodynamic properties. Manuals and Guides 56, Intergovernmental Oceanographic Commission, 2010. URL www.TEOS-10.org.

R.I Issa. Solution of the implicitly discretised fluid flow equations by operator-splitting. *Journal of Computational Physics*, 62(1):40–65, January 1986. ISSN 00219991. doi: 10.1016/0021-9991(86)90099-9. URL https://linkinghub.elsevier.com/retrieve/pii/0021999186900999.

Vivian Issa and Zahir A. Daya. Modeling the turbulent trailing ship wake in the infrared. *Applied Optics*, 53(19):4282, July 2014. ISSN 1559-128X, 2155-3165. doi: 10.1364/AO.53.004282. URL https://www.osapublishing.org/abstract.cfm?URI=ao-53-19-4282.

Yue Jin, Yang Ruliang, and Huan Ruohong. Pixel level fusion for multiple SAR images using PCA and wavelet transform. In *2006 CIE International Conference on Radar*, pages 1–4, Shanghai, China, October 2006. IEEE. ISBN 978-0-7803-9582-4 978-0-7803-9583-1. doi: 10.1109/ICR.2006.343209. URL http://ieeexplore.ieee.org/document/4148315/.

Branndon Jones, Ali Ahmadibeni, and Amir Shirkhodaie. Marine vehicles modeling and simulated SAR imagery datasets generation. In Weilin "Will" Hou and Robert A. Arnone, editors, *Ocean Sensing and Monitoring XII*, page 24, Online Only, United States, April 2020. SPIE. ISBN 978-1-5106-3617-0 978-1-5106-3618-7. doi: 10.1117/12.2558270. URL https://www.spiedigitallibrary.org/conference-proceedings-of-spie/11420/2558270/Marine-vehicles-modeling-and-simulated-SAR-imagery-datasets-generation/10.1117/12.2558270.full.

Branndon Jones, Ali Ahmadibeni, and Amir Shirkhodaie. Simulated SAR imagery generation of marine vehicles and associated wakes using electromagnetic modeling and simulation techniques. In Michael E. Zelinski, Tarek M. Taha, and Jonathan Howe, editors, *Applications of Machine Learning 2021*, page 12, San Diego, United States, August 2021. SPIE. ISBN 978-1-5106-4524-0 978-1-5106-4525-7. doi: 10.1117/12.2600500. URL https://www.spiedigitallibrary.org/conference-proceedings-of-spie/11843/2600500/Simulated-SAR-imagery-generation-of-marine-vehicles-and-associated-wakes/10.1117/12.2600500.full.

Ki-mook Kang and Duk-jin Kim. Ship Velocity Estimation From Ship Wakes Detected Using Convolutional Neural Networks. *IEEE Journal of Selected Topics in Applied Earth Observations and Remote Sensing*, 12(11):4379–4388, November 2019. ISSN 1939-1404, 2151-1535. doi: 10.1109/JSTARS.2019.2949006. URL https://ieeexplore.ieee.org/document/8896951/.

Oktay Karakus and Alin Achim. Ship Wake Detection in X-band SAR Images Using Sparse GMC Regularization. In *ICASSP 2019 - 2019 IEEE International Conference on Acoustics, Speech and Signal Processing (ICASSP)*, pages 2182–2186, Brighton, United King-

dom, May 2019. IEEE. ISBN 978-1-4799-8131-1. doi: 10.1109/ICASSP.2019.8683489. URL https://ieeexplore.ieee.org/document/8683489/.

M Khazaee, H Ahmadi, M Omid, A Banakar, and A Moosavian. Feature-level fusion based on wavelet transform and artificial neural network for fault diagnosis of planetary gearbox using acoustic and vibration signals. *Insight - Non-Destructive Testing and Condition Monitoring*, 55(6):7, June 2013.

Sungho Kim, Woo-Jin Song, and So-Hyun Kim. Robust Ground Target Detection by SAR and IR Sensor Fusion Using Adaboost-Based Feature Selection. *Sensors*, 16(7):1117, July 2016. ISSN 1424-8220. doi: 10.3390/s16071117. URL http://www.mdpi.com/1424-8220/16/7/1117.

Sungho Kim, Woo-Jin Song, and So-Hyun Kim. Double Weight-Based SAR and Infrared Sensor Fusion for Automatic Ground Target Recognition with Deep Learning. *Remote Sensing*, 10(2):72, January 2018. ISSN 2072-4292. doi: 10.3390/rs10010072. URL http://www.mdpi.com/2072-4292/10/1/72.

B. E. Launder. Second-moment closure and its use in modelling turbulent industrial flows. *International Journal for Numerical Methods in Fluids*, 9(8):963–985, August 1989. ISSN 0271-2091, 1097-0363. doi: 10.1002/fld.1650090806. URL https://onlinelibrary.wiley.com/doi/10.1002/fld.1650090806.

B.E. Launder and D.B. Spalding. The numerical computation of turbulent flows. *Computer Methods in Applied Mechanics and Engineering*, 3(2):269–289, March 1974. ISSN 00457825. doi: 10.1016/0045-7825(74)90029-2. URL https://linkinghub.elsevier.com/retrieve/pii/0045782574900292.

Martin P. Levesque and Daniel St-Germain. Generation of synthetic IR sea images. In Milton J. Triplett, Wendell R. Watkins, and Ferdinand H. Zegel, editors, *Characterization,*

Propagation, and Simulation of Infrared Scenes, volume 1311, pages 352 – 357. SPIE, 1990. doi: 10.1117/12.21849. URL https://doi.org/10.1117/12.21849. Backup Publisher: International Society for Optics and Photonics.

Benjamin Lewis, Omar DeGuchy, Joseph Sebastian, and John Kaminski. Realistic SAR data augmentation using machine learning techniques. In Edmund Zelnio and Frederick D. Garber, editors, *Algorithms for Synthetic Aperture Radar Imagery XXVI*, page 12, Baltimore, United States, May 2019. SPIE. ISBN 978-1-5106-2639-3 978-1-5106-2640-9. doi: 10.1117/12.2518452. URL https://www.spiedigitallibrary.org/conference-proceedings-of-spie/10987/2518452/Realistic-SAR-data-augmentation-using-machine-learning-techniques/10.1117/12.2518452.full.

Qian Li, Yanmin Zhang, Yunhua Wang, Yining Bai, Yushi Zhang, and Xin Li. Numerical Simulation of SAR Image for Sea Surface. *Remote Sensing*, 14(3):439, January 2022. ISSN 2072-4292. doi: 10.3390/rs14030439. URL https://www.mdpi.com/2072-4292/14/3/439.

Wangyan Li, Zidong Wang, Guoliang Wei, Lifeng Ma, Jun Hu, and Derui Ding. A survey on multisensor fusion and consensus filtering for sensor networks. *Discrete Dynamics in Nature and Society*, 2015:1–12, 2015. doi: https://doi.org/10.1155/2015/683701.

Tsung-Yi Lin, Piotr Dollár, Ross Girshick, Kaiming He, Bharath Hariharan, and Serge Belongie. Feature Pyramid Networks for Object Detection. Technical Report arXiv:1612.03144, arXiv, April 2017. URL http://arxiv.org/abs/1612.03144. arXiv:1612.03144 [cs] type: article.

Meijie Liu, Yongshou Dai, Jie Zhang, Xi Zhang, Junmin Meng, and Qinchuan Xie. PCA-based sea-ice image fusion of optical data by HIS transform and SAR data by wavelet

transform. *Acta Oceanologica Sinica*, 34(3):59–67, March 2015. ISSN 0253-505X, 1869-1099. doi: 10.1007/s13131-015-0634-7. URL http://link.springer.com/10.1007/s13131-015-0634-7.

Wei Liu, Dragomir Anguelov, Dumitru Erhan, Christian Szegedy, Scott Reed, Cheng-Yang Fu, and Alexander C. Berg. SSD: Single Shot MultiBox Detector. volume 9905, pages 21–37. 2016. doi: 10.1007/978-3-319-46448-0_2. URL http://arxiv.org/abs/1512.02325. arXiv:1512.02325 [cs].

Lijun Lu, Wenjun Xie, Jixian Zhang, Guoman Huang, Qiwei Li, and Zheng Zhao. Woodland Extraction from High-Resolution CASMSAR Data Based on Dempster-Shafer Evidence Theory Fusion. *Remote Sensing*, 7(4):4068–4091, April 2015. ISSN 2072-4292. doi: 10.3390/rs70404068. URL http://www.mdpi.com/2072-4292/7/4/4068.

David Lyzenga. Numerical Simulation of Synthetic Aperture Radar Image Spectra for Ocean Waves. *IEEE Transactions on Geoscience and Remote Sensing*, GE-24(6):863–872, November 1986. ISSN 0196-2892. doi: 10.1109/TGRS.1986.289701. URL http://ieeexplore.ieee.org/document/4072557/.

David R. Lyzenga and John R. Bennett. Full-spectrum modeling of synthetic aperture radar internal wave signatures. *Journal of Geophysical Research*, 93(C10):12345, 1988. ISSN 0148-0227. doi: 10.1029/JC093iC10p12345. URL http://doi.wiley.com/10.1029/JC093iC10p12345.

Zbyněk Malenovský, Helmut Rott, Josef Cihlar, Michael E. Schaepman, Glenda García-Santos, Richard Fernandes, and Michael Berger. Sentinels for science: Potential of Sentinel-1, -2, and -3 missions for scientific observations of ocean, cryosphere, and land. *Remote Sensing of Environment*, 120:91–101, May 2012. ISSN 00344257. doi:

10.1016/j.rse.2011.09.026. URL https://linkinghub.elsevier.com/retrieve/pii/S0034425712000648.

David Malmgren-Hansen, Anders Kusk, Jørgen Dall, Allan Aasbjerg Nielsen, Rasmus Engholm, and Henning Skriver. Improving sar automatic target recognition models with transfer learning from simulated data. *IEEE Geoscience and Remote Sensing Letters*, 14 (9):1484–1488, 2017. doi: 10.1109/LGRS.2017.2717486.

Armando Marino, Maria Sanjuan-Ferrer, Irena Hajnsek, and Kazuo Ouchi. Ship Detection with Spectral Analysis of Synthetic Aperture Radar: A Comparison of New and Well-Known Algorithms. *Remote Sensing*, 7(5):5416–5439, April 2015. ISSN 2072-4292. doi: 10.3390/rs70505416. URL http://www.mdpi.com/2072-4292/7/5/5416.

M. D. Mermelstein, E. P. Shettle, E. H. Takken, and R. G. Priest. Infrared radiance and solar glint at the ocean–sky horizon. *Applied Optics*, 33(25):6022–6034, September 1994. ISSN 0003-6935, 1539-4522. doi: 10.1364/AO.33.006022. URL https://www.osapublishing.org/abstract.cfm?URI=ao-33-25-6022.

J. H. Milgram, R. D. Peltzer, and O. M. Griffin. Suppression of short sea waves in ship wakes: Measurements and observations. *Journal of Geophysical Research: Oceans*, 98 (C4):7103–7114, April 1993a. ISSN 01480227. doi: 10.1029/92JC02612. URL http://doi.wiley.com/10.1029/92JC02612.

J. H. Milgram, Richard A. Skop, Rodney D. Peltzer, and Owen M. Griffin. Modeling short sea wave energy distributions in the far wakes of ships. *Journal of Geophysical Research: Oceans*, 98(C4):7115–7124, April 1993b. ISSN 01480227. doi: 10.1029/92JC02611. URL http://doi.wiley.com/10.1029/92JC02611.

F.J. Millero. *Chemical Oceanography*. CRC Press, Boca Raton, Florida, 4 ed edition, 2016. ISBN 978-1-4665-1255-9.

E. Wade Miner, Steven E. Ramberg, and Thomas F. Swean Jr. A Method for Approximating the Initial Data Plane for Surface Ship Wake Simulations. NRL Memorandum Report 6376, Naval Research Laboratory, Washington, D.C., November 1988. URL https://apps.dtic.mil/sti/citations/ADA202473.

P.J. Minnett, A. Alvera-Azcárate, T.M. Chin, G.K. Corlett, C.L. Gentemann, I. Karagali, X. Li, A. Marsouin, S. Marullo, E. Maturi, R. Santoleri, S. Saux Picart, M. Steele, and J. Vazquez-Cuervo. Half a century of satellite remote sensing of sea-surface temperature. *Remote Sensing of Environment*, 233:111366, November 2019. ISSN 00344257. doi: 10.1016/j.rse.2019.111366. URL https://linkinghub.elsevier.com/retrieve/pii/S0034425719303852.

Usman Muhammad, Weiqiang Wang, Shahbaz Pervaiz Chattha, and Sajid Ali. Pre-trained VGGNet Architecture for Remote-Sensing Image Scene Classification. In *2018 24th International Conference on Pattern Recognition (ICPR)*, pages 1622–1627, Beijing, August 2018. IEEE. ISBN 978-1-5386-3788-3. doi: 10.1109/ICPR.2018.8545591. URL https://ieeexplore.ieee.org/document/8545591/.

W. H. Munk, P. Scully-Power, and F. Zachariasen. The Bakerian Lecture, 1986. Ships from Space. *Proceedings of the Royal Society of London. A. Mathematical and Physical Sciences*, 412(1843):231–254, August 1987. doi: 10.1098/rspa.1987.0087. URL https://royalsocietypublishing.org/doi/abs/10.1098/rspa.1987.0087.

W. H. Munk, Laurence Armi, Kenneth Fischer, and F. Zachariasen. Spirals on the sea. *Proceedings of the Royal Society of London. Series A: Mathematical, Physical and Engineering Sciences*, 456(1997):1217–1280, May 2000. doi: 10.1098/rspa.2000.0560.

S. M. Newman, J. A. Smith, M. D. Glew, S. M. Rogers, and J. P. Taylor. Temperature and salinity dependence of sea surface emissivity in the thermal infrared. *Quarterly Jour-*

nal of the Royal Meteorological Society, 131(610):2539–2557, July 2005. ISSN 00359009, 1477870X. doi: 10.1256/qj.04.150. URL http://doi.wiley.com/10.1256/qj.04.150.

Reza Olfati-Saber. Kalman-consensus filter : Optimality, stability, and performance. In *Proceedings of the 48h IEEE Conference on Decision and Control (CDC) held jointly with 2009 28th Chinese Control Conference*, pages 7036–7042, 2009. doi: 10.1109/CDC.2009.5399678.

Adam Paszke, Sam Gross, Francisco Massa, Adam Lerer, James Bradbury, Gregory Chanan, Trevor Killeen, Zeming Lin, Natalia Gimelshein, Luca Antiga, et al. Pytorch: An imperative style, high-performance deep learning library. *Advances in Neural Information Processing Systems*, 32:8026–8037, 2019.

R. Peltzer, W. Garrett, and P. Smith. A remote sensing study of a surface ship wake. *International Journal of Remote Sensing*, 8(5):689–704, 1987.

R. D. Peltzer, O. M. Griffin, J. A. C. Kaiser, and W. R. Barger. The 1989 ONR Field Experiment: High Resolution Surfactant Film Measurements. Technical Report AD-A268455, Office of Naval Research, Washington, D.C., July 1993.

Willard J. Pierson and Lionel Moskowitz. A proposed spectral form for fully developed wind seas based on the similarity theory of S. A. Kitaigorodskii. *Journal of Geophysical Research*, 69(24):5181–5190, December 1964. ISSN 01480227. doi: 10.1029/JZ069i024p05181. URL http://doi.wiley.com/10.1029/JZ069i024p05181.

Lary W. Pinkley and Dudley Williams. Optical properties of sea water in the infrared. *Journal of the Optical Society of America*, 66(6):554, June 1976. ISSN 0030-3941. doi: 10.1364/JOSA.66.000554. URL https://opg.optica.org/abstract.cfm?URI=josa-66-6-554.

Lary W. Pinkley, P. P. Sethna, and Dudley Williams. Optical constants of water in the

infrared: Influence of temperature. *Journal of the Optical Society of America*, 67(4):494, April 1977. ISSN 0030-3941. doi: 10.1364/JOSA.67.000494. URL https://opg.optica.org/abstract.cfm?URI=josa-67-4-494.

William J. Plant. A relationship between wind stress and wave slope. *Journal of Geophysical Research*, 87(C3):1961, 1982. ISSN 0148-0227. doi: 10.1029/JC087iC03p01961. URL http://doi.wiley.com/10.1029/JC087iC03p01961.

Riccardo Polvara, Massimiliano Patacchiola, Marc Hanheide, and Gerhard Neumann. Sim-to-Real Quadrotor Landing via Sequential Deep Q-Networks and Domain Randomization. *Robotics*, 9(1):8, February 2020. ISSN 2218-6581. doi: 10.3390/robotics9010008. URL https://www.mdpi.com/2218-6581/9/1/8.

Joseph Redmon, Santosh Divvala, Ross Girshick, and Ali Farhadi. You Only Look Once: Unified, Real-Time Object Detection. Technical Report arXiv:1506.02640, arXiv, May 2016. URL http://arxiv.org/abs/1506.02640. arXiv:1506.02640 [cs] type: article.

Arthur M. Reed and Jerome H. Milgram. Ship Wakes and Their Radar Images. *Annual Review of Fluid Mechanics*, 34(1):469–502, January 2002. ISSN 0066-4189, 1545-4479. doi: 10.1146/annurev.fluid.34.090101.190252. URL https://www.annualreviews.org/doi/10.1146/annurev.fluid.34.090101.190252.

Igor G. Rizaev and Alin Achim. SynthWakeSAR: A Synthetic SAR Dataset for Deep Learning Classification of Ships at Sea. *Remote Sensing*, 14(16):3999, August 2022. ISSN 2072-4292. doi: 10.3390/rs14163999. URL https://www.mdpi.com/2072-4292/14/16/3999.

Igor G. Rizaev, Oktay Karakus, S. John Hogan, and Alin Achim. Modeling and SAR Imaging of the Sea Surface: a Review of the State-of-the-Art with Simulations. *arXiv:2102.05199 [physics]*, January 2022. URL http://arxiv.org/abs/2102.05199. arXiv: 2102.05199.

Wolfgang Rodi. Examples of calculation methods for flow and mixing in stratified fluids. *Journal of Geophysical Research*, 92(C5):5305, 1987. ISSN 0148-0227. doi: 10.1029/JC092iC05p05305. URL http://doi.wiley.com/10.1029/JC092iC05p05305.

Olaf Ronneberger, Philipp Fischer, and Thomas Brox. U-Net: Convolutional Networks for Biomedical Image Segmentation, May 2015. URL http://arxiv.org/abs/1505.04597. Number: arXiv:1505.04597 arXiv:1505.04597 [cs].

Alvin N. Rusk, Dudley Williams, and Marvin R. Querry. Optical Constants of Water in the Infrared. *Journal of the Optical Society of America*, 61(7):895, July 1971. ISSN 0030-3941. doi: 10.1364/JOSA.61.000895. URL https://opg.optica.org/josa/abstract.cfm?uri=josa-61-7-895.

Peter M. Saunders. Radiance of Sea and Sky in the Infrared Window 800–1200 cm^{-1}. *Journal of the Optical Society of America*, 58(5):645, May 1968. ISSN 0030-3941. doi: 10.1364/JOSA.58.000645. URL https://opg.optica.org/abstract.cfm?URI=josa-58-5-645.

Frederic Schwenger and Endre Repasi. Sea surface simulation for testing of multiband imaging sensors. In Wendell R. Watkins, Dieter Clement, and William R. Reynolds, editors, *Targets and Backgrounds IX: Characterization and Representation*, volume 5075, pages 72–84, Orlando, FL, September 2003. SPIE. doi: 10.1117/12.488472. URL http://proceedings.spiedigitallibrary.org/proceeding.aspx?doi=10.1117/12.488472.

David J. Segelstein. *The complex refractive index of water*. PhD thesis, University of Missouri-Kansas City, Kansas City, Missouri, 1981.

Glenn Shafer. *A Mathematical Theory of Evidence*. Princeton University Press, 1976.

Philippe Smets and Robert Kennes. The transferable belief model. *Artificial Intelligence*, 66

(2):191–234, 1994. ISSN 0004-3702. doi: https://doi.org/10.1016/0004-3702(94)90026-4. URL https://www.sciencedirect.com/science/article/pii/0004370294900264.

Dan Sobien, Justin Kauffman, Erik Higgins, Laura Freeman, and Jonathan S Pitt. Evaluation of Machine-Learning Data Fusion Classifier Performance for Ship-Wake Detection with Augmented Data Sets. In *AIAA SCITECH 2023 Forum*, National Harbor, MD & Online, January 2023. doi: 10.2514/6.2023-0195. URL https://arc.aiaa.org/doi/abs/10.2514/6.2023-0195.

B. Solaiman, L.E. Pierce, and F.T. Ulaby. Multisensor data fusion using fuzzy concepts: application to land-cover classification using ers-1/jers-1 sar composites. *IEEE Transactions on Geoscience and Remote Sensing*, 37(3):1316–1326, 1999. doi: 10.1109/36.763295.

John Ryan Somero. *Structure and Persistence of Surface Ship Wakes*. Dissertation, Virginia Polytechnic Institute and State University, Blacksburg, Virginia, USA, 2021.

Ryan Somero, Andre Basovich, and Eric G. Paterson. Structure and Persistence of Ship Wakes and the Role of Langmuir-Type Circulations. *Journal of Ship Research*, 62(04):241–258, December 2018. ISSN 0022-4502, 1542-0604. doi: 10.5957/JOSR.07180036. URL https://onepetro.org/JSR/article/62/04/241/175300/Structure-and-Persistence-of-Ship-Wakes-and-the.

N. R. Stapleton. Ship wakes in radar imagery. *International Journal of Remote Sensing*, 18 (6):1381–1386, April 1997. ISSN 0143-1161, 1366-5901. doi: 10.1080/014311697218494. URL https://www.tandfonline.com/doi/full/10.1080/014311697218494.

Josh Tobin, Rachel Fong, Alex Ray, Jonas Schneider, Wojciech Zaremba, and Pieter Abbeel. Domain randomization for transferring deep neural networks from simulation to the real world. In *2017 IEEE/RSJ International Conference on Intelligent Robots and Systems (IROS)*, pages 23–30, 2017. doi: 10.1109/IROS.2017.8202133.

Jonathan Tremblay, Aayush Prakash, David Acuna, Mark Brophy, Varun Jampani, Cem Anil, Thang To, Eric Cameracci, Shaad Boochoon, and Stan Birchfield. Training deep networks with synthetic data: Bridging the reality gap by domain randomization, 2018.

Naoto Usuyama. UNet/FCN PyTorch. https://github.com/usuyama/pytorch-unet, 2020.

D. Velotto, F. Nunziata, M. Migliaccio, and S. Lehner. Dual-Polarimetric TerraSAR-X SAR Data for Target at Sea Observation. *IEEE Geoscience and Remote Sensing Letters*, 10 (5):1114–1118, September 2013. ISSN 1545-598X, 1558-0571. doi: 10.1109/LGRS.2012.2231048. URL http://ieeexplore.ieee.org/document/6472773/.

Dylan Wall. *Anisotropic Turbulence Modeling for Wakes in an Active Ocean Environment*. Dissertation, Virginia Polytechnic Institute and State University, Blacksburg, Virginia, USA, 2021.

Cornelius J. Willers, Maria S. Willers, and Fabian Lapierre. Signature modelling and radiometric rendering equations in infrared scene simulation systems. page 81870R, Prague, Czech Republic, October 2011. doi: 10.1117/12.903352. URL http://proceedings.spiedigitallibrary.org/proceeding.aspx?doi=10.1117/12.903352.

Donald M Wilson. A Method of Computing Ship Contrast Temperatures Including Results Based on Weather Ship J Environment Data. Technical Report NSWC/WOL TR 78-187, Naval Surface Weapons Center, Silver Spring, Maryland, January 1979.

Xiangqian Wu and William L. Smith. Emissivity of rough sea surface for 8–13 µm: modeling and verification. *Appl. Opt.*, 36(12):2609–2619, Apr 1997. doi: 10.1364/AO.36.002609. URL http://www.osapublishing.org/ao/abstract.cfm?URI=ao-36-12-2609.

Min Xia, Yichen Cui, Yonghong Zhang, Yiming Xu, Jia Liu, and Yiqing Xu. Dau-net: a

novel water areas segmentation structure for remote sensing image. *International Journal of Remote Sensing*, 42(7):2594–2621, 2021. doi: 10.1080/01431161.2020.1856964. URL https://doi.org/10.1080/01431161.2020.1856964.

Zhou Xu, Bo Tang, and Shuiying Cheng. Faint Ship Wake Detection in PolSAR Images. *IEEE Geoscience and Remote Sensing Letters*, 15(7):1055–1059, July 2018. ISSN 1545-598X, 1558-0571. doi: 10.1109/LGRS.2018.2823007. URL https://ieeexplore.ieee.org/document/8341759/.

Li Yang, Xuan Chen, Shizheng Chang, Enchi Xu, Xingyu Wang, Ye Wang, Xiaolong Zhao, Yongchen Du, Wei Kou, and Chunli Fan. Infrared imaging simulation and detection of ship wake. Beijing, China, October 2015. doi: 10.1117/12.2199454. URL http://proceedings.spiedigitallibrary.org/proceeding.aspx?doi=10.1117/12.2199454.

Min Zhang, Yan Wei Zhao, Hui Chen, and Wang-Qiang Jiang. SAR Imaging Simulation for Composite Model of Ship on Dynamic Ocean Scene. *Progress In Electromagnetics Research*, 113:395–412, 2011. ISSN 1559-8985. doi: 10.2528/PIER10121102.

Zhi Zhao, Kefeng Ji, Xiangwei Xing, Huanxin Zou, and Shilin Zhou. Ship Surveillance by Integration of Space-borne SAR and AIS – Review of Current Research. *Journal of Navigation*, 67(1):177–189, January 2014. ISSN 0373-4633, 1469-7785. doi: 10.1017/S0373463313000659. URL https://www.cambridge.org/core/product/identifier/S0373463313000659/type/journal_article.

Chunbo Zhu, Danpei Zhao, Jing Qi, Xinhu Qi, and Zhenwei Shi. Cross-Domain Transfer for Ship Instance Segmentation in SAR Images. In *2021 IEEE International Geoscience and Remote Sensing Symposium IGARSS*, pages 2206–2209, Brussels, Belgium, July 2021. IEEE. ISBN 978-1-66540-369-6. doi: 10.1109/IGARSS47720.2021.9554284. URL https://ieeexplore.ieee.org/document/9554284/.

G. Zilman, A. Zapolski, and M. Marom. The speed and beam of a ship from its wake's SAR images. *IEEE Transactions on Geoscience and Remote Sensing*, 42(10): 2335–2343, October 2004. ISSN 0196-2892. doi: 10.1109/TGRS.2004.833390. URL http://ieeexplore.ieee.org/document/1344183/.

Gregory Zilman, Anatoli Zapolski, and Moshe Marom. On Detectability of a Ship's Kelvin Wake in Simulated SAR Images of Rough Sea Surface. *IEEE Transactions on Geoscience and Remote Sensing*, 53(2):609–619, February 2015. ISSN 0196-2892, 1558-0644. doi: 10.1109/TGRS.2014.2326519. URL http://ieeexplore.ieee.org/document/6828750/.

Nina Ødegaard, Atle Onar Knapskog, Christian Cochin, and Jean-Christophe Louvigne. Classification of ships using real and simulated data in a convolutional neural network. In *2016 IEEE Radar Conference (RadarConf)*, pages 1–6, 2016. doi: 10.1109/RADAR.2016.7485270.